

Element-selective and time-resolved magnetic investigations in the extreme ultraviolet range

Patrik Grychtol

Forschungszentrum Jülich GmbH
Peter Grünberg Institut (PGI)
Elektronische Eigenschaften (PGI-6)

Element-selective and time-resolved magnetic investigations in the extreme ultraviolet range

Patrik Grychtol

Schriften des Forschungszentrums Jülich
Reihe Schlüsseltechnologien / Key Technologies

Band / Volume 22

ISSN 1866-1807

ISBN 978-3-89336-706-1

Bibliographic information published by the Deutsche Nationalbibliothek.
The Deutsche Nationalbibliothek lists this publication in the Deutsche
Nationalbibliografie; detailed bibliographic data are available in the
Internet at <http://dnb.d-nb.de>.

Publisher and
Distributor: Forschungszentrum Jülich GmbH
Zentralbibliothek
52425 Jülich
Phone +49 (0) 24 61 61-53 68 · Fax +49 (0) 24 61 61-61 03
e-mail: zb-publikation@fz-juelich.de
Internet: <http://www.fz-juelich.de/zb>

Cover Design: Grafische Medien, Forschungszentrum Jülich GmbH

Printer: Grafische Medien, Forschungszentrum Jülich GmbH

Copyright: Forschungszentrum Jülich 2011

Schriften des Forschungszentrums Jülich
Reihe Schlüsseltechnologien / Key Technologies Band / Volume 22

D 464 (Diss., Duisburg, Univ., 2011)

ISSN 1866-1807
ISBN 978-3-89336-706-1

The complete volume is freely available on the Internet on the Jülicher Open Access Server (JUWEL) at
<http://www.fz-juelich.de/zb/juwel>

Neither this book nor any part of it may be reproduced or transmitted in any form or by any
means, electronic or mechanical, including photocopying, microfilming, and recording, or by any
information storage and retrieval system, without permission in writing from the publisher.

Zusammenfassung

Ziel dieser Dissertation ist es, den extremen ultravioletten (EUV) Spektralbereich im Hinblick auf elementselektive magneto-optische Untersuchungen zu erkunden. Zu diesem Zweck konzentriert sich die folgende Arbeit auf eisen-, cobalt- und nickelbasierte Legierung und Mehrschichtsysteme bedingt durch ihre hohe Bedeutung für die Grundlagenforschung und Technik. Es wurden vier Reflexionsexperimente durchgeführt, die sich des transversalen magneto-optischen Kerreffekts (T-MOKE) an den M Absorptionskanten dieser Übergangsmetalle bedienen. Für diese Experimente kamen sowohl synchrotron- als auch laserbasierte Röntgenlichtquellen zum Einsatz, dessen gepulste Emissionscharakteristik auch für zeitaufgelöste Experimente genutzt wurde.

Während sich das erste Experiment mit räumlich getrennten aber homogenen und ferromagnetisch gekoppelten Schichten in einem $\text{Co}(5\text{ nm})/\text{Si}(1-4\text{ nm})/\text{Ni}(8\text{ nm})/\text{Fe}(2\text{ nm})$ Mehrschichtsystem befasst, wurde in dem zweiten Experiment ein $\text{Ni}_{80}\text{Fe}_{20}(5\text{ nm})/\text{Cr}(0.6\text{ nm})/\text{Co}_{40}\text{Fe}_{60}(10\text{ nm})$ Mehrschichtsystem untersucht, welches aus zwei heterogenen und anti-ferromagnetisch gekoppelten Schichten besteht. Mit entsprechenden Messungen und magneto-optischen Simulationen wird der Charakter des magneto-dichroitischen Signals in Abhängigkeit der Photonenenergie, des Einfallswinkels und der Zwischenschichtdicke erforscht. Ein magnetischer Kontrast in Höhe von 80 % kann erreicht werden und Hysteresekurven zeigen, dass das Schalten einzelner Schichten schichtselektiv untersucht werden kann.

Im dritten Experiment wird Präzessionsdynamik der Magnetisierung in Permalloy-schichten untersucht. Die durch einen Laserpuls induzierte Präzession wird mittels synchronisierter EUV Pulse vom Synchrotron an der M Nickelkante vermessen. Das Resultat in Kombination mit Vergleichsmessungen im optischen Labor zeigt nicht nur die Durchführbarkeit, sondern auch die Grenzen eines solchen Pump-Probe-Ansatzes.

Das vierte Experiment befasst sich mit der ultraschnellen Entmagnetisierung von Permalloy, welche durch intensive Laserpulse induziert wird. Ein magnetischer Kontrast von 30 % kann dazu genutzt werden, die zeitliche Entwicklung dieses Prozesses elementselektiv und mit einer Zeitauflösung von 55 fs mittels EUV Pulsen aus einer laserbasierten Röntgenquelle zu untersuchen. Das Resultat deutet darauf hin, dass die lokale Spinumgebung auf der atomaren Ebene eine große Rolle spielt und in der Beschreibung ultraschneller Entmagnetisierungsprozesse berücksichtigt werden muss.

Abstract

The objective of this thesis is to explore the potential of the extreme ultraviolet (EUV) region to serve as an element-selective and magnetic contrast mechanism for magneto-optical investigations. To this end, the following work focuses on alloy and multilayer model systems based on iron, cobalt and nickel due to their high relevance for both fundamental research and technology. Four reflectivity experiments exploiting the transversal magneto-optical Kerr effect (T-MOKE) have been performed by tuning the photon energy to the M absorption edges of the respective 3d transition ferromagnets and by employing synchrotron as well as laser based soft x-ray light sources.

In the first experiment spatially separated but homogeneous and ferromagnetically coupled layers in a wedged Co(5 nm)/Si(1-4 nm)/Ni(8 nm)/Fe(2 nm) multilayer are studied, whereas the second experiment is concerned with magneto-optical investigations of a single Ni₈₀Fe₂₀(5 nm)/Cr(0.6 nm)/Co₄₀Fe₆₀(10 nm) multilayer containing two anti-ferromagnetically coupled heterogeneous ferromagnetic layers. Measurements and supporting simulations of the magneto-optical response as a function of the photon energy, the incidence angle and the spacer thickness explore the character of the magneto-dichroic signal in the EUV and its potential for layer-selective investigations. A magnetic contrast as high as 80 % can be obtained and the recorded hysteresis loops prove that the switching of single layers can indeed be measured layer-selectively.

In the third experiment, precessional dynamics of the magnetization in thin permalloy films patterned to form a coplanar waveguide is induced by ultrashort laser pulses. The resulting oscillatory response is probed by synchronized EUV pulses originating from a synchrotron tuned to the M absorption edge of Ni. The obtained results in combination with reference measurements in the visible range not only prove the feasibility, but also explore the limitations of this pump-probe approach.

The fourth experiment is concerned with the ultrafast demagnetization of permalloy, which is optically driven by intense laser pulses. A magnetic contrast of 30% can be exploited to element-selectively probe the evolution of the magnetic system by EUV pulses from a table-top soft x-ray source with an unprecedented temporal resolution. The result suggests that the local spin environment at the atomic level plays a vital role in the dynamic response of magnetic materials, and must be included for a complete understanding of the microscopic physics underlying demagnetization processes.

Acknowledgements

First of all, I would like to thank the following advisors, colleagues, friends and relatives, who contributed to the success of this dissertation the one way or the other:

Prof. Claus M. Schneider for providing the opportunity to conduct research in an international environment as well as maintaining an open-minded working atmosphere.

Prof. Martin Aeschlimann for not only accepting the burden of reviewing this thesis, but also supporting my research fellowship to the University of Colorado.

Prof. Margaret Murnane and **Prof. Henry Kapteyn** for generously sharing their experience and offering deep insights into laser-generated soft x-ray science.

Prof. Peter Oppeneer for fruitful discussions in the field of magneto-optics.

Prof. Paul Bechthold for proof-reading this thesis.

Dr. Roman Adam for sharing his experience and for motivating me during many long night shifts at the synchrotron, which resulted in a successful collaboration.

Dr. Stefan Mathias and **Chan La-O-Vorakiat** for sharing their experience in operating a table-top soft x-ray source as well as engaging in a flourishing collaboration.

Dr. Stefan Cramm for sharing his synchrotron knowledge, resulting in an excellent beamline support around the clock and many helpful scientific discussions.

Dr. Tom Silva, **Dr. Justin Shaw** and **Dr. Hans Nembach** for sharing their expertise in the field of ferromagnetic resonance and sample fabrication.

Dr. Sergio Valencia for generously supporting the reflectivity experiment on magnetic multilayers with magneto-optical simulations.

Dr. Matthias Buchmeier for an invaluable introduction into the realm of magnetic multilayers, the magneto-optical Kerr effect and Brillouin light scattering.

Dr. Daniel Bürgler for providing expertise in the field of multilayer coupling phenomena and proof-reading several manuscripts.

Dr. Alexander Kaiser and **Dr. Carsten Wiemann** for thoroughly characterizing various samples with the photo electron emission microscope at the synchrotron.

Bernd Küpper and **Konrad Bickmann** for various priceless design and construction works, that often had to be done on short notice, and interesting insights into mechanics as well as ultra high vacuum technology.

Jürgen Lauer, **Heinz Pfeiffer** and **Norbert Schnitzler** for the development and construction of irreplaceable and inventive programmes as well as electronic devices, and their personal assistance at the beamline in fixing even the nastiest bugs.

Reinert Schreiber, **Franz-Josef Köhne**, **Hans Wingens** and **Thomas Jansen** for the careful deposition of high quality magnetic thin film systems.

The team of the **IFF mechanical workshop**, headed by **Kurt Hirtz**, for the realization of various mechanical constructions.

Jürgen Müller and **Holger John** for the support of the IBN and IFF clean rooms.

Stefan Trellenkamp and **Mona Nonn** for providing invaluable expertise in electron beam lithography and for the fabrication of optical lithography masks.

The staff at **BESSY** for their relentless technical support during beamtimes.

The **BMBF** and the **DAAD** for their generous financial support.

All colleagues from **Jülich**, **Kaiserslautern** and **Boulder** for the enjoyable collaboration and infrequent leisure activities, creating a pleasant working atmosphere and supplying coffee as well as occasional distractions from the routine in the lab.

All good friends from the **Aachen Crew** and my family for a life besides research: Especially my girlfriend **Maria Wingens** and our son **Elias** for accompanying and emotionally supporting me all the way long, as well as my parents **Jolanthe** and **Johann Grychtol** for their interest and support during my studies.

Contents

1	Motivation	1
2	Magneto-Optical Considerations	5
2.1	Magneto Optical Kerr Effect (MOKE)	5
2.1.1	Polar MOKE	8
2.1.2	Longitudinal MOKE	10
2.1.3	Transversal MOKE	11
2.2	MOKE and XMCD	12
2.3	MOKE in Multilayer Systems	13
2.4	The Classical Oscillator Model	14
2.5	Quantum Mechanical Considerations	15
2.6	T-MOKE at High Photon Energies	17
2.6.1	EUV vs. Soft X-Ray Regime	19
3	Instrumentation and Methods	21
3.1	X-Ray Generation at the Synchrotron	21
3.2	UHV Reflectometer	25
3.3	Time-Resolved Experiments at the Synchrotron	27
3.4	MOKE Experiments in the Optical Laboratory	30
3.5	Soft X-Rays from Higher Harmonic Generation	33
3.6	Time-Resolved Experiments employing a HHG Source	37
3.7	Construction of a HHG Beamline	38
4	Static Synchrotron Experiments	45
4.1	A Ferromagnetically Coupled Multilayer	46
4.1.1	Sample Preparation and Characterization	46
4.1.2	Magneto-Optical Response in the EUV	47
4.1.3	Magnetic Switching Behavior	51
4.1.4	Magneto-Optical Crosstalk and Interferences	54
4.1.5	Summary and Conclusion	56

4.2	An Anti-Ferromagnetically Coupled Multilayer	57
4.2.1	Sample Preparation and Characterization	57
4.2.2	Magneto-Optical Response in the EUV	60
4.2.3	Magnetic Switching Behavior	63
4.2.4	Summary and Conclusion	65
5	Magnetization Dynamics	67
5.1	Time-Resolved Precessional Dynamics	68
5.1.1	Sample Preparation and Characterization	68
5.1.2	Time-Resolved MOKE in the Visible Range	71
5.1.3	Time-Resolved MOKE in the EUV	75
5.1.4	Summary and Conclusion	79
5.2	Ultrafast Demagnetization Dynamics	80
5.2.1	Sample Preparation and Characterization	81
5.2.2	Demagnetization Dynamics of Nickel	86
5.2.3	Demagnetization Dynamics of Permalloy	92
5.2.4	Summary and Conclusion	98
6	Conclusion and Outlook	99
	Appendix	105
1	APD Powersupply	107
2	Pulse Stretcher	109
3	Balanced Detection Scheme	111
4	Toroid Chamber	113
5	Sample Chamber	115
6	HHG Reflectivity Experiment	117
7	MATLAB Evaluation Routine	119
	Bibliography	127
	Publications	139
	Conference Contributions	141
	Curriculum Vitae	143

Chapter 1

Motivation

The following work is motivated by the substantial advance in the understanding of magnetism that took place in the last few decades. This progress has largely been driven by scientific curiosity and the on-going development of preparative as well as investigative methods. While the former propels the latter, it is the discovery of new phenomena that arises from the utilization of novel experimental techniques, paving the way for new ideas and concepts. This is even more true as new technological achievements result and crucially contribute to the advancement of society. The most prominent example in the recent history of magnetism is the miniaturization of hard disk read heads facilitated by exploiting the *giant magnetoresistance* (GMR). The independent discovery of this effect by the groups of Albert Fert and Peter Grünberg has been awarded with the Nobel prize in 2007 due to its significant impact on today's information society.

The discovery of phenomena related to magnetic properties of thin metallic films, such as the GMR [1], has been made possible by major improvements in deposition as well as characterization techniques. With the advent of molecular beam epitaxy in the nineteen-eighties, films with thicknesses down to a single monolayer could be grown with a high quality regarding chemical purity, crystalline structure, interface roughness and homogeneity [2]. Thus, theoretically predicted modifications of magnetic properties, such as the anisotropy and the domain structure, introduced by a reduction of the dimensionality could be studied. In the wake of this instrumental development, a wealth of phenomena, such as *interlayer exchange coupling* [3] and *tunnelling magnetoresistance* [4], were discovered or experienced a revival. These effects among various others found their way into a wide range of electronic applications ranging from sensors [5] and hard disk read heads [6] to transistors [7]. This diversity opened the door of *spintronics*, an entirely new field of research, which nowadays has substantiated its high relevance for both fundamental research and technology [8, 9]. In this context, exploiting the quantum nature of the electron spin may result in the development of novel devices, such as magnetic logics [10] or non-volatile magnetoresistive random access memories [11].

As it is customary to manipulate and store data by recording zeros and ones in the sense of magnetizationally reversed domain states, switching the magnetization in a controlled manner as quickly as possible has grown into a widely pursued scientific objective. Moreover, if an ever increasing information density is required not only the speed of manipulation has to increase, but also the size of a single bit has to be reduced. To this end, it is essential to understand exactly which mechanisms at which scale of time and space contribute to the magnetic reversal process. In general, magnetization dynamics involves micromagnetic processes on a broad time scale, including domain wall nucleation and propagation on the milli- to nanosecond time scale [12], vortex core and precessional switching on the picosecond scale [13, 14], or ultrafast demagnetization [15] and all optical switching [16] in the femtosecond range. In the spatial domain, state of the art preparation methods allow for the fabrication of high quality nanoscale structures, whose magnetic properties can be tuned both by the dimension and the chemical composition of the thin film system. It can therefore be concluded that ultimately a highly sensitive as well as element-selective method of investigation is required, which combines a temporal resolution on the femtosecond scale with a spatial resolution on the nanometer scale.

Since the discovery of the magneto-optical Kerr (MOKE) effect in the eighteen-seventies [17, 18], a magneto-optic reflectivity experiment has often been the technique of choice to study ferromagnetic materials. The Kerr effect is associated with the elastic scattering of polarized light at a magnetic surface within the visible range. Here, a change of the magnetization state in the material usually induces a change in the polarization state of the scattered light, except for a transversal Kerr (T-MOKE) geometry, in which the magneto-optical response directly translates into an intensity modulation. This contrast mechanism has been initially exploited to study the switching behavior of magnetic films or to visualize the magnetic domain structure of a sample. Investigations of reversible magneto-dynamic processes followed as mechanical and later electro-optical shutter allowed for the first pump-probe experiments with a temporal resolution ranging into the nanosecond regime [19, 20]. That is how processes such as the magnetization reversal by propagation of magnetic domain walls or coherent magnetization rotation could be mapped in a stroboscopic manner. Not until the development of pulsed Ti:Sapphire based lasers, atomic timescales in the femtosecond regime were accessible, thereby providing a method to address magnetism at a fundamental level away from the thermal equilibrium of the magnetic system and where a conventional macrospin approximation fails [21–24]. In spite of the superb temporal resolution of this approach, the wavelengths employed in these nowadays conventional MOKE experiments are large as compared to cutting-edge magnetic structures on the nanometer scale, thus precluding their imaging with an appropriate lateral resolution [25]. Moreover, in the visible range the Kerr effect does not offer element-selectivity and it is weak in most materials - less than a millirad of Kerr rotation and far below one percent change in intensity upon a full magnetization reversal.

In the last decade, these shortcomings have been largely overcome by exploiting much stronger magneto-optical effects in the soft x-ray regime. Although these effects can be treated in a common theoretical framework, it is convenient to distinguish between magneto-dichroic phenomena in absorption and transmission, e.g., x-ray magnetic circular dichroism (XMCD) and linear dichroism (XMLD) [26, 27], and magneto-dichroic effects in reflection. The latter are often grouped under the term x-ray resonant magnetic scattering (XRMS) and are closely related to the MOKE in the visible range. All of these phenomena require a resonant excitation by means of linearly or circularly polarized tunable soft x-rays, which are provided by large synchrotron radiation facilities. At the L absorption edges of transition metals at photon energies above 500 eV, both XRMS and XMCD effects allow for magnetic investigations of individual constituents of heterogeneous ferromagnetic systems on a nanometer scale. Thus, not only a superior magnetodichroic contrast of up to several tens of percent and a lateral resolution down to a few nanometers can be attained, but also element-selectivity can be gained in a resonant excitation [28–30]. These investigative methods, however, significantly increase the experimental complexity and are restricted in terms of availability as compared to a laboratory approach, which is basically accessible the whole year round rather than two weeks per semester. This is even more true, as a temporal resolution in the femtosecond range is desired, therefore necessitating appropriate techniques such as femtoslicing [31] or suitable light sources such as free-electron lasers [32].

This kind of experimental drawbacks can nowadays be addressed by exploiting resonant magnetic reflectivity and magnetic dichroism at the M edges of transition metals at photon energies around 50 eV – in the extreme ultraviolet (EUV) regime. With respect to the magneto-optical response, these EUV phenomena have been found equally useful, with changes of the dichroic contrast ranging up to almost 100 % [33–37]. Because the majority of beamlines at third generation synchrotron facilities are dedicated to photon energies in the soft x-ray region, the opportunity of EUV magneto-optical studies has mostly escaped the attention of the magnetic community. However, recently substantial progress has been made in the development of laser-based soft x-ray sources reaching photon energies of up to 100 eV with moderate effort. These reliable table-top light sources are able to produce ultrashort EUV light pulses, which retain the coherence properties as well as the temporal femtosecond structure of the driving laser by exploiting a highly nonlinear conversion process (Higher Harmonic Generation - HHG) [38–40]. Due to the pulsed and coherent nature of the emitted radiation, HHG based light sources may serve as compact tools for element-selective investigations of magnetic properties on femtosecond and nanometer scales in a laboratory environment [41, 42]. Since only little work has been done in this wavelength range and the prospect is high to develop a practical technique which addresses the underlying mechanisms of magnetism at fundamental levels of space and time, a closer look into magneto-optics of the extreme ultraviolet region is imperative.

Therefore, it is the purpose of this work to explore the potential of the EUV region for magnetic contrast generation by tuning the photon energy to the M absorption edges of 3d transition ferromagnets in T-MOKE reflectivity experiments. By employing synchrotron as well as HHG based soft x-ray light sources the performance of this approach with respect to element-selective and time-resolved magnetic investigations will be assessed. To this end, this study focuses on multilayer and alloy model systems based on Fe, Co and Ni due to their high relevance for both fundamental research and technology. After having embedded this work into a historic as well as a scientific context, this thesis continues the following way:

Chapter 2 deals with magneto-optical considerations, in which a mathematical formulation of the Kerr effect is derived from Maxwell's equations that can be readily applied to resonant reflectivity in the EUV and even the soft x-ray region.

Chapter 3 introduces the experimental instrumentation as well as methods, which were employed and partly developed for investigations of magnetic heterostructures within the context of this thesis. This description ranges from a static reflectivity experiment at the synchrotron to a custom made pump-probe setup comprising a HHG based table-top soft x-ray source.

Chapter 4 is concerned with results obtained in static reflectivity experiments at the synchrotron. Basically two experiments have been conducted, both of which focus on coupled magnetic multilayer systems comprising iron, cobalt and nickel. Both studies address the question of whether the switching behavior of individual layers can be separated in a multilayer consisting either of chemically homogeneous or heterogeneous layers, respectively.

Chapter 5 shows results obtained in pump-probe experiments employing a synchrotron light source as well as a table-top soft x-ray source. For this purpose two experiments have been conducted investigating permalloy as a model system. The first experiment focuses on precessional magnetization dynamics in the picosecond range of a thermally equilibrated magnetic system, whereas the second experiment studies ultrafast demagnetization dynamics element-selectively on the femtosecond timescale far away from the thermal equilibrium of the magnetic system.

Chapter 6 summarizes the most important findings and concludes with an outlook for future experiments, whereas the **Appendix** shows plans that are supposed to elucidate the operation of some experiments as well as document the principles behind some of the custom made electronic devices and the computer code programmed to evaluate and display the recorded data.

Magneto-Optical Considerations

The interaction of light with a magnetic system provides a wealth of experimental means to study various aspects of magnetism. This chapter focuses on the magneto-optical Kerr effect (MOKE), which is utilized to extract information about the magnetic state of a sample under investigation. As the mathematical formulation of the Kerr effect, including its terminology, is more than one hundred years old [43], the derivation shown here follows the description of recently published material, the author of which has a strong background in magneto-optics of the extreme ultraviolet (EUV) as well as soft x-ray region [44]. It is noteworthy that PhD theses can be referred to, which not only fully derive the formulas for all MOKE geometries based on the original formulation from 1908, but also, just like this study, focus their attention to resonant magneto-optic phenomena in the EUV [45, 46].

2.1 Magneto Optical Kerr Effect (MOKE)

MOKE is commonly associated with the influence of magnetic materials on scattered polarized light in the visible range. Depending on the reflection geometry of the experiment, the magnetic moment of the material can induce either a modulation of the intensity or a change in the polarization state of the scattered light. The mathematical formulation of this interaction can be directly deduced from Maxwell's equations including boundary conditions for dielectric media within a magneto-optical framework by connecting the sample magnetization with the Fresnel reflection coefficients via the dielectric tensor. It is possible to account for the complex quantum mechanical interaction of light and matter by utilizing a quantum mechanical description of phenomenological response functions. This description can be readily applied to resonant reflectivity in the EUV and even soft x-ray region, as the wavelength of the scattered radiation can still be considered large in comparison to the interatomic distance satisfying the macroscopic nature of Maxwell's equations [47]. Presuming the absence of permanent electrical charges and currents on the surface of an anisotropic medium that

interacts with a plane and monochromatic electromagnetic wave, Maxwell's equations can be written as:

$$\vec{\nabla} \times \vec{E} = -\mu_0 \frac{\partial \vec{H}}{\partial t}, \quad (2.1)$$

$$\vec{\nabla} \times \vec{H} = \frac{\partial \vec{D}}{\partial t}, \quad (2.2)$$

$$\vec{\nabla} \cdot \vec{D} = 0, \quad (2.3)$$

$$\vec{\nabla} \cdot \vec{H} = 0, \quad (2.4)$$

with μ_0 the vacuum permeability, \vec{D} the electric displacement, \vec{E} the electric field averaged over microscopic regions on the atomic scale, and \vec{H} the phenomenological macroscopic magnetic field. Moreover, the derived field \vec{D} in the medium can be related to the microscopic field \vec{E} by a material relationship via the vacuum permittivity ϵ_0 , the electric polarization \vec{P} and the dielectric tensor $\overleftrightarrow{\epsilon}$, respectively:

$$\vec{D} = \epsilon_0 \vec{E} + \vec{P} = \overleftrightarrow{\epsilon} \vec{E}. \quad (2.5)$$

For the sake of simplicity the medium is assumed to be bounded by vacuum, and plane monochromatic waves of the following form are considered to propagate with a frequency of ω along their complex wavevector \vec{k} in the anisotropic medium, with \vec{r} denoting the position vector and \vec{E}_0 , \vec{D}_0 , \vec{H}_0 their respective complex amplitudes.

$$\vec{E}(\vec{r}, t) = \vec{E}_0 e^{i(\vec{k}\vec{r} - \omega t)}, \quad (2.6)$$

$$\vec{D}(\vec{r}, t) = \vec{D}_0 e^{i(\vec{k}\vec{r} - \omega t)}, \quad (2.7)$$

$$\vec{H}(\vec{r}, t) = \vec{H}_0 e^{i(\vec{k}\vec{r} - \omega t)}. \quad (2.8)$$

These equations can be inserted into Maxwell's equations resulting in orthogonality conditions for the respective fields

$$\vec{k} \times \vec{E} = \mu_0 \omega \vec{H}, \quad (2.9)$$

$$\vec{k} \times \vec{H} = -\omega \vec{D}, \quad (2.10)$$

$$\vec{k} \cdot \vec{H} = 0, \quad (2.11)$$

$$\vec{k} \cdot \vec{D} = 0, \quad (2.12)$$

which can be used to obtain the following equation by the cross product of \vec{k} with equation 2.9 and exploiting equation 2.10:

$$\vec{k} \times (\vec{k} \times \vec{E}) = \mu_0 \omega \vec{k} \times \vec{H} = -\mu_0 \omega^2 \vec{D}. \quad (2.13)$$

Considering $c^{-1} = \sqrt{\mu_0 \epsilon_0}$ and the vector identity:

$$\vec{a} \times (\vec{b} \times \vec{c}) = (\vec{a} \cdot \vec{c}) \cdot \vec{b} - (\vec{a} \cdot \vec{b}) \cdot \vec{c}, \quad (2.14)$$

the general wave equation, also known as the Fresnel equation, can be derived:

$$\vec{k} \cdot (\vec{k} \cdot \vec{E}) - k^2 \vec{E} + \frac{\omega^2}{\epsilon_0 c^2} \overleftrightarrow{\epsilon} \cdot \vec{E} = [\vec{k} \vec{k}^T - k^2 \mathbf{1} + \frac{\omega^2}{\epsilon_0 c^2} \overleftrightarrow{\epsilon}] \cdot \vec{E} = 0. \quad (2.15)$$

Since the dielectric tensor is determined by the physical property of the material involved and it is expressed as a phenomenological and fixed quantity, the complex refractive index $\vec{n} \equiv c \vec{k} / \omega$, with c the velocity of light in vacuum, and the modes of the electric field $\vec{E}(\vec{r}, t)$ follow from the solution of

$$\det[\vec{n} \vec{n}^T - n^2 \mathbf{1} + \frac{\overleftrightarrow{\epsilon}}{\epsilon_0}] = 0. \quad (2.16)$$

By adding appropriate boundary conditions a full description of all linear optical as well as magneto-optical effects in a reflectivity experiment can be obtained. These are derived from the continuity requirements of Maxwell's equation and the phase of the electro-magnetic wave at the interface of the media involved, here the vacuum and the anisotropic material. Because the Kerr effect depends on the polarization of the incident light wave, it is customary to consider this beam as a superposition of a s - and p -polarized wave, which refer to the orientation of its electric field vector aligned either perpendicular or parallel to the plane of incidence. Within this notation a change of polarization at the interface of the medium induced by an external magnetic field can be expressed by the Fresnel reflection coefficients [48, 49]:

$$\begin{pmatrix} E'_s \\ E'_p \end{pmatrix} = \begin{pmatrix} r_{ss} & r_{sp} \\ r_{ps} & r_{pp} \end{pmatrix} \begin{pmatrix} E_s \\ E_p \end{pmatrix}. \quad (2.17)$$

Here, E_s and E_p are the complex components of the incident electric field in s and p direction, whereas E'_s and E'_p are the respective components of the reflected beam.

As for oblique angles of incidence with respect to the sample surface and the magnetization rather complicated solutions for the Kerr effect result, it is convenient to confine the following discussion to distinct geometries in order to grasp the essence of MOKE. Commonly, three special cases are distinguished (see figure 2.1):

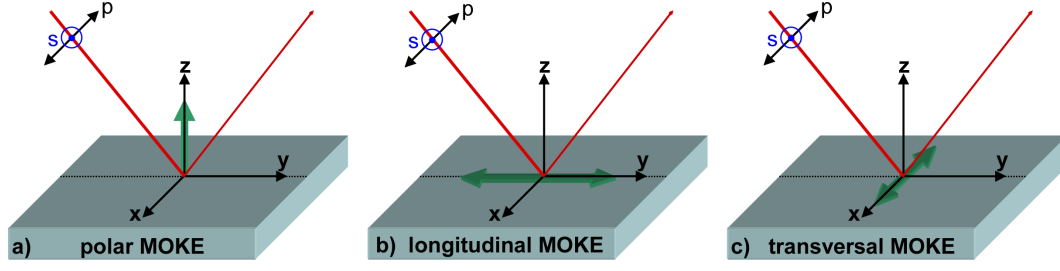


Figure 2.1: Overview of Kerr geometries

- In the **polar** MOKE geometry the magnetic field is aligned along the normal of the sample surface and in the plane of incidence - see figure 2.1a.
- In the **longitudinal** MOKE geometry the magnetic field is aligned in the sample surface as well as the plane of incidence - see figure 2.1b.
- In the **transversal** MOKE geometry the magnetic field is aligned in the sample surface and perpendicular to the plane of incidence - see figure 2.1c.

These reflection geometries are discussed in more detail in the following sections.

2.1.1 Polar MOKE

In the polar geometry the magnetization \vec{M} of the material points along the surface normal, which is chosen to be the z-axis of the Cartesian coordinate system. By exploiting the Onsager relation for this particular cubic crystal structure $\epsilon_{nn}(\vec{M}) = \epsilon_{nn}(-\vec{M})$ and $\epsilon_{nm}(\vec{M}) = \epsilon_{nm}(-\vec{M})$, the related dielectric tensor adopts the following form resulting in a rotational symmetry along the z-axis:

$$\overleftrightarrow{\epsilon}_p = \begin{pmatrix} \epsilon_{xx} & \epsilon_{xy} & 0 \\ -\epsilon_{xy} & \epsilon_{xx} & 0 \\ 0 & 0 & \epsilon_{zz} \end{pmatrix}. \quad (2.18)$$

Under the assumption that the light is at normal incidence, a simple and exact solution of the Fresnel equation can be readily given with $\vec{n} = n\vec{e}_z$. Due to the high symmetry of the problem, the polarization of the incident beam does not have to be considered:

$$n_{\pm}^2 = \epsilon_{xx} \pm i\epsilon_{xy} \quad ; \quad \vec{E}_{\pm}(\vec{r}, t) = \frac{1}{\sqrt{2}} E_0 (\vec{e}_x \pm i\vec{e}_y) e^{i\omega n_{\pm} z/c - i\omega t}. \quad (2.19)$$

Thus, the resulting modes of the reflected electric field can be associated with a left-hand as well as a right-hand circularly polarized light wave, whose amplitude and phase differ for a non vanishing ϵ_{xy} . This off-diagonal element of the dielectric tensor is linearly proportional to the magnetization in first approximation. It ultimately gives rise to the magneto-optical Kerr effect by inducing both a phase shift and an amplitude change in the electric field. As a consequence, the initial polarization of the light changes from linear to elliptical in the reflection process, which is expressed by the complex Kerr angle Φ_K , defined by the sum of the Kerr rotation Θ_K and Kerr ellipticity ϵ_K :

$$\Phi_K = \Theta_K + i\epsilon_K. \quad (2.20)$$

In most materials the Kerr effect is rather small inducing less than 1° of rotation and ellipticity into the beam upon a full magnetization reversal. That is why a relatively simple expression of the Kerr angle can be found in first approximation:

$$\Phi_K \approx \frac{-\epsilon_{xy}\epsilon_0}{\sqrt{\epsilon_{xx}}(\epsilon_0 - \epsilon_{xx})} = -\frac{in_0n}{n^2 - n_0^2}Q_z, \quad (2.21)$$

with $n = \sqrt{\epsilon_{xx}}$ being the average refractive index of the magnetic reflective medium, $n_0 = \sqrt{\epsilon_0}$ being the refractive index of the non-magnetic transmitted medium, here vacuum, and $Q_z = i\frac{\epsilon_{xy}}{\epsilon_{xx}}$, the z component of Voigt vector \vec{Q} , which is commonly introduced to account for magnetic interactions.

Similarly, a more general expression for oblique incident angles ϕ_i can be found. Here, the symmetry with respect to the magnetic field applied along the z-axis is broken and the boundary conditions at the interface between vacuum and the medium have to account for the polarization of the incident light. The solution of the Fresnel equation follows with ϕ_t^\pm denoting the angles of refraction of the two beams:

$$n_\pm^2 = \epsilon_{xx} \pm i\epsilon_{xy} \cos\phi_t^\pm. \quad (2.22)$$

In the first order of ϵ_{xy} , ϕ_t^\pm can be approximated by ϕ_t representing the angle of refraction in the non-magnetized medium. Thus, the resulting complex Fresnel reflection coefficients r_{ss} , r_{pp} and r_{sp} of the s- and p-polarized modes can be written as:

$$r_{ss} = \frac{n_0 \cos\phi_i - n \cos\phi_t}{n_0 \cos\phi_i + n \cos\phi_t} \quad ; \quad r_{pp} = \frac{n \cos\phi_i - n_0 \cos\phi_t}{n \cos\phi_i + n_0 \cos\phi_t}, \quad (2.23)$$

$$r_{ps} = r_{sp} = \frac{-in_0(n_+ - n_-) \cos\phi_i}{(n \cos\phi_t + n_0 \cos\phi_i)(n \cos\phi_i + n_0 \cos\phi_t) \cos\phi_t}, \quad (2.24)$$

which then can be linked to the Kerr angle for the first order in Q :

$$\Phi_K^s = -\frac{r_{ps}}{r_{ss}} \approx -\frac{in_0n}{n^2 - n_0^2} Q_z \frac{\cos\phi_i}{\cos(\phi_i - \phi_t)}, \quad (2.25)$$

$$\Phi_K^p = \frac{r_{sp}}{r_{ss}} \approx -\frac{in_0n}{n^2 - n_0^2} Q_z \frac{\cos\phi_i}{\cos(\phi_i + \phi_t)}. \quad (2.26)$$

2.1.2 Longitudinal MOKE

In the longitudinal geometry the magnetization is oriented within the plane of the sample surface as well as the plane of incidence. If the surface normal is defined to be parallel to the z-axis, the plane of incidence lies within the y-z plane, and the magnetization aligns along the y-axis, the dielectric tensor adopts the following form:

$$\overleftrightarrow{\epsilon}_l = \begin{pmatrix} \epsilon_{xx} & 0 & \epsilon_{xz} \\ 0 & \epsilon_{yy} & 0 \\ -\epsilon_{xz} & 0 & \epsilon_{xx} \end{pmatrix}. \quad (2.27)$$

It can be easily shown that an elementary transformation of the basis can convert this tensor to a form previously associated with the polar geometry. This proves the off-diagonal components of the respective tensors ϵ_{xy} and ϵ_{xz} to be equivalent and thus to contain the origin of the magneto-optic interaction [50]. That is also why the solutions of the Fresnel equation have a comparable form:

$$n_{\pm}^2 \approx \epsilon_{xx} \pm i\epsilon_{xz} \sin\phi_t^{\pm}, \quad (2.28)$$

Even the relation of the Kerr angle and the complex Fresnel reflexion coefficients for the polar and longitudinal geometry share a striking similarity:

$$\Phi_K^s = -\frac{r_{ps}}{r_{ss}} \approx -\frac{in_0n}{n^2 - n_0^2} Q_y \tan\phi_t \frac{\cos\phi_i}{\cos(\phi_i - \phi_t)} \quad (2.29)$$

$$\Phi_K^p = -\frac{r_{sp}}{r_{ss}} \approx -\frac{in_0n}{n^2 - n_0^2} Q_y \tan\phi_t \frac{\cos\phi_i}{\cos(\phi_i + \phi_t)}. \quad (2.30)$$

As can be seen from a comparison of the longitudinal and the polar MOKE, the strength of the Kerr effect for the respective geometries only differs by a factor of $\tan\phi_t$. It follows that the longitudinal Kerr effect in first order of Q vanishes for small incidence angles and its strength is usually about a factor of 10 smaller than the polar MOKE due to a high refractive index of most ferromagnetic metals in the visible range. As a consequence, the magnetic properties of materials with an in-plane magnetization are rather studied in a reflectivity MOKE experiment at flat incidence angles, whereas materials with an out-of-plane magnetization are preferentially studied at normal incidence.

2.1.3 Transversal MOKE

Unlike the polar and longitudinal case, where the magnetization of the sample induces a change in the polarization, in a transversal geometry the magneto-optic response directly translates into an intensity modulation of the reflected light. In this geometry the surface normal is defined to be parallel to the z-axis, the plane of incidence lies within the y-z plane, and the magnetization aligns along the x-axis. Thus, the dielectric tensor adopts the following form and it can be shown that for this geometry the off-diagonal element ϵ_{yz} can be equivalently related to ϵ_{xy} , the origin of the magneto-optic response in the polar geometry [50]:

$$\overleftrightarrow{\epsilon}_t = \begin{pmatrix} \epsilon_{xx} & 0 & 0 \\ 0 & \epsilon_{yy} & \epsilon_{yz} \\ 0 & -\epsilon_{yz} & \epsilon_{yy} \end{pmatrix}. \quad (2.31)$$

Here, the solutions of the modes propagating in the magnetized material consists of two linearly polarized light waves, which are similar to the s- and p-polarized incident light waves, and whose refractive indices are determined to be:

$$n_s^2 = \epsilon_{xx} \quad \text{and} \quad n_p^2 = \epsilon_{yy} + \frac{\epsilon_{yz}^2}{\epsilon_{yy}}. \quad (2.32)$$

As the magnetization only couples to n_p , no magneto-optical Kerr effect is to be expected for a s-polarized incident wave. This fact is also expressed in the Fresnel reflection coefficient, where the s-wave reflection coefficient does not contain any magnetic contribution from the dielectric tensor and the cross-mode reflection coefficients are equal to zero, thus no change of the polarization is introduced:

$$r_{ss} = \frac{n_0 \cos \phi_i - n \cos \phi_t}{n_0 \cos \phi_i + n \cos \phi_t} \quad ; \quad r_{sp} = r_{ps} = 0 \quad (2.33)$$

$$r_{pp}^{\uparrow\downarrow} = \frac{n \cos \phi_i - n_0 \cos \phi_t}{n \cos \phi_i + n_0 \cos \phi_t} \pm \frac{2i n n_0 \cos \phi_i \sin \phi_t}{(n \cos \phi_i + n_0 \cos \phi_t)^2} Q_x. \quad (2.34)$$

The strength of the transversal MOKE signal, being odd in magnetization just like in the polar and longitudinal case, is commonly denoted by the normalized difference of the reflected intensity I for two inverted directions of the sample magnetization, here referred to as \uparrow and \downarrow . This magnetization reversal is achieved by an external magnetic field applied along the x-axis. This so-called magnetic asymmetry A is related to the Fresnel reflection coefficients r_{pp} and it is introduced to eliminate the non-magnetic contribution in the measured signal:

$$A = \frac{I_{\uparrow} - I_{\downarrow}}{I_{\uparrow} + I_{\downarrow}} = \frac{|r_{pp}^{\uparrow}|^2 - |r_{pp}^{\downarrow}|^2}{|r_{pp}^{\uparrow}|^2 + |r_{pp}^{\downarrow}|^2} \approx 2\Re\left(\frac{\sin 2\phi_i}{n^2 \cos^2 \phi_i - n_0^2 \cos^2 \phi_t} Q_x\right). \quad (2.35)$$

Just like in the longitudinal geometry the transversal MOKE disappears at normal incident angles. Because no polarization analysis of the reflected light is required, the experimental setup is significantly simplified. Even an unpolarized light source may be employed, because the s -polarized components of the light do not contribute to the magnetic signal. Nonetheless, a sensitive detection scheme has to be implemented, as the measured changes of the reflected intensity are usually below 1 % in the visible range, especially if a full magnetization reversal is not examined, such as in the visualization of surface magnetic domain structures [51].

2.2 MOKE and XMCD

Even though the X-ray Magnetic Circular Dichroism (XMCD) is commonly associated with transmission experiments in the soft x-ray regime [26], it is interesting to note that this magneto-optical effect can be easily related qualitatively as well as quantitatively to the Kerr effect. XMCD denotes a difference in absorption for circularly left and circularly right polarized photons in a ferromagnetic material. This phenomenon maximizes in a geometry where the magnetizations of the material under investigation aligns parallel to the helicity vector of the incident light. Similar to the T-MOKE, the strength of the dichroism can be described by the normalized difference A_{XMCD} of the measured signal intensities I_{\pm} associated with the absorption in the material for opposite photon helicities, here referred to as $+$ and $-$,

$$A_{XMCD} = \frac{I_+ - I_-}{I_+ + I_-} \quad \text{with} \quad I_{\pm} = e^{-\mu_{\pm}d}, \quad (2.36)$$

with d being the thickness of the magnetic material and μ_{\pm} the absorption coefficient. In a transmission experiment in a polar geometry, where the magnetization of the material points out of the surface plane and the incident light penetrates the sample along the surface normal, the absorption coefficient can be related to the imaginary part of the refractive index introduced in section 2.1.1 as well as the real part of the off-diagonal element of the dielectric tensor:

$$\mu_{\pm} = \Im(n_+ - n_-) = \Im(\sqrt{\epsilon_{xx} + i\epsilon_{xy}} - \sqrt{\epsilon_{xx} - i\epsilon_{xy}}) \approx \Re\left(\frac{\epsilon_{xy}}{\sqrt{\epsilon_{xx}}}\right). \quad (2.37)$$

Thus, the magneto-optic response in the case of the XMCD can be attributed to a non vanishing ϵ_{xy} in a magnetized sample and therefore directly connected to a reflectivity MOKE experiment by means of an elementary basis transformation.

2.3 MOKE in Multilayer Systems

The formulation of the Kerr effect for distinct reflection geometries outlined above can only be applied to a single magnetic layer bounded by vacuum. However, various authors have not only succeeded to extend this formulation to magnetic multilayer systems [52, 53], but also were they able to include surface as well as interfacial roughness in their description [54]. Their models can be used to realistically simulate the magneto-optical response of a multilayer system with an arbitrary direction of the magnetization and polarization of the incoming radiation for oblique incidence angles.

To this end, a 4×4 matrix formalism describes the response of a magnetic system comprising n layers by introducing a medium boundary matrix A_m and a propagation matrix D_m . The former accounts for the conservation of the tangential components of the electric and magnetic fields at the interface of medium m and $m + 1$, whereas the latter considers the absorption and dispersion of the radiation within the layer m . Thus, the polarization state at the final medium P_f of an electro-magnetic wave propagating through all layers can be related to the initial polarization state P_i :

$$P_i = A_i^{-1} \prod_{m=1}^n (A_m D_m A_m^{-1}) A_f P_f = M P_f \quad \text{with} \quad M = \begin{pmatrix} G & H \\ I & J \end{pmatrix}, \quad (2.38)$$

G, **H**, **I** and **J** being 2×2 matrices containing reflection coefficient for the electric and magnetic field of the wave interacting with the multilayer. The solution of the Fresnel reflection coefficients for the entire multilayer system can be obtained from:

$$\begin{pmatrix} r_{ss} & r_{sp} \\ r_{ps} & r_{pp} \end{pmatrix} = I G^{-1}, \quad (2.39)$$

provided that the thickness and the magneto-optical constants for all the individual layers are known. Within this formulation the roughness has been accounted for by multiplying the reflection amplitude coefficient $r^m = \frac{I_{ii}^m}{G_{ii}^m} = \frac{H_{ii}^m}{J_{ii}^m}$ of an individual layer m by a roughness modeling factor χ^m , that effectively decreases the amplitude of the reflected wave at the interface. The computer code, provided for this thesis by the courtesy of BESSY, was capable of considering two basic roughness models. In the case of the Névot–Croce model [55, 56], χ^m can be written as:

$$\chi^m = e^{-2\sigma_m^2 k_m k_{m+1}} \quad \text{with} \quad k_m = \sqrt{\frac{2\pi}{\lambda \sin \theta_m}}, \quad (2.40)$$

whereas in the Debye-Waller model k_{m+1} is simply replaced for k_m [57], which in both cases represents the z-component of the wave vector incident at an angle θ_m propagating in the layer m with a wavelength of λ , and σ_m denotes the root mean squared roughness.

2.4 The Classical Oscillator Model

The previous sections exemplified that the magneto-optical Kerr effect is directly related to the off-diagonal elements of the dielectric tensor, which in first approximation are antisymmetric in the magnetization. Even though the MOKE can be fully described by the introduction of these phenomenological material related quantities within a magneto-optical framework, it is possible to link these components to a simplified model in order to obtain a qualitative picture of the microscopic mechanisms behind the magneto-optic interaction of light and matter. In the Lorentz-Drude model, the electrons of a solid are assumed to respond to a periodic electric field \vec{E} of an incident electro-magnetic wave oscillating with a frequency ω as well as a static external magnetic field \vec{B} like a classical damped oscillator, which is subject to an oscillatory electrical as well as a Lorentzian force [47]. Thus, the equation of motion is:

$$\ddot{\vec{r}} + \gamma \dot{\vec{r}} + \omega_0^2 \vec{r} = \frac{e}{m} (\vec{E} + \dot{\vec{r}} \times \vec{B}), \quad (2.41)$$

with \vec{r} being the displacement of the electrons, each of which has a mass m and a charge e , whereas ω_0 denotes the resonance frequency of the undamped oscillator and γ represents the damping of the solid.

In this picture, the electric field of the incident electro-magnetic wave induces an oscillation of the polarization in the solid. The magnetic field forces the electrons in a polar and longitudinal geometry on elliptical trajectories, along the component perpendicular to the magnetization, which results in a polarization change of reflected light associated with the emitted dipole radiation. In the transversal case, on the other hand, the magnetization causes only a reduction in the amplitude of the electron oscillation, which explains that only the intensity of the reflected light changes as a function on the applied magnetic field. Moreover, no Kerr effect is expected for an incident s-polarized wave, as the magnetization is parallel to the dipole oscillation axis and the Lorentz force and therefore the magnetic influence disappears.

Under the assumption that the magnetic field is applied along the z-axis and the electro-magnetic wave is at normal incidence (polar geometry), the dielectric tensor is given by $\overleftrightarrow{\epsilon}_p$ (see equation 2.18) and the solutions for the individual components are determined to be [46]:

$$\epsilon_{zz} = 1 + \frac{e^2 N}{\epsilon_0 m V} \frac{1}{(\omega_0^2 - \omega^2 - i \gamma \omega)} \quad (2.42)$$

$$\epsilon_{xx} = 1 + \frac{e^2 N}{\epsilon_0 m V} \frac{\omega_0^2 - \omega^2 - i \gamma \omega}{(\omega_0^2 - \omega^2 - i \gamma \omega) - 4\omega^2 \omega_L^2} \quad (2.43)$$

$$\epsilon_{xy} = \frac{e^2 N}{\epsilon_0 m V} \frac{-i \omega \omega_L}{(\omega_0^2 - \omega^2 - i \gamma \omega) - 4\omega^2 \omega_L^2}, \quad (2.44)$$

with N being the number of excited dipoles in a volume V and $\omega_L = \frac{eB}{2m}$ the Larmor frequency. It is evident from these equations that the linear magnetization dependence of the dielectric tensor is confined to its off-diagonal components, which thereby allows for an optical measurement of the magnetization and its orientation in the sample. Furthermore, it is interesting to note that the influence of the magnetization on the magneto-optical response of the material is enhanced close to the resonance frequency of the polarization oscillation in the solid. The macroscopic nature of the solutions to the Fresnel equation 2.15 and this resonant behavior already give a sufficient justification for this magneto-optical framework to be readily applied to resonant magneto-optical phenomena at high photon energies.

2.5 Quantum Mechanical Considerations

Even though the description of the Kerr effect in the classical oscillator model already provides a basic understanding of this magneto-optical phenomenon, the underlying microscopic mechanisms behind the MOKE have to be grasped beyond the notion of the Lorentzian force acting on the electronic system excited by the impinging photon field. In a quantum mechanical picture, it is possible to provide the connection of ϵ_{ij} to the electronic structure of the solid via electric dipole transitions. Regarding the previously discussed origin of magneto-optical effects, it is convenient to focus on the absorptive part of the off-diagonal tensor elements in a circular basis and express the dielectric tensor via the optical conductivity $\sigma_{ij} = (i\omega/4\pi)(\epsilon_{ij} - \delta_{ij}) = \sigma_{xy}^{(1)} + i\sigma_{xy}^{(2)}$. By means of the Kramers-Kronig relations, the absorptive part $\sigma_{xy}^{(2)}$ of the off-diagonal conductivity tensor element can be related to the spectral integral of the dispersive part $\sigma_{xy}^{(1)}$, and vice versa. It can be shown via Fermi's golden rule that the former tensor element adapts the following form [58]:

$$\sigma_{xy}^{(2)}(\omega) = \frac{\pi e^2}{4\hbar\omega m^2 \Omega} \sum_{i,f} f(\epsilon_i)[1 - f(\epsilon_f)] [|\langle i|p_-|f\rangle|^2 - |\langle i|p_+|f\rangle|^2] \delta(\omega_{fi} - \omega), \quad (2.45)$$

with $f(\epsilon)$ being the Fermi-Dirac distribution, $\hbar\omega_{fi} = \epsilon_f - \epsilon_i$ representing the energy difference of the band energies ϵ and Ω denoting the volume of the unit cell. The momentum operators for right and left circularly polarized light are represented by $p_{\pm} = p_x \pm p_y$, which govern the allowed optical transitions between the occupied initial state $|i\rangle$ and the unoccupied final state $|f\rangle$. Here, $\delta(\omega_{fi} - \omega)$ accounts for the conservation of the energy in this photo-absorption process.

A discussion of equation 2.45 is assisted by figure 2.2, which schematically illustrates the energy levels of a ferromagnetic material (left) as well as a paramagnetic material (right) in an atomic model. All optical transitions from a $d_{xz,yz}$ level

($l = 2, m_l = \pm 1$) into a p_z level ($l = 1, m_l = 0$) for circularly polarized light are displayed and the corresponding dipole selection rules are:

$$\Delta l = \pm 1 \quad \Delta m_l = \pm 1. \quad (2.46)$$

As indicated in the left graph of figure 2.2, the energy levels for spin up and spin down electrons, here referred to as \uparrow and \downarrow , are split by the exchange energy Δ_{ex} , which commonly amounts to 1 eV to 2 eV. In addition, the initially degenerate $d_{xz,yz}$ level is split by spin-orbit-coupling, whose energy Δ_{SO} happens to be a few tens of electron volts in the case of valence electrons of 3d transition metals. Considering both electron spin species, the dipole selection rules allow for transitions from $d_{(x-iy)z}$ levels into the p_z level with right circularly polarized light, here referred to as +, and for transitions from the $d_{(x+iy)z}$ levels into the p_z level with left circularly polarized light, here referred to as -. Since the spin is conserved in this excitation process and all d levels possess a distinct energy, left and right circularly polarized light is absorbed differently in a ferromagnetic material resulting in a magneto-dichroic signal. This relationship is reflected in differing spin-dependent transition matrix elements for right and left circularly polarized light in equation 2.45 resulting in a finite off-diagonal tensor element and therefore in a rotation of the incident polarization.

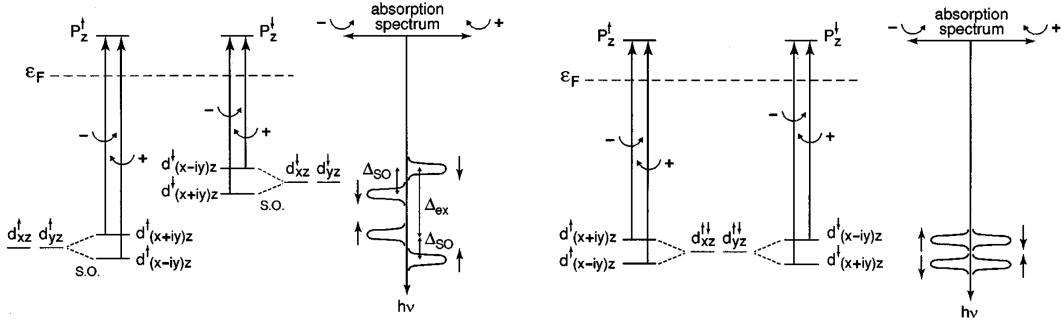


Figure 2.2: Illustration of the energy levels in a bulk ferromagnet on the left and in a bulk paramagnet on the right, showing the electric dipolar optical transitions for left and right circular light. The corresponding absorption spectra versus photon energy are shown on the right; the solid and dashed lines correspond to spin up and spin down transitions, respectively - adapted from [58].

As indicated in the right graph of figure 2.2, the d levels in a paramagnetic material exhibit no exchange splitting provided that an external magnetic field is not applied. Therefore, the absorption for right and left circularly polarized light is the same resulting in a vanishing Kerr effect in spite of spin-orbit split energy levels. Similarly, it is clear that even if an exchange splitting is present, no difference in the absorption

behavior can be expected in the absence of spin-orbit coupling. It can be concluded that the Kerr effect arises from the simultaneous occurrence of exchange splitting and spin-orbit coupling, the former of which lifts the energetic degeneracy of the latter.

The discrete energy levels in figure 2.2 suggest the Kerr effect to reach up to 100%. However, it is the width of the energy bands in a real solid state body, which results in a broad absorption spectrum and a reduction of the Kerr effect amounting to usually less than 1° for wavelengths above 250 nm.

It is interesting to note that the conductivity tensor can also provide a relationship between the magneto-optical spectrum and the orbital moment. Within a single-particle formulation, it can be shown that the integrated absorptive part of the off-diagonal conductivity tensor can be explicitly linked to the total angular momentum by the following expression [59, 60]:

$$\int_0^\infty d\omega \sigma_{xy}^{(2)}(\omega) \approx -\frac{\pi e^2}{2mV} \frac{\langle l_z \rangle}{\hbar} - R_{xy}, \quad (2.47)$$

with $\langle l_z \rangle$ being the total angular momentum in the volume V , which is related to the z -component of the total orbital moment by $M_{l_z} = -\langle l_z \rangle \mu_B / \hbar$. The remainder R_{xy} can be shown to vanish at zero temperature, but the fact that the integral amounts up to only a part of the orbital moment is a hindrance for practical applications. On the other hand, test calculations show that $\langle l_z \rangle$ represents the major contribution to the spectral integral and the remainder is small, exemplifying that the off-diagonal conductivity and the orbital moment are closely related quantities.

2.6 T-MOKE at High Photon Energies

In order to extract information about the sample magnetization in MOKE experiments in the visible range, changes in the polarization state of the reflected light are usually analyzed in a polar or longitudinal geometry. In contrast to this, most magnetic reflectivity experiments in the EUV and soft x-ray region can readily be performed in a transversal geometry (T-MOKE) due to a sizable intensity modulation that can be exploited for magnetic contrast generation. Moreover, the complexity of the experimental setup is significantly reduced, as no polarization analysis is required, which necessitates a sophisticated optical apparatus at these wavelengths.

The element-selective nature and the strength of the dichroism originates from a large enhancement of the reflected light intensity, if the energy of the incident beam is tuned to the absorption edges of the material under investigation [61]. This strongly resonant behavior involves low-order electric multipole transitions between core levels and unoccupied states of the valence band which results in both element-selectivity and magnetic sensitivity in the presence of spin-orbit coupling and exchange interaction.

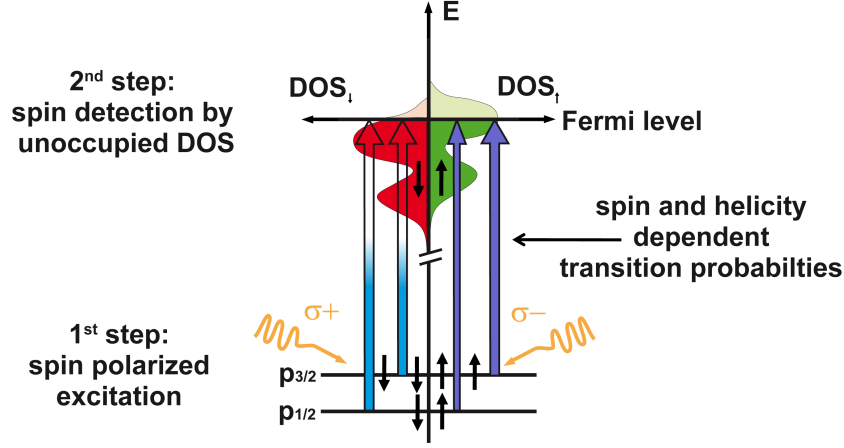


Figure 2.3: Illustration of the spin-dependent absorption in the two-step process

In a simple picture, illustrated in figure 2.3, the magnetic sensitivity originates from the interplay of two mechanisms, which are therefore often referred to as a "two-step-process" [62]. In the first step, the exchange interaction energetically splits the magnetic sublevels m_J of both the upper and lower states, which are involved in the photo-excitation process [63]. This results in spin-split core states and a spin-split density of the valence states. Thus, a core electron which is excited by a photon becomes spin-polarized depending on the employed photon helicity $\sigma\pm$. In the second step, the spin-orbit coupling in either the lower or the upper states (or in both) causes the optical interband transitions to become spin dependent, which is also known as optical spin orientation [64]. As the core electron is excited into an already spin-polarized empty state, which serves as a spin detector, the strength of the transition matrix element for transitions from each sublevel m_J is now determined by both the magnetization direction and the light polarization. The resulting difference in absorption of left and right circularly polarized light leads to the magneto-optical response, just like in the case of MOKE. Even though the origin of this magneto-optic interaction differs for the respective wavelength regimes, a resonant core level excitation of the electron system in contrast to an interband transition in the visible range, the mathematical description outlined above holds for a large spectral range. The underlying quantum mechanical processes can be suitably described by response functions of the material, through which phenomenological optical constants can be expressed. Following the discussion of the quantum mechanical origin of magneto-optical phenomena, it is immediately clear that the sharp line widths of the core levels must result in a much larger magnetic contrast as compared to a pure valence band excitation, which indeed attains up to several tens of percent at high photon energies.

In addition to the element selective nature of the magneto-dichroic signal, a lateral resolution down to a few nanometers can be obtained if the experiment is shifted away from the optical regime to shorter wavelengths [65]. For the 3d transition metals Fe, Co and Ni, which this study focuses on, enhanced magnetic resonances occur at $L_{2,3}$ absorption edges in the range of 500 eV to 950 eV in the soft x-ray region and at the $M_{2,3}$ absorption edges in the range of 50 eV to 70 eV in the EUV by involving mainly $2p \rightarrow 3d$ and $3p \rightarrow 3d$ transitions, respectively.

2.6.1 EUV vs. Soft X-Ray Regime

Magnetic investigations exploiting magneto-dichroic phenomena in the soft x-ray range have been performed about a decade earlier than comparable magneto-optic experiments in the extreme ultraviolet range. One reason is a result of the energetic proximity of the Fe, Co and Ni M absorption edges suggesting that the element-specific response of a magnetic system can be separated more clearly at the L absorption edges. For the same reason, an experimental determination of the local magnetic moments, especially a separation of orbital and spin momentum, by means of XMCD transmission experiments and the application of sum rules was assumed to be only feasible at the L absorption edges. First experiments on NiPd alloys confirmed significant discrepancies in the calculations of the orbital momentum by the application of sum rules at their respective M and L edges, thereby excluding this powerful technique to be applied in the extreme ultraviolet range [66]. Thus, EUV magneto-optical studies have mostly escaped the attention of the magnetic community and synchrotron radiation facilities started to dedicated their beamlines to photon energies in the soft x-ray region.

Nonetheless, the EUV spectral range offers certain advantages over the soft x-ray regime with respect to element-selective magneto-optical studies in reflection geometries. Several experiments have already shown that magnetic investigations of single films by resonantly scattered EUV light at the M absorption edges of transition metals [33–37] and even at the N absorption edges of the lanthanide series [67, 68] yield very strong magneto-dichroic signals. Moreover, studies of the Faraday rotation and the Voigt effect at the M and L absorption edges of Fe, Co, and Ni reveal that magneto-optical constants and thus responses at the M edges are as large as those at the L edges [37, 69, 70]. However, since the magneto-optical information is carried by the optical signal, it is the high absorbance of most materials, at angles where the magneto-dichroic signal maximizes in the EUV, which gives no rise to a magnetic contrast in comparable soft x-ray experiments. In a T-MOKE geometry, for example, the maximum of the magneto-dichroic response is located around the Brewster angle, i.e. incoming and outgoing light beam enclose an angle of $\sim 90^\circ$. Under these conditions there is still a sizable reflectance of the order of $R \sim 10^{-4}$, which ensures a reasonable signal-to-noise ratio in the EUV. Here, a magnetic contrast of up to 100 % can be obtained allowing for sensitive measurements of weak magnetizations originating, for

example, from very thin films and nanoscale structures. In the soft x-ray regime, on the other hand, the light penetrates deeper into the sample and the reflectivity drops off much faster with increasing incidence angle θ , reaching values of $R \sim 10^{-10} - 10^{-11}$ at $\theta = 45^\circ$ [71]. Therefore, in the soft x-ray regime magnetic information can only be obtained at grazing incidence angles, which adds to the complexity of the experimental setup and reduces the magnetic contrast that can be utilized.

Another aspect concerns optical interference effects arising in the sample. Typical structural dimensions of a sample system, such as the individual layer thickness in a multilayer stack, and the wavelength corresponding to a transition metal L edge are of similar magnitude, i.e. of the order of a few nm (1.59 nm for the Co L_3 absorption edge at 778.1 eV). In a reflectivity experiment at these photon energies, the multilayer acts as a superlattice, resulting in a relatively complex interference pattern mixing structural and magnetic periodicities. As a consequence, the reflected intensity exhibits a strong angular modulation of the magneto-dichroic signal and structural and magnetic properties cannot be separated easily [54]. In the case of transition metal M edges, where the wavelength is about one order of magnitude larger (20.6 nm for the Co M absorption edge at 60.2 eV), structurally induced interferences in the magnetic signal are less pronounced, simplifying the interpretation in this respect. For the same reason, surface and interface roughness influence the magnetic signal to a much smaller extent. Moreover, due to a smaller penetration depth of the EUV radiation, Kiessig fringes [72] - resonances between surface and substrate - do not occur, further facilitating the interpretation.

Furthermore, a closer look into EUV magneto-optics is more than justified, since laser-based light sources can nowadays reach photon energies of up to 100 eV with moderate effort. Recent advancements in laser amplifier technology have brought about reliable table-top light sources, which are able to produce ultrashort EUV light pulses exploiting a highly nonlinear conversion process (Higher Harmonic Generation - HHG) [38, 39]. By this means the generated light retains the properties of the driving laser resulting in spatially coherent femtosecond pulses with energies ranging into the soft x-ray region [40]. Due to the pulsed and coherent nature of the emitted radiation, HHG-based light sources may serve as compact tools for element-selective investigations of magnetic properties on femtosecond and nanometer scales in a laboratory environment [41, 42]. Because of this outstanding prospect, the discussed advantages and the simple fact that only little attention has been paid to the EUV region, it is the purpose of the following experiments to explore its potential as a magnetic contrast mechanism. By tuning the photon energy to the M absorption edges of Fe, Co and Ni in a T-MOKE reflectivity experiment, magnetic investigations focusing on magnetic multilayer and alloy model systems should prove whether an element-selective response can be obtained. In addition, the feasibility of time-resolved experiments should be determined by employing both synchrotron as well as laser based EUV radiation sources and by utilizing their distinct time structures.

Chapter 3

Instrumentation and Methods

This chapter deals with the experimental instrumentation as well as methods, which were employed and partly developed for investigations of magnetic heterostructures within the context of this thesis in both the visible and the extreme ultraviolet range. As the principles behind the involved equipment and techniques cover more than one diverse area of expertise, only brief descriptions can be given. For more details it is referred to more elaborated literature [73–75].

In the following, the attention is firstly focused on reflectometry performed at the synchrotron, which has been used to statically measure the magneto-optical response of various heterogeneous, ferromagnetic systems. An experimental extension into the time domain, by studying the response of magnetic films to laser excitation in a pump-probe approach, is introduced thereafter. Secondly, both static and time-resolved laser based MOKE setups are presented serving as reference experiments to measurements performed in the EUV. Finally, the principle as well as the apparatus behind a table-top soft x-ray source is introduced combining the aforementioned approaches in a laboratory environment.

3.1 X-Ray Generation at the Synchrotron

Synchrotron radiation was historically considered as an unwelcomed byproduct of circular accelerators designed for particle collisions in the field of nuclear and elementary particle physics. Due to the high brilliance, a quantity introduced to describe the divergence and intensity of the emitted radiation, electron storage rings are nowadays constructed specifically to provide synchrotron radiation which is dedicated to various fundamental and applied scientific questions.

The low divergence of the generated x-rays originates from the directed emission characteristic of the electrons traveling at relativistic speeds on a curved path in the synchrotron. Assuming that the absolute value of the electron velocity $|v|$ remains constant for a circular trajectory in the electron storage ring, the electrons emit radiation along a tangential cone of their orbit, as the speed of the electrons approaches

the speed of light c . Figure 3.1 illustrates how the angular emission characteristic changes with increasing speed from the well-known $\sin^2\theta$ dependence of a classical dipole moving at non-relativistic velocities to a radiation cone with an opening angle of $\theta \approx 1/\gamma$, with gamma denoting the Lorentz factor $1/\sqrt{1-\beta^2}$ and $\beta = v/c$. As a consequence, the divergence of a beam resulting from an electron traveling with an energy of a few GeVs decreases to about 0.1 mrad. At the synchrotron BESSY in Berlin, for example, where the measurements for this study have been performed, a γ of 3320 yields a θ of 0.15 mrad (0.01°).

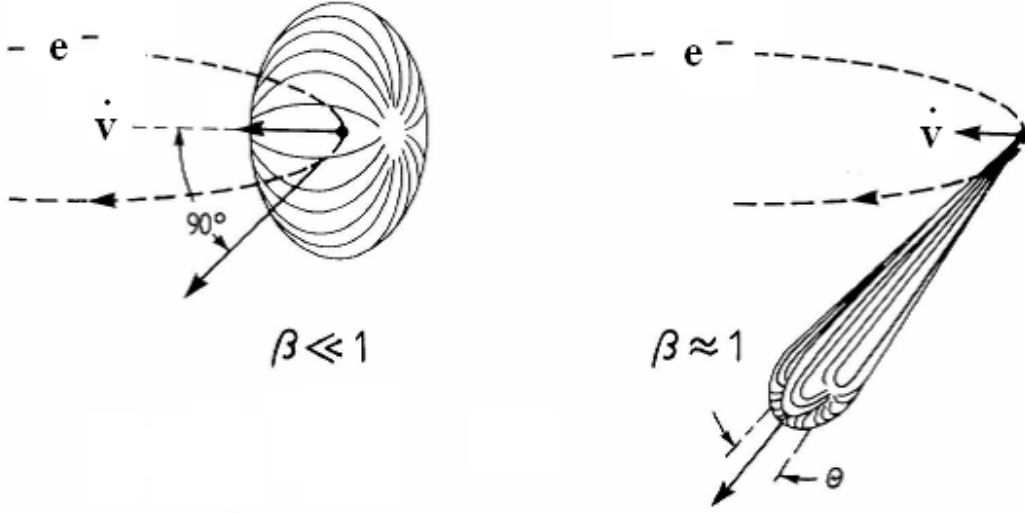


Figure 3.1: The emission characteristic of an electron on a circular trajectory in a magnetic field moving at non-relativistic (left) and relativistic (right) speed – adopted from [76].

As the emission angle of the generated radiation decreases, the intensity and therefore the brilliance is enhanced naturally. However, in order to further increase the x-ray intensity, the path of the electron is commonly modulated by insertion devices, such as wigglers and undulators. These magnetic chicanes are located at straight sections of a storage ring, which is usually built in a polygon shape with bending magnets at its corners connecting all straight sections. As is illustrated in figure 3.2, insertion devices comprise a periodic array of permanent magnets modulating the trajectory of the electrons traversing this linear structure in an oscillatory manner. Intuitively, the polarization of the generated x-rays is determined by the plane, in which the electrons oscillate, here the horizontal plane. In contrast to a simple bending magnet, which is constructed to provide a homogeneous magnetic field B to bend the path of the electron on a circular trajectory, the total deviation of the electron path in a wiggler

and an undulator is reduced to a minimum by a sequence of relatively short magnets producing an alternating magnetic field with a period of λ_u .

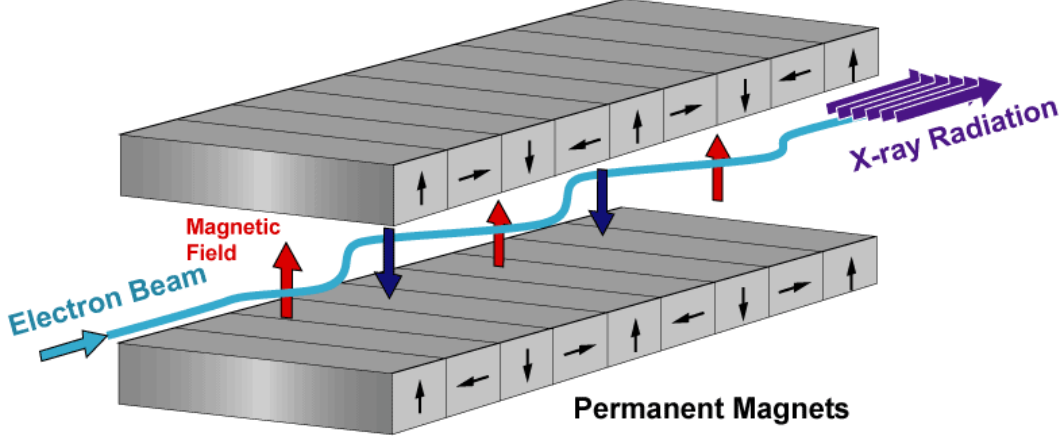


Figure 3.2: Schematic of a wiggler/undulator structure – adopted from [77].

The deflection parameter K is a quantity to describe the deviation of the electron path from the central long axis of the insertion device and it is stated to distinguish between a wiggler, having a $K \gg 1$, and an undulator, having a $K \lesssim 1$ with [73]:

$$K = \frac{e\lambda_u B}{2\pi m_e c} = 0.934\lambda_u[cm]B[T]. \quad (3.1)$$

The emitted photons of the undulating electron add from each magnetic period of the insertion device, resulting in a large increase of the photon flux. In the case of a wiggler the emitted intensity scales with $2N$, with N denoting the number of magnetic periods, and in the case of an undulator with N^2 as compared to the intensity arising from a bending magnet. This difference can be attributed to a larger deflection of the electron path in a wiggler in comparison to an undulator resulting in a series of incoherent x-ray bursts rather than a coherent superposition of the photon field in the undulator. Therefore, similar to a bending magnet, a wiggler emits a rather continuous spectrum, whereas an undulator spectrum consists of peak shaped harmonics. For a large number of magnetic periods, constructive interference at a wavelength λ can be observed in the order of the n^{th} harmonic for the following condition [73]:

$$n\lambda = \frac{\lambda_u}{2\gamma^2} \left(1 + \frac{K^2}{2} + \gamma^2\vartheta^2 \right) \quad \text{with } n = 1, 2, 3, \dots, \quad (3.2)$$

and ϑ being the observation angle with respect to the undulator axis. The first factor of this so-called *undulator equation* describes how short wavelengths are generated by a relativistic electron, whereas the second factor accounts for the tunability of the x-rays. This is accomplished by varying the undulator gap and thus the magnetic field rather than γ , because changing the gap only affects the experimental station as compared to the electron orbit of the entire ring. The third factor describes the off-axis angular dependent aberration of the wavelength related to a relativistic Doppler-shift and a distinct dipole radiation pattern. As a consequence, only the fundamental first harmonic as well as odd integers thereof can be observed on the central undulator axis, along which a beamline is usually positioned.

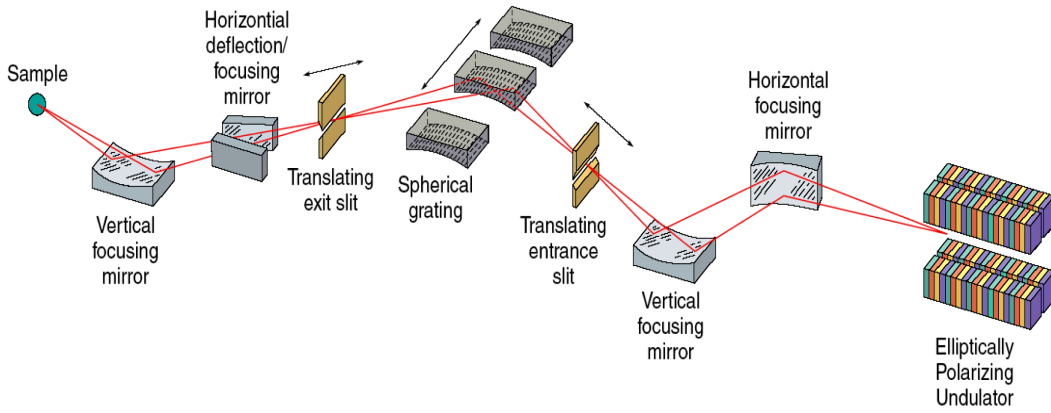


Figure 3.3: Schematics of a typical soft x-ray beamline, whose length amounts to about 35 m from the undulator to the sample – adopted from [73].

Figure 3.3 schematically depicts the instrumentation of a beamline serving to guide the generated photons from the undulator to the sample. The set up of the optical components shown in this illustration resembles the undulator beamline UE56/1-SGM of the synchrotron radiation facility BESSY II, where the magnetic reflectivity measurements for this study have been performed with an energy resolution of 0.1 eV and a degree of linear polarization exceeding 99 %.

To capture as many photons as possible, vertical and horizontal focusing mirrors behind the undulator are used to image the point source, the emitted radiation from the moving electrons inside the ring, onto the entrance slit of the monochromator. To be able to tune the photon energy, a spherical grating is introduced imaging the entrance slit onto the exit slit. As the photon energy is supposed to be tuned over a wide energy range, the monochromator consists of a set of interchangeable gratings

with various line densities. Behind the exit slit, whose width can be adjusted to determine the desired energy resolution, the beam diverges again and a further pair of mirrors is used to focus it onto the sample. Thus, the synchrotron beam can be focused down to a spot size of approximately $100 \times 100 \mu\text{m}^2$ at the sample surface. The photon flux of this soft x-ray beamline covering a wide energy range of 55 eV to 1300 eV can be extracted from the figure below.

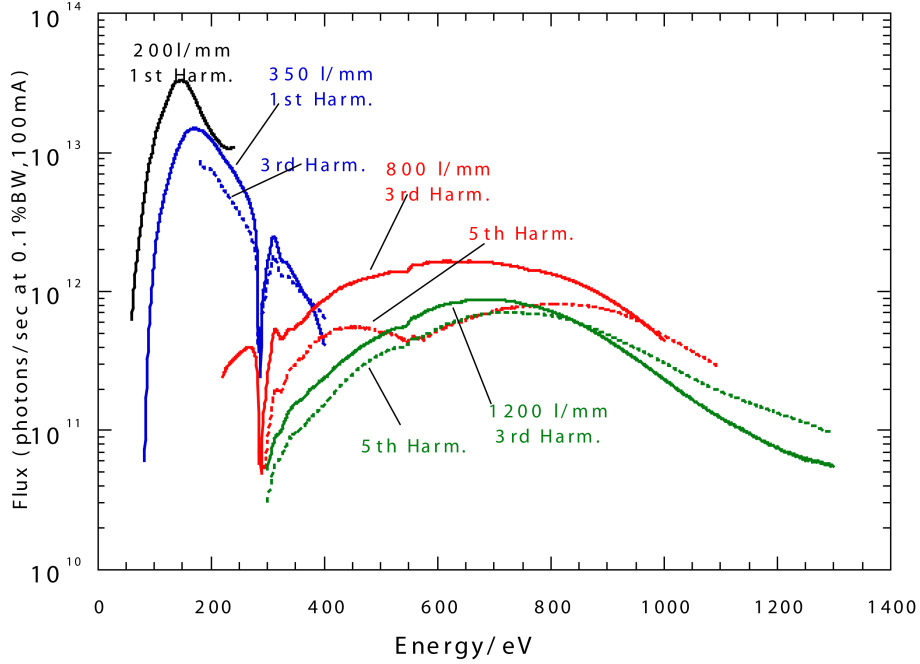


Figure 3.4: Photon flux of the BESSY undulator beamline UE56/1-SGM at the sample surface, which was measured for 4 interchangeable gratings with a line density of 200, 350, 800 and 1200 lines/mm [76].

3.2 UHV Reflectometer

The sample was placed into a dedicated ultrahigh vacuum (UHV) reflectometer, depicted in figure 3.5, which is based on a steel pipe with a diameter of about 100 mm. CF 40 and CF 60 flanges are welded to this custom designed body allowing for the attachment of a turbo pump (Pfeifer - TMU 071P - marked green), a full range vacuum gauge (Pfeifer - PKR 261 - marked brown), an titanium ion pump (Gamma Vacuum - TiTan-IGP - not shown) and an UHV compatible SMA electrical feed-through. The sample holder, vertically sandwiched by two magnetic coils, is mounted to the axis of

a rotational manipulator that can be translated in the x, y and z direction in a range of about 25 mm. For measurements this manipulator is placed into the body, which is connected to and rests on a robust framework made from standard Al profiles. The photodiode is connected to an additional rotational manipulator, which is attached via a CF 100 flange to the bottom of this reflectometer

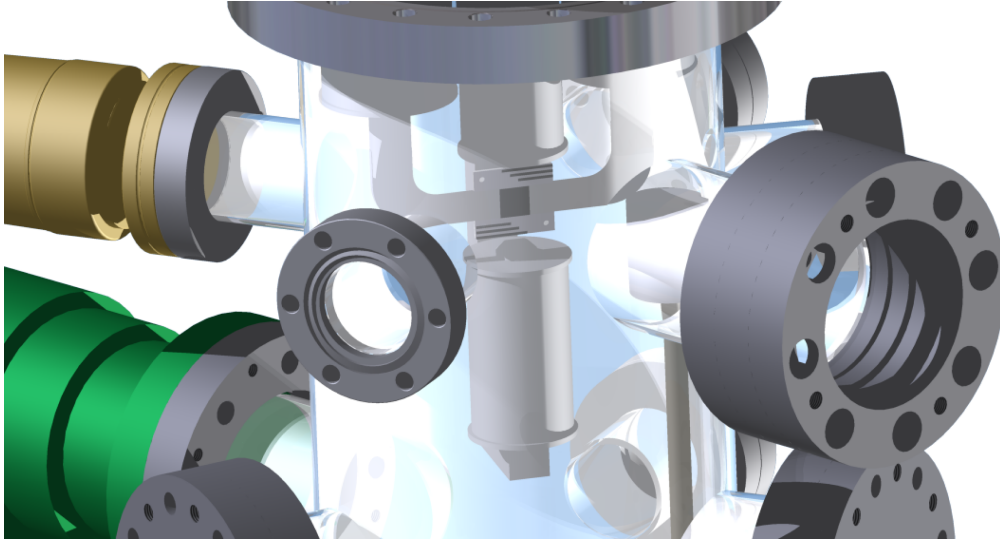


Figure 3.5: UHV reflectometer designed and built at the Forschungszentrum Jülich.

Both rotational manipulators allow for manual $\theta - 2\theta$ scans in a horizontal plane with the angle of incidence θ ranging from 0° to 90° and an accuracy of 0.1° . For static measurements of the magneto-optical response, the intensity of the EUV light reflected off the sample was detected by a Schottky-type GaAsP photodiode (Hamamatsu - G1127) directly connected to a sensitive amperemeter (Keithley - 6517A). The calibrated photodiode was operated in reverse bias, an amplification regime where the generated photo current responds linearly to the impinging photon intensity. In order to block out the visible stray light the diode was usually covered by a 200 nm thick Al filter. A set of vertically mounted coils was capable to generate a static magnetic field of up to ± 140 mT at a driving current of 10 A provided by a bipolar power supply (Kepco - BOP 20/20). A standard laptop equipped with a USB/GPIB adapter was used to control the experiment, i.e., to adjust the variations of the undulator gap and monochromator angle changing the photon energy, to set the coil current vertically applying a magnetic field to the sample, to read out the amperemeter, to save the data and to synchronize all devices by means of a LabView controlled IEEE-Bus.

This compact design results in a simple and flexible reflectometer that can be easily operated and comfortably transported due to its light weight of less than 100 kg. Because of its small volume, a vacuum of less than 10^{-7} mbar can be obtained within 12 hours, which is sufficient for the chamber to be connected to any synchrotron beamline. In the initial experiments a sample was changed by breaking the vacuum and removing the sample manipulator. Recently, this major drawback has been overcome by redesigning the sample holder to admit standard sample mounts of the Omicron type and attaching a small transfer chamber including a separate turbo pump, a wobble stick and a sample magazine with enough space for six samples via an UHV valve to the reflectometer. As a consequence, the allocated blocks of measurement time can be optimally used in the nearly 24/7 operation of the synchrotron, since changing a sample is reduced from 12 hours to 15 min and the transfer chamber can be reloaded and evacuated within a couple of hours.

3.3 Time-Resolved Experiments at the Synchrotron

The temporal structure of the synchrotron light in combination with a pulsed laser can be exploited to element-selectively perform time-resolved experiments at the synchrotron. The emitted radiation and therefore lost kinetic energy of an electron circling the storage ring is replenished within a microwave cavity. The electric field structure of the microwave accelerating the electrons is the reason why the storage ring cannot be filled continuously. Rather, bunches of electrons are injected into so-called buckets of the microwave. In the case of the synchrotron BESSY in Berlin the klystron oscillates with a frequency of 500 MHz and thereby determines the minimum spacing of two electron bunches, i.e. 2 ns.

Here, two distinct operation modes are usually offered to the user which differ in the filling pattern of the ring. In the multibunch mode a large portion of the buckets is filled with electrons, whereas a gap of about 100 ns remains unfilled in the middle of which a so called hybrid-bunch is placed. This hybrid-bunch is usually filled with about ten times more electrons than the normal bunches. In contrast to the multibunch mode, only one bunch is filled into the ring in the single-bunch mode. A normal electron bunch contains approximately 10^{10} electrons and its local spread is optimized to provide a short burst of x-rays when traversing the insertion device. The resulting pulse length happens to be in the range of 30 ps for the normal bunches and 50 ps to 100 ps for the hybrid bunch. The former operation mode is chosen for static measurements due to a much larger average electron current and thus photon flux as compared to the latter operation mode, which is preferred for time-resolved experiments because of its well defined temporal structure. A schematic summary of the above mentioned can be found in figure 3.6.

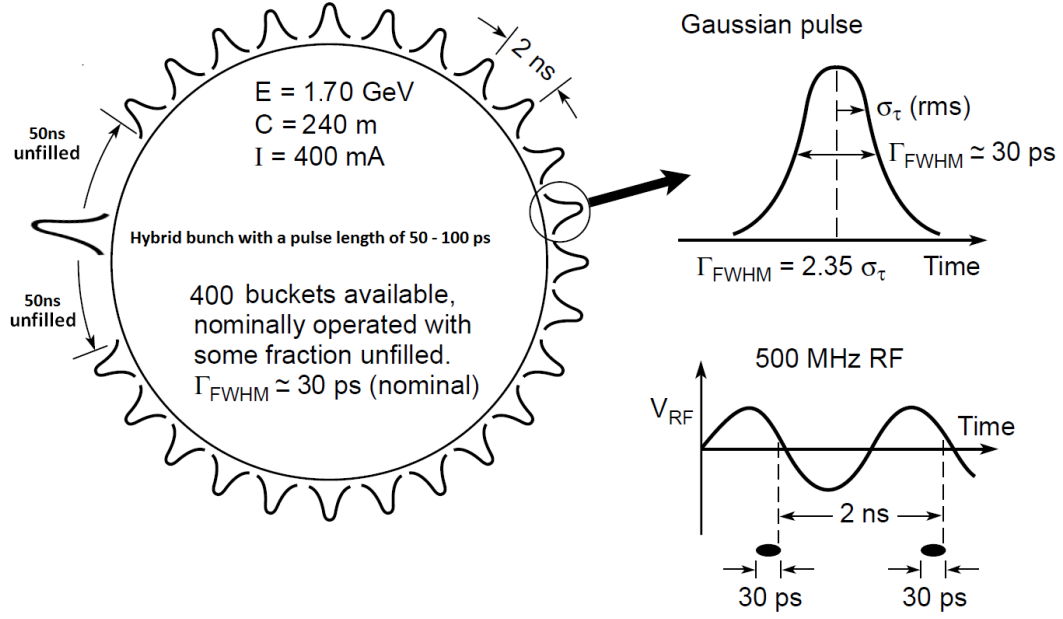


Figure 3.6: Temporal structure of the electron bunches in the multi-bunch mode at BESSY: in the microwave cavity (bottom right), around the ring (left) and of a normal single bunch (top right) - adopted from [73].

The pulse structure of the synchrotron radiation tuned to the absorption edge of an element under investigation was used to element-selectively probe the dynamic response of a magnetic system to an excitation by pump pulses from a laser. For this pump-probe experiment, a Ti:Sapphire based oscillator was employed (Femto Lasers - Synergy) delivering pulses with a pulse length of about 20 fs (FWHM) at a central wavelength of 800 nm and a maximum energy of 7 nJ at a repetition rate of 100 MHz. To synchronize the pulse trains of the laser and the storage ring, the repetition rate of the laser, which is determined by the length of the optical cavity [78], was chosen to be an integer fraction of the microwave klystron frequency, the repetition rate of the synchrotron. Dedicated electronics (Femto Laser - Femtolock) locked to the 500 MHz bunch clock adjusted the length of the laser cavity by means of a piezo-electrically mounted silver mirror establishing a fixed phase relation between the pulses from both light sources. To this end, the repetition rate of the laser was determined by an internal photodiode, which was electronically multiplied by five and subtracted from the reference signal of the bunch clock. A PID controller drove the optical mirror inside the laser cavity such that the difference signal equaled zero, thus synchronizing the x-ray and laser pulses with a temporal jitter below 1 ps.

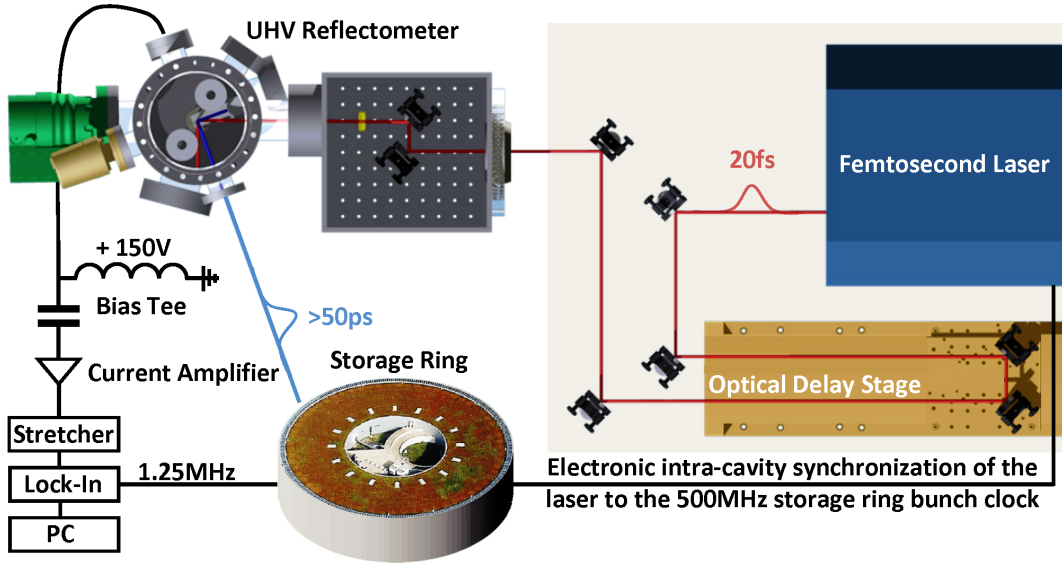


Figure 3.7: Optical setup of the pump-probe experiment at BESSY (top view).

A schematic drawing of the pump-probe experiment from a top-view can be found in figure 3.7. On the top left side of this picture, the reflectometer from figure 3.5 can be seen and blue as well as red lines indicate how synchrotron and laser pulses enter the chamber, respectively. This reflectometer is connected to the refocusing chamber of the beamline, not shown here for the purpose of illustration, by which the focus of the x-rays can be comfortably moved to the sample. The laser beam, which is emitted by the oscillator, travels over an optical delay stage into a black box firmly attached to the reflectometer. This box contains two steering mirrors mounted to a small optical breadboard and a plano-convex lens with a focal length of 20 cm. The proximity of these optical components to the sample is necessary to precisely guide the laser focus onto the sample and to ensure a spatial overlap of the x-ray as well as visible light at the order of a few tens of microns. The alignment procedure is usually monitored by a CCD camera (not shown here). The translation stage (Newport - IMS600PP) having an accuracy of about $1\text{ }\mu\text{m}$ and a traveling distance of 60 cm was introduced to delay the laser pulse exciting the magnetic system with respect to the synchrotron pulse probing the system's response, once a synchronization between both light sources was established.

In the single bunch operation mode, where the pulse structure of the synchrotron is reduced to a single electron bunch circling the ring at a frequency of 1.25 MHz, it is possible to employ a lock-in technique to measure small changes of the reflectivity

with a high signal-to-noise ratio of $10^{-4} - 10^{-5}$. In contrast to static measurements with a slowly responding photodiode, the temporal evolution of the reflectivity as a function of the pump-probe delay has been detected by means of a bias tee (Picosecond - 5530B), and an avalanche photodiode (APD) with a response time of about 10 ns (Hamamatsu - S5345). The resulting pulse was electronically amplified by a current amplifier (Femto - DHP-100) and stretched in time by custom made electronics (see appendix) to satisfy the required sampling ratio of approximately 1:10 for the 2 MHz digital lock-in amplifier (Signal Recovery - 7280DSP). The amplified signal was smoothed by a low-pass filter (Micro Circuits - BLP-21.4+) having a cut-off frequency of 20 MHz before it was fed into the lock-in amplifier locked to the 1.25 MHz reference signal derived from the synchrotron bunch clock. Again, changing the photon energy, driving the magnetic field, moving the delay stage, reading out the lock-in amplifier and saving the data has been accomplished by a simple laptop via a LabView program and a GPIB interface.

3.4 MOKE Experiments in the Optical Laboratory

Static as well as time resolved MOKE setups served as reference experiments to characterize all magnetic samples in the visible range. As most of the studied samples are in-plane magnetized, a longitudinal MOKE geometry is used to measure the magnetic switching behavior in the scattering plane. Schematics of the employed setup are displayed in figure 3.8.

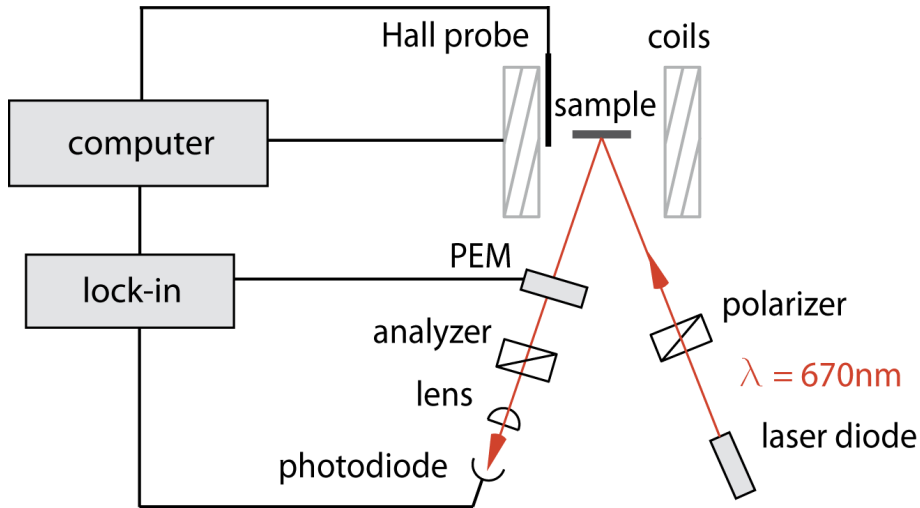


Figure 3.8: Schematics of the longitudinal MOKE experiment.

A monochromatic beam with a wavelength of 670 nm from a laser diode (Toshiba - TOLD 9321M) is directed at the sample at an incidence angle of about 15° . Before hitting the sample, the beam is p-polarized by a Glan-Taylor polarizer. After the light is reflected off the sample and before it passes through an analyzer, it is modulated at a frequency of 50 kHz by a photoelastic modulator (Hinds - PEM-90). Behind the analyzer the light is focused by a lens onto a custom made photodiode, which is connected to a lock-in amplifier (Signal Recovery - 7265) locked to the 50 kHz of the PEM. It can be shown that the measured amplitude of this frequency component is linearly proportional to the Kerr ellipticity ϵ_K [79] and thus to the sample magnetization in first approximation. By introducing a $\lambda/4$ retardation plate between the sample and the PEM, it is possible to measure the Kerr rotation Θ_K instead of the ellipticity ϵ_K , thereby accessing the complex Kerr angle Φ_K . The sample can be mounted on a manually rotatable holder allowing for the experimental determination of the magneto-crystalline in-plane anisotropy, for example. Moreover, two motorized linear translation stages (Newport - 850G) can move the sample holder with an accuracy of about $1 \mu\text{m}$ in the plane of the sample surface (x-y plane - compare figure 2.1 b), thereby facilitating a MOKE study of samples with laterally varying magnetic properties. A magnetic field of up to 700 mT can be applied in the plane of incidence, the field intensity of which is measured by a calibrated Hall probe (Magnet-Physik - FH36). All electronic devices are controlled, synchronized and read out via their RS232 or GPIB interfaces in a LabView environment.

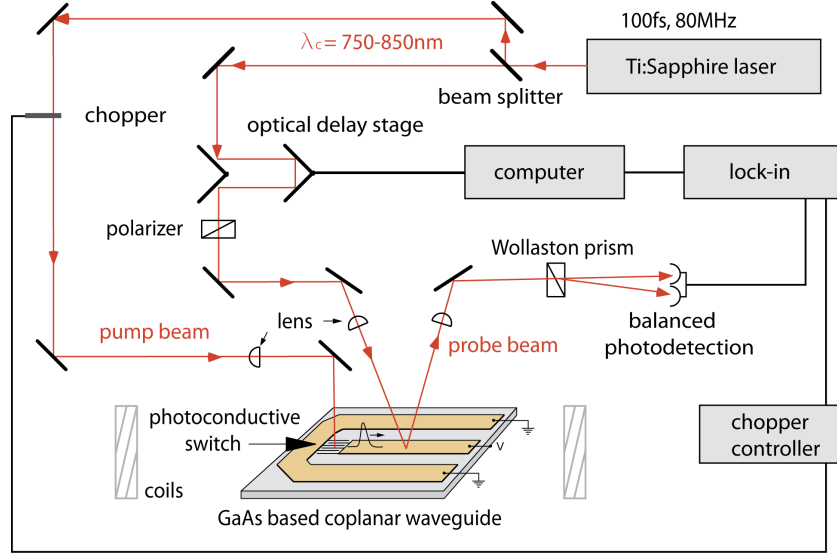


Figure 3.9: Schematics of the time-resolved MOKE experiment.

A schematic of the time-resolved MOKE setup can be seen in the figure 3.9. A Ti:Sapphire based oscillator (Spectra Physics - MaiTai) is used to deliver laser pulses at a repetition rate of 80 MHz over a tunable wavelength range from 750 nm to 850 nm with a pulse length of about 100 fs and a pulse energy of approximately 10 nJ. The emitted light is divided by a beam splitter in two beams of equal intensity. The reflected portion is directly guided and focused onto the sample by a plano-convex lens with a focal length of 15 cm, exciting the magnetic system at normal incidence. The portion transmitted through the beamsplitter is diverted over a linear translation stage (Newport - IMS600PP) before it is focused onto the sample by a plano-convex lens with a focal length of 10 cm, probing the system's magneto-optical response under oblique incidence angles. At this geometry a change in the magnetization of the sample induces a change in the polarization state of the reflected light, which is detected by a Wollaston prism in combination with a balanced photo detection scheme (see appendix). Variable grey wheels, rotatable polarizers and $\lambda/2$ retardation plates are placed into both beams to define the intensity as well as the polarization impinging onto the sample and maximize the magneto-optical response. In order to be able to detect small changes of the polarization, a mechanical chopper (Thorlabs - MC2000) is introduced into the pump beam to modulate the excitation of the magnetic system at a frequency of a few hundred Hz. A reference signal derived from the chopper is fed into a lock-in amplifier (Stanford Research Systems - SR810) receiving the amplified signal from the biased and balanced photodiodes. By moving the translation stage, thereby opto-mechanically delaying the probe pulse with respect to the pump pulse, and reading out the lock-in amplifier as a function of the delay, it is possible to measure the temporal evolution of the magnetization change induced by the pump beam. It has been shown that at this wavelength and geometry, the probe beam is sensitive to the polar component of the magnetization [80]. A bipolar power supply (Kepco - BOP 20/20) drives the current through a pair of magnetic coils providing a field of up to 150 mT in the plane of incidence at 6 A. A standard LabView programmed PC is used to communicate with all devices by means of their respective interfaces.

In contrast to the pump-probe experiment at the synchrotron where the synchronization of the pump and probe beam is accomplished by electronic and mechanical means, this pure optical technique possesses an inherent jitter-free synchronization as only a single light source is involved and a firm phase relation between the pump and probe pulses is maintained throughout the experiment.

3.5 Soft X-Rays from Higher Harmonic Generation

Even though a laser pump and a soft x-ray probe experiment at the storage ring extends the optical approach by gaining element-selectivity and a higher magnetic contrast, the pulse length of the synchrotron generated radiation in the picosecond range limits investigations of ultrafast magnetization dynamics. Only if appropriate techniques, such as femto-slicing [31], or suitable light sources, such as free electron lasers [32], are employed, processes on the femtosecond timescale associated with the fundamental nature of magnetism can be studied. However, not only is the access to this kind of capabilities extremely limited, but also issues related to the photon flux and the pulse-to-pulse stability are a major concern. That is why a table-top and laser-based light source producing ultrafast as well as coherent soft x-ray pulses [38] represents a viable alternative for exploring magnetism at its fundamental limits in space and time.

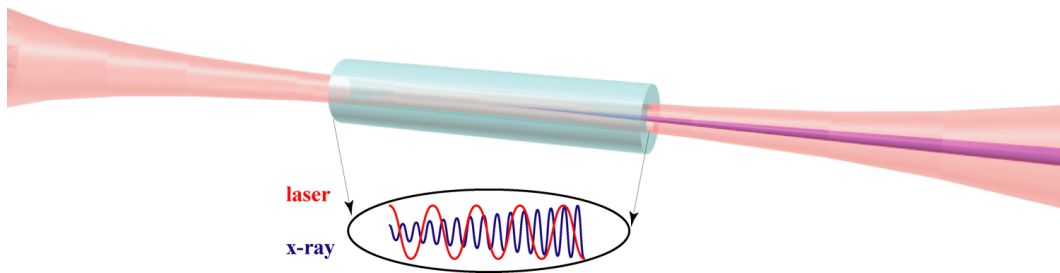


Figure 3.10: Illustration of the principle behind the employed table-top soft x-ray source. An intense laser pulse is focused into a gas filled capillary, producing a co-propagating beam of higher harmonics - adopted from [38].

The figure above illustrates the underlying principle behind the employed table-top source. Similar to the basic three components that are required to build a laser, there is a pump - here an intense laser pulse -, a conversion medium that is being pumped - in this case a noble gas - and to some limited extent a resonator or in the case of soft x-ray radiation a waveguide - here a glass capillary in which the gas flows, the laser beam is focused into and the generated x-rays are guided through.

The process in which laser light is upconverted to integer multiples of its fundamental frequency by a highly nonlinear interaction in a conversion medium is commonly referred to as higher harmonic generation (HHG). Figure 3.11 schematically depicts the conversion process and illustrates how it can be described in the so-called three step model [81, 82]. In this semi-classical picture, electrons are first ripped from their parent atoms in a tunneling process, which is induced by the strong electrical field

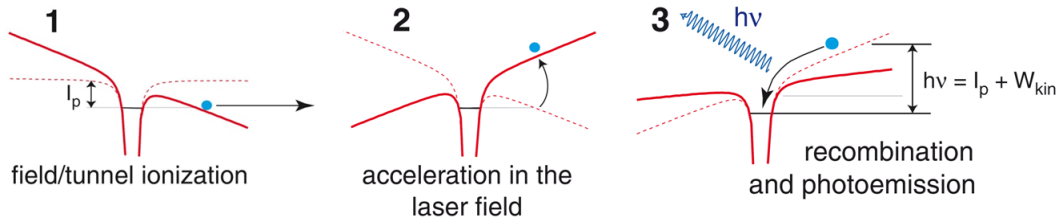


Figure 3.11: Higher Harmonic Generation in the three step model - adopted from [75].

of the laser pulse distorting the Coulomb potential of the atom. In the second step, the electrons are accelerated in the laser field gaining a significant amount of kinetic energy. Finally they recombine with their parent atom in a fraction of a femtosecond under the emission of a photon in the soft x-ray range. As this process repeats itself every half-cycle of the laser pulse and the field direction reverses, thereby introducing a phase shift every time the electron recombines, it can be easily shown, that the spectrum of the produced radiation has to consist of peaks at odd integer multiples of the laser frequency.

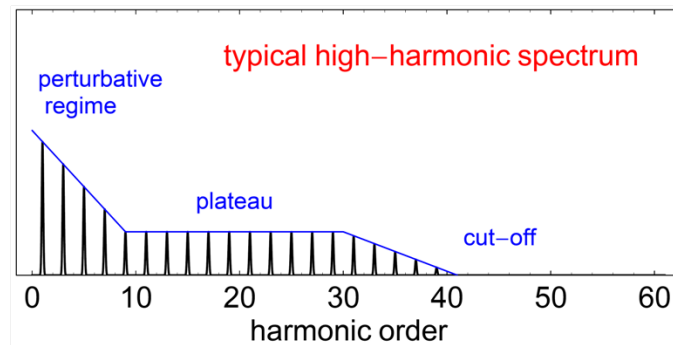


Figure 3.12: Scheme of a typical HHG spectrum - adopted from [83].

Because each half-cycle of the driving laser pulse gives rise to a short burst of x-rays and the amplitude of the electric field for each of these cycles varies due to the usually Gaussian structure of the pulse, the energy of the photons generated at the respective cycles differs. Thus, the total sum of all generated bursts from a single optical laser pulse results in a broad spectrum of harmonics. A scheme of a typical HHG spectrum can be seen in figure 3.12 and it can be divided into three parts. In the perturbative regime photons are generated for electrical field strengths that are

still small in comparison to the inner atomic Coulomb field. Therefore, their behavior can be described by the well-known expansion of the electric polarization, leading to nonlinear effects, such as third harmonic generation (THG). When the electrical field strength of the laser pulse increases, a plateau of harmonics and the final cut-off can be observed. Intuitively, the highest energy is determined by the maximum of the kinetic energy obtained in the laser field and the ionization potential of the conversion medium I_p . Assuming that the electrons are accelerated in the sinusoidal electric field $E = E_0 \sin \omega t$ of the laser, having an intensity I and a central wavelength λ , the gained average energy is given by the ponderomotive potential U_p [84]:

$$U_p[\text{eV}] = \frac{e^2 E_0^2}{4m_e \omega^2} = 0.97 \cdot 10^{-13} I [\text{W cm}^{-2}] \lambda^2 [\mu\text{m}^2]. \quad (3.3)$$

Both the tunneling and the recombination process are subject to a certain probability, which consequently means that only electrons that leave the atom at a specific phase of the electric field and adhere to distinct trajectories contribute to the resulting photon field. Considering this fact, an accurate determination of the highest photon energy in the semi-classical three step model can be given [81, 82]:

$$\hbar\omega_{max} = I_p + 3.2U_p. \quad (3.4)$$

This so-called cut-off law suggests that a conversion medium with a high ionization energy, such as a noble gas, and a laser with a high intensity have to be chosen, if high photon energies are desired. Practically meaning, that by focusing a laser pulse with a pulse energy of 1 mJ and a pulse length of 100 fs with a 30 cm lens into a Neon-filled capillary could yield photons up to an energy of 74 eV. This is high enough to address the M absorption edges of most 3d transition metals with moderate effort resulting in a strong magnetic contrast and element-selectivity.

Similar to second harmonic generation in non-linear crystals; however, a sophisticated dispersion management is required to maximize the x-ray photon output. The laser light as well as the produced comb of harmonics have to travel through the wave guide at the same velocity with their phases matched in order to ensure an optimum of constructive interference of the produced radiation [85]. In the case of a hollow waveguide filled with a conversion medium, there are three major contributions to the wavevector mismatch Δk , which is assumed to be a scalar due to the co-propagation of the m^{th} harmonic and the fundamental wave oscillating at a frequency ω_f .

First, there is a frequency-dependent mismatch of the refractive indexes n in the conversion medium, whose normal dispersion relation is assumed to be linear in ω . Since generally the refractive index in the optical or near infrared region is larger than 1 and in the EUV region smaller than 1, the respective wavevector mismatch Δk_{disp} is positive. Second, as the electrical field of the laser is high enough to ionize the medium and most of the electrons do not recombine with their parent atom, a plasma is formed

which itself causes a change of the refractive index. The induced mismatch Δk_{plasma} can be related to the resonance frequency of the plasma ω_P and it is negative. It is important to note that if a critical plasma density is reached, the plasma becomes completely absorbing for the generated electromagnetic wave, which ultimately limits the phase-matching of multi-cycle pulses. Third, the laser beam is guided through a waveguide with an inner radius a , which only admits distinct modes propagating inside of it. Each of these eigenmodes exhibits a particular dispersion resulting in a negative mismatch of Δk_{cap} , which can be related to the l^{th} zero of the Bessel function $J_{n-1}(u_{nl}) = 0$. Thus, the total mismatch of the wavevector can be written as [75]:

$$\begin{aligned} \Delta k &= \underbrace{\Delta k_{disp}}_{> 0} + \underbrace{\Delta k_{plasma}}_{< 0} + \underbrace{\Delta k_{cap}}_{< 0} \\ &= \underbrace{(n(\omega_f) - n(m\omega_f)) \frac{\omega_f}{c}}_{> 0} + \underbrace{\frac{\omega_p^2(1 - m^2)}{2mc\omega_f}}_{< 0} + \underbrace{\frac{u_{nl}^2(1 - m^2)}{2ma^2\omega_f}}_{< 0}. \end{aligned} \quad (3.5)$$

As can be seen easily from the equations above, the contributions of the plasma and the waveguide are both negative in sign and therefore have to be compensated for by the normal dispersion of the refractive index. In the experiment, this is most conveniently achieved by varying the pressure and thereby the density of the gas flowing through the capillary for a given pulse length and intensity; two parameters which already determine the desired cut-off frequency.

In summary, if perfect phase matching is achieved in the capillary, the driving laser pulse propagates through the wave guide and continuously generates new harmonic light that constructively interferes with the co-propagating harmonic radiation generated earlier. This superposition guarantees that the generated soft x-rays retain the polarization as well as coherence properties of the driving laser pulse, to which they are inherently synchronized. The resulting radiation has not only a good beam profile and a small divergence, but also full spatial coherence which opens the door for coherent imaging of magnetic structures, as has already been demonstrated with a resolution below 50 nm in the non-magnetic case [42]. Since the recombination process of the electron with the parent atom happens within a sub-cycle of the driving laser pulse, ultrashort pulses down to the attosecond regime can be generated [86], allowing for pump-probe experiments with a superb temporal resolution.

A comparison of the brilliance between a HHG source and the synchrotron, which can be extracted from figure 3.13, boils down to a discussion of the pulse length and repetition rate.

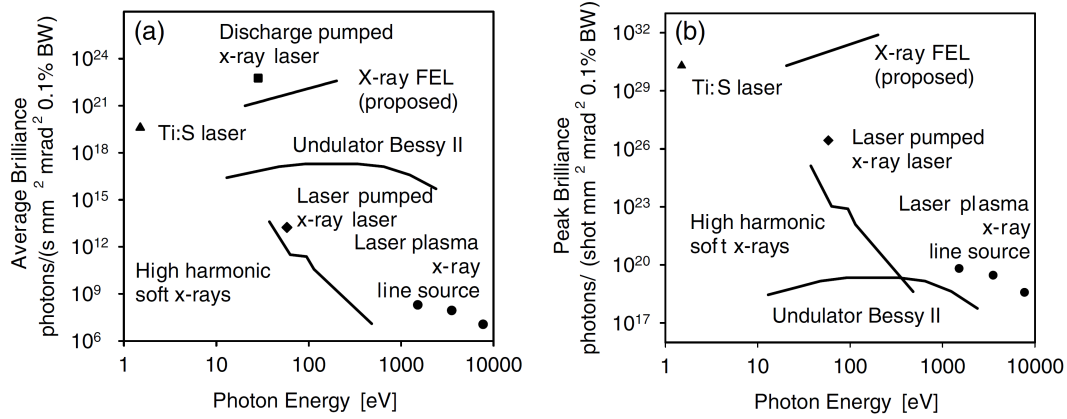


Figure 3.13: Average (a) and peak (b) brilliance of various light sources - from [75].

Although the average brilliance of an undulator from BESSY is more than three orders of magnitude higher than from a HHG source, the brilliance per shot of the latter is superior to the peak brilliance of the former light source. This fact can be easily understood by considering that the high average photon flux from an undulator originates from a repetition rate in the MHz and pulse lengths in the picosecond range as compared to high-harmonic sources, where repetition rates are on the order of kHz and pulse durations on the femtosecond to attosecond time-scale.

3.6 Time-Resolved Experiments employing a HHG Source

An illustration of the experimental HHG based pump probe setup used for this study can be seen in figure 3.14. Ultra short (30 fs) and intense laser pulses (2.2 mJ) from a Ti:Sapphire based multi-pass amplifier (KMLabs - prototype) are divided by a beam splitter with a ratio of 90:10 into two beams. The weaker portion of the split light intensity is diverted over a linear translation stage (Newport - UTS100CC) before it illuminates the sample in order to excite the magnetic system. The remaining ninety percent of the beam intensity is focused into a neon filled capillary by a plano-convex lens with a focal length of 50 cm, thereby producing a frequency-comb of ultra-short coherent EUV pulses. Behind the capillary a 200 nm thick Al filter blocks out the co-propagating laser light and passes harmonics up to an energy of 73 eV with an average transmissivity of about 70 % [71]. At an incidence angle of 8°, a toroid mirror directs these EUV pulses onto the sample probing the system's response close to an angle of about 45°. Subsequently, the probe light is focused on a x-ray CCD camera (Andor - Ikon L). Both the pump and residual visible light are blocked out thereafter by two additional Al filter of 200 nm thickness positioned right in front of the camera. In

order to maximize the reflected portion of the HHG photons, a grating like structure has been manufactured to act as both the sample and a dispersive element separating the harmonics on the CCD chip. Helmholtz coils sandwiching the sample generate a homogeneous magnetic field with a strength of up to 10 mT, if driven by a current of 10 A provided by a bipolar power supply (Kepco - BOP 10/10). The sample holder and the coils are equipped with a water cooling stabilizing the temperature of the sample for a running experiment around 12°C, which is measured by a thermocouple directly connected to the sample holder. The data acquisition, the application of the magnetic field and the positioning of the delay stage is realized by custom made electronics and LabView programmed device interfaces.

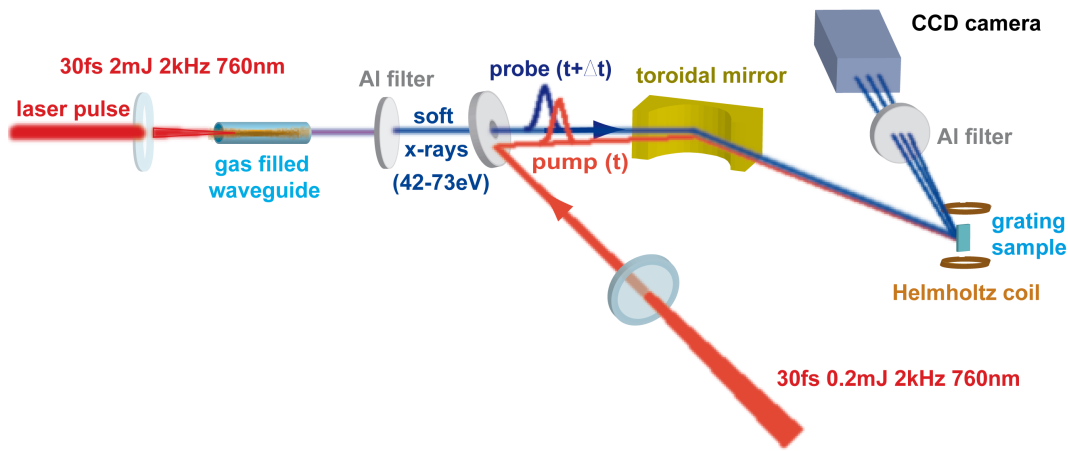


Figure 3.14: Schematics of a NIR pump and EUV probe experiment based on HHG [41].

3.7 Construction of a HHG Beamline

Even though all experiments shown in this thesis involving a table-top soft x-ray source have been carried out in collaboration with the group of Prof. Margaret Murnane and Prof. Henry Kapteyn at the University of Colorado in Boulder, a HHG soft x-ray beamline has been constructed at the Forschungszentrum Jülich in the group of Prof. Claus M. Schneider based on the pump-probe experiment mentioned above. The experience gathered at JILA in Boulder helped to identify weaknesses in the initial design not only improving the capabilities of the newly constructed beamline (see figure 3.15) in terms of photon flux, stability and handling, but also facilitating to choose among various companies and parameters to obtain the most essential piece of equipment, the laser amplifier system.

First of all, a large laser hatch based on aluminum profiles has been installed around a vibration-isolated optical table, providing a clean room like environment for the beamline as well as the laser system. As the temperature can be stabilized within 0.1°C and most contaminants can be kept from entering the hatch, the maintenance of the laser amplifier is supposed to be minimized and the stability of the entire experiment should be significantly improved. An advanced version of the amplifier, the experiments were conducted with in Boulder, was obtained from the company KM-Labs. This recently installed laser system has shown to deliver 2.4 mJ per pulse with a pulse length of 25 fs at a repetition rate of 2 kHz. In spite of similar specifications, the laser in Jülich has some advantages over the prototype of the Dragon at JILA, such as a helium cryostat instead of a nitrogen dewar for cooling the Ti:Sapphire crystal, a more reliable pockels cell whose pulse-picking gate does not drift in time and in general more robust optical components.

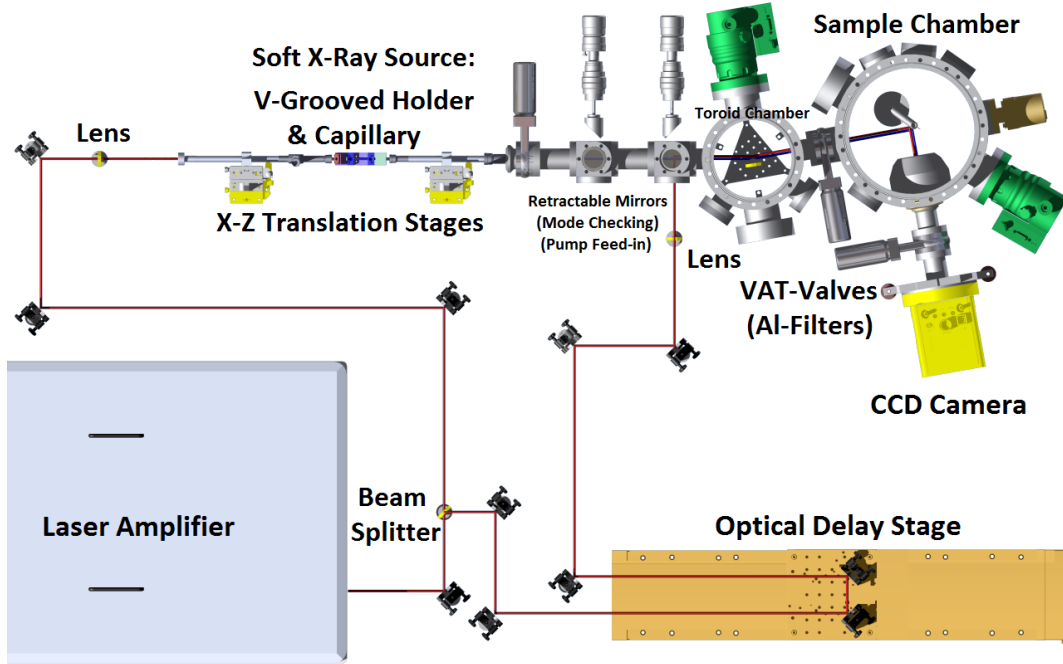


Figure 3.15: HHG based soft x-ray beamline at the Forschungszentrum Juelich.

In addition to the laser system, a soft x-ray source was delivered consisting of all necessary components to generate higher harmonics. One end of the HHG beamline, assembled from these components, is terminated by a sapphire window to admit laser light and the other is connected to the experiment delivering the higher harmonics.

The package contained a plano-convex lens with a focal length of 50 cm coming with an anti-reflective coating for the visible and near infra red spectral range. This lens is used to focus the amplified laser beam into the capillary and it can be mounted on a provided linear translation stage. That is how the focus can be moved with respect to the capillary in order to optimize the intensity as well as mode coupled into the waveguide. The capillary itself is placed into a v-grooved holder [87], which can be connected on both ends to stainless steel tubes. Each of these steel pipes is mounted to high precision x-z translation stages, which allow for an accurate alignment of the capillary with respect to the laser beam and focus in order to maximize the coupling efficiency. The steel pipes connected to the capillary holder are evacuated via individual outlets connected to a rough vacuum pump, whereas the v-grooved holder possesses two additional gas inlets located right above the laser-drilled holes of the capillary to admit a gaseous HHG conversion medium. A mass flow meter (Cole Palmer - PC3) is used to precisely adjust the amount of gas flowing through the capillary to phase-match the generating and generated electromagnetic waves.

This source of higher harmonics is connected to the toroid chamber by two CF40 cubes, each of which is equipped with a rotational linear feed-through on one side and a CF40 window on the opposite side. At the tip of both feed-throughs a silver mirror is mounted at an angle of 45° . This construction allows for moving and completely retracting the mirrors into and from the beam path. The first mirror is used for alignment purposes of the capillary. When laser light is initially coupled into the wave guide at low intensities, this mirror serves to reflect the visible light through the window out of the beamline. Thus, the transmitted intensity and mode of the laser light through the capillary can be optimized by means of the above-mentioned translation stages without having to break the vacuum. The second mirror, on the other hand, is moved into the beam during the pump-probe experiment transmitting the soft x-rays by a 3 mm wide hole centrally drilled into the mirror under an angle of 45° . That is how laser pump pulses can be coupled into the experiment almost co-propagating with the HHG probe pulses, thereby minimizing the angular smear of the pump-probe overlap.

In the initial design of this pump-probe experiment in Boulder, the toroid mirror as well as the sample holder including the Helmholtz coils were squeezed into a single UHV chamber. In contrast to this, separate chambers for the sample and the toroid were constructed for the Jülich beamline (see appendix for detailed drawings). The toroid chamber is based on a CF150 steel UHV extension tube. Standard CF40 flanges were attached in the scattering plane at various positions to ensure a certain flexibility for the reflection geometry. Two CF60 ports were welded to this construction to admit a turbo pump (Pfeifer - HiPace60) thereby maximizing the pumping cross section. In contrast to this chamber which accommodates only a relatively small part that is not touched once properly aligned, the sample chamber is constructed on the basis of a CF250 tube, in which the sample holder and water-cooled coils have to be placed.

Similarly, CF40 and CF60 flanges have been attached to this body in the plane of incidence admitting the essential periphery, such as a turbo pump, water cooling, mechanical and electrical feed-throughs. Moreover, a custom designed flange has been welded into this reflectometer, which allows for the camera to be moved in a range of $\pm 10^\circ$ around an right angle reflection geometry. As can be seen in figure 3.15, UHV CF40 gate valves not only connect all individual parts of the setup, but also can they be equipped with a metallic filter, such Al, to block out a certain spectral portion of the passing light once the valve is closed.

Due to the changed dimensions of the setup, the imaging properties of the toroid mirror had to be adjusted accordingly. To this end, the optical characteristics of the involved components and the entire experiment were simulated by the raytracing program RAY [88]. This freely available software is provided by BESSY and it is a powerful tool to simulate the geometric optical response ranging from individual components and light sources, such as spherical gratings and undulators, to sophisticated synchrotron beamlines.

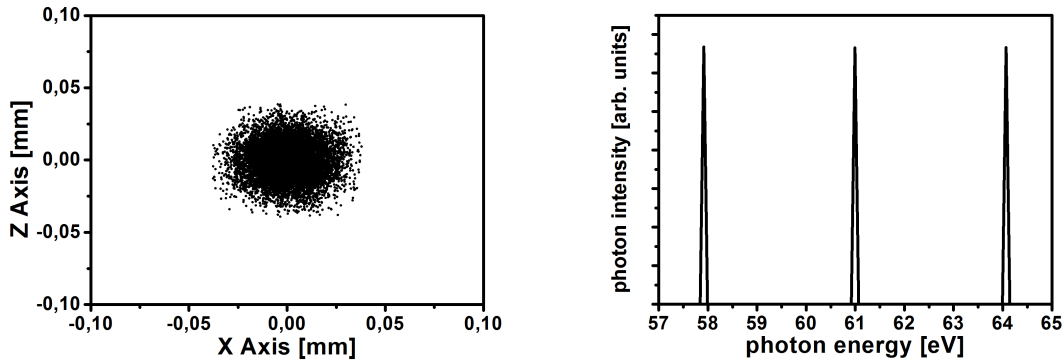


Figure 3.16: RAYtracing simulation of a HHG $25\ \mu\text{m}$ wide (FWHM) point source (left) emitting three δ -function-like harmonics (right) with a divergence of 2 mrad.

To start with, the generated harmonics are considered to originate from a point source with a diameter of $25\ \mu\text{m}$ (FWHM) and they subsequently propagate in a laser like manner with a divergence of 2 mrad; realistic parameters that have been determined in previous experiments [87]. Figure 3.16 shows the simulated intensity profile at the origin of this source on the left side. The right side of the same figure depicts the assumed emission spectrum consisting of three harmonics which are 3.2 eV apart and centered around the 61 eV, the approximate position of the Co absorption edge in the EUV. It is further assumed that a toroid is placed at a distance of 750 mm from the point source, the sample is located about 300 mm further down the beam path and the camera chip will be positioned 450 mm thereafter.

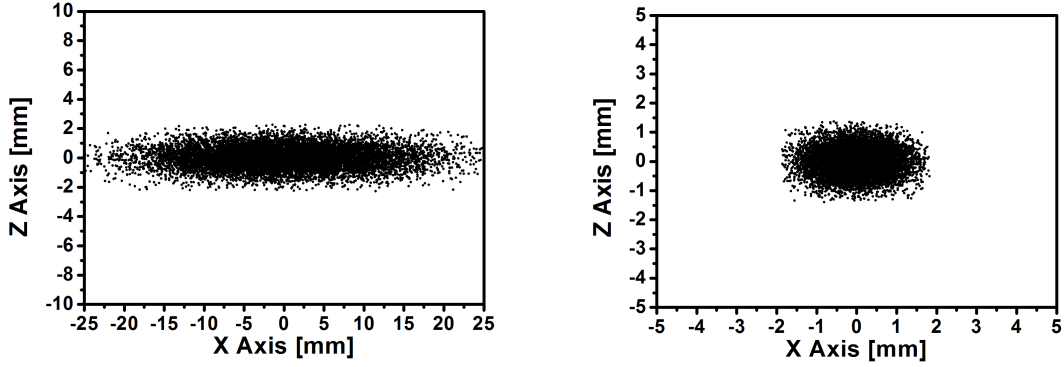


Figure 3.17: RAYtracing simulations: Intensity footprint of the toroid (left) at an incidence angle of 5° located 750 mm away from the HHG point source and intensity footprint of the sample/grating (right) at an incidence angle of 45° located 300 mm away from the toroid.

The incidence angle of the toroidal mirror has been chosen such that the reflectivity of the toroid is maximized and the alignment at flat incidence angles can still be performed comfortably. The raytracing revealed that at an angle of 5° the reflectivity of a gold coated toroid amounts to 81% (75%) for s(p)-polarized light, whereas the reflected intensity at the toroid surface is reasonably spread over approximately 40 mm of the horizontal axis (compare figure 3.17 - left). Thus, the dimensions of the toroid substrate and their respective curvatures were determined to be 8605 mm over the 50 mm long horizontal axis and 65.4 mm over the 25 mm short vertical axis. With this kind of toroid, the EUV spot size at the sample surface positioned 300 mm further down the beam path was simulated to be as large as 1 mm (FWHM) along the vertical axis. In order to maximize the magnetic contrast in a T-MOKE geometry, the grating-like sample is supposed to be rotated by 45° around its vertical z-axis approaching the Brewster angle. This explains the spread of the spot size by a factor of $\sqrt{2}$ along the horizontal x-axis as compared to the z-axis in figure 3.17 - right.

In order to characterize only the imaging properties of the setup, the sample was chosen to be a laminar non-magnetic gold grating with a line density of 500 lines/mm and a groove depth of 30 nm. Figure 3.18 depicts the simulated intensity footprint at the CCD chip, which is assumed to be positioned about 450 mm behind the sample in the image plane of the toroid. Both the specular reflection in 0th order at the center of this figure and the ± 1 st diffraction orders of the three harmonics around ± 7 cm on the x-axis can be clearly identified. The simulation reveals that the $25 \mu\text{m}$ wide point source can be imagined in this geometry on Gaussian points with a diameter of $60 \mu\text{m}$ at FWHM. For the sake of illustration; however, the imaged harmonics appear to be elongated along the vertical axis because of the large difference in scale.

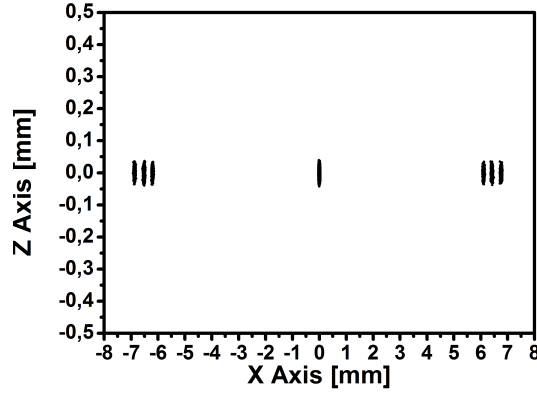


Figure 3.18: RAYtracing simulation: Intensity footprint in the image plane, where the CCD chip is supposed to be positioned - 450 mm behind the sample.

As the CCD chip consists of 2048 by 2048 pixels, each of which is as small as $13 \times 13 \mu\text{m}^2$, the entire spectrum can be comfortably recorded at this configuration in a single shot. Furthermore, a first estimate of the transmitted intensity can be given. For an s(p)-polarized beam the intensity of the 0th order is calculated to be 4.2% (0.25%), whereas for the +1st order only 0.38% (0.025%) and -1st order 0.28% (0.016%). Now, if the material of the grating is changed from gold to a magnetic system, a further drop of the transmitted intensity is to be expected, especially so, as the T-MOKE experiment is tuned to the *M absorption* edge of the material under investigation. Nonetheless, it is the large magnetic dichroism of up to 100% and the high sensitivity of the employed X-ray CCD camera, proven to recover even small changes of the sample magnetization, which more than justifies the practicability of this pump-probe experiment.

Chapter 4

Static Synchrotron Experiments

This chapter deals with results obtained in static reflectivity experiments at the synchrotron. The following pages aim at examining the potential of resonantly scattered light in a T-MOKE geometry to provide an element-selective magnetic contrast mechanism in the EUV. Two types of experiments have been conducted to this end, both of which focus on coupled magnetic multilayer systems comprising iron, cobalt and nickel. By tuning the photon energy to the M absorption edges of the element under investigation, either study addresses the question of whether the switching behavior of individual layers can be distinguished in a multilayer.

In the first experiment spatially separated but homogeneous and ferromagnetically coupled layers in a wedged $\text{Co}(5\text{ nm})/\text{Si}(1\text{--}4\text{ nm})/\text{Ni}(8\text{ nm})/\text{Fe}(2\text{ nm})$ multilayer are studied. Measurements and supporting simulations of the magneto-optical response as a function of the photon energy, the incidence angle and the Si spacer thickness explore the character of the magneto-dichroic signal in the EUV and its potential for layer-selective investigations. In this system a magnetic contrast as high as 80 % can be obtained and the recorded magneto-optical loops of the hysteresis prove that the switching of single layers can indeed be measured layer-selectively.

The second experiment is concerned with magneto-optical investigations of a single multilayer containing two anti-ferromagnetically coupled heterogeneous ferromagnetic layers. Here, the magneto-optical response of the system consisting of a bottom $\text{Co}_{40}\text{Fe}_{60}$ layer (10 nm) and a top $\text{Ni}_{80}\text{Fe}_{20}$ layer (5 nm) separated by a thin layer of Cr (0.6 nm) is compared with the response of the respective individual alloys. The hysteretic switching behavior of the multilayer is analyzed in the EUV with regard to layer-selectivity by referring to the absolute magnetic moment derived from measurements by a SQUID magnetometer. The magnetic contrast reaches about 30 % and the individual switching of layers in the multilayer can be observed.

Both experiments show that the magnetic contrast at the M absorption edges is much larger than in the visible or soft x-ray range. However, due to the energetic proximity of the absorption edges of Fe, Co and Ni special care has to be taken to attain a layer-selective response from a complex multilayer system.

4.1 A Ferromagnetically Coupled Multilayer

In an effort to explore the potential of the resonantly enhanced magneto-dichroic signal in the EUV to serve as an element-selective contrast mechanism for magnetic investigations, this study focused at the M absorption edges of the two neighboring 3d ferromagnets cobalt and nickel. These elements were chosen because of their known absorptions edges located around 60 eV and 66 eV [33], respectively - at photon energies which are still within reach of the Jülich undulator beamline UE 56/1-SGM at BESSY. In addition, their energetic proximity immediately raised the question of whether the response of a magnetic system containing Co and Ni can be probed element-selectively in the same manner as at the L absorption edges [89]. To this end, thin cobalt and nickel films spatially separated by a silicon spacer with varying thicknesses were fabricated in a wedged multilayer system and characterized by means of MOKE in the visible as well as extreme ultraviolet range.

4.1.1 Sample Preparation and Characterization

The sample consisted of a magnetic trilayer structure and was prepared by thermal evaporation at a base pressure of 5×10^{-11} mbar [90]. In a first step a substrate system for the magnetic multilayer was manufactured comprising a 150 nm thick Ag $\langle 001 \rangle$ buffer layer [91], which was grown on an iron precovered GaAs $\langle 001 \rangle$ wafer at a temperature of 380 K. After annealing at a temperature of 570 K, a 2 nm Fe layer followed by a 8 nm Ni layer were deposited onto the buffer at room temperature. A stepped Si layer with a step height of 1.5 nm, 2.5 nm and 4 nm, each 1 mm wide, followed. Finally, a 5 nm thick Co layer was deposited on top.

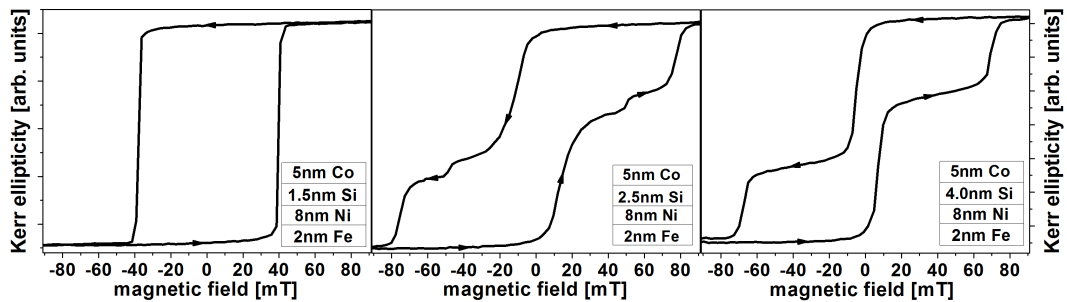


Figure 4.1: Magneto-optical loops of the multilayer wedge system taken at a Si spacer thickness of 1.5 nm (left), 2.5 nm (middle) and 4 nm (right) by means of a longitudinal MOKE setup (compare section 3.4).

The magnetic switching behavior in the plane of the multilayer system was first characterized by MOKE measurements in the visible range. Recording hysteresis loops in a L-MOKE setup (see section 3.4) for various angles of the sample with respect to the external magnetic field revealed a negligible magneto-crystalline anisotropy. Three regions of different interlayer coupling between the Co and Ni/Fe layers were identified and associated with regions of different Si spacer thicknesses, as deduced from distinct coercivities of the hysteresis loops, which are displayed in figure 4.1.

As can be seen in this figure, at a spacer thickness of 1.5 nm the multilayer is ferromagnetically coupled forcing all layers to switch simultaneously resulting in a rectangular magneto-optical hysteresis loop. At a spacer thickness of 4 nm the multilayer is entirely decoupled allowing for an independent switching of the top Co and bottom Ni/Fe layers, which is indicated by the stepped hysteresis loop. Independent experiments prove that the Ni/Fe bilayer indeed behaves like a single magnetic unit. At a spacer thickness of 2.5 nm an intermediate behavior can be observed, in which the reversal of one layer is hindered by a weak ferromagnetic interlayer coupling. The hysteresis loops taken in the visible range do not reveal directly, which layer switches first, thereby necessitating a layer- and element-selective approach.

In order to further characterize the magnetic multilayer, resonant magnetic reflectivity measurements were performed in a T-MOKE geometry at the synchrotron. The sample was placed in a reflectometer (see section 3.2) and the reflectivity of linearly p-polarized EUV light was measured across the M absorption edges of Co and Ni from 57 eV to 72 eV with an energy resolution of 0.1 eV and in steps of 0.25 eV. The lower photon energy limit of 57 eV was determined by the smallest possible gap of the undulator forcing the experiment to omit the Fe M absorption edge located around 54 eV. An Al filter was placed on the photodiode to block visible stray light. The Al absorption edge at 72 eV determined the upper photon energy limit of this study.

4.1.2 Magneto-Optical Response in the EUV

As a first step in the experiment, the conditions for a maximum of the magneto-optical signal were determined. For this purpose the magnitude of the dichroism was mapped by taking angular and photon energy scans of the magnetic asymmetry. These measurements were performed for regions of different interlayer coupling clearly identified previously in the visible range. For each of these three regions figure 4.2 depicts the measured asymmetry across the Co and Ni edge in an energy range from 57 eV to 72 eV with the angle of incidence θ varying from 35° to 55° and a magnetic field reversing between ± 100 mT, magnetically saturating the sample in opposite directions.

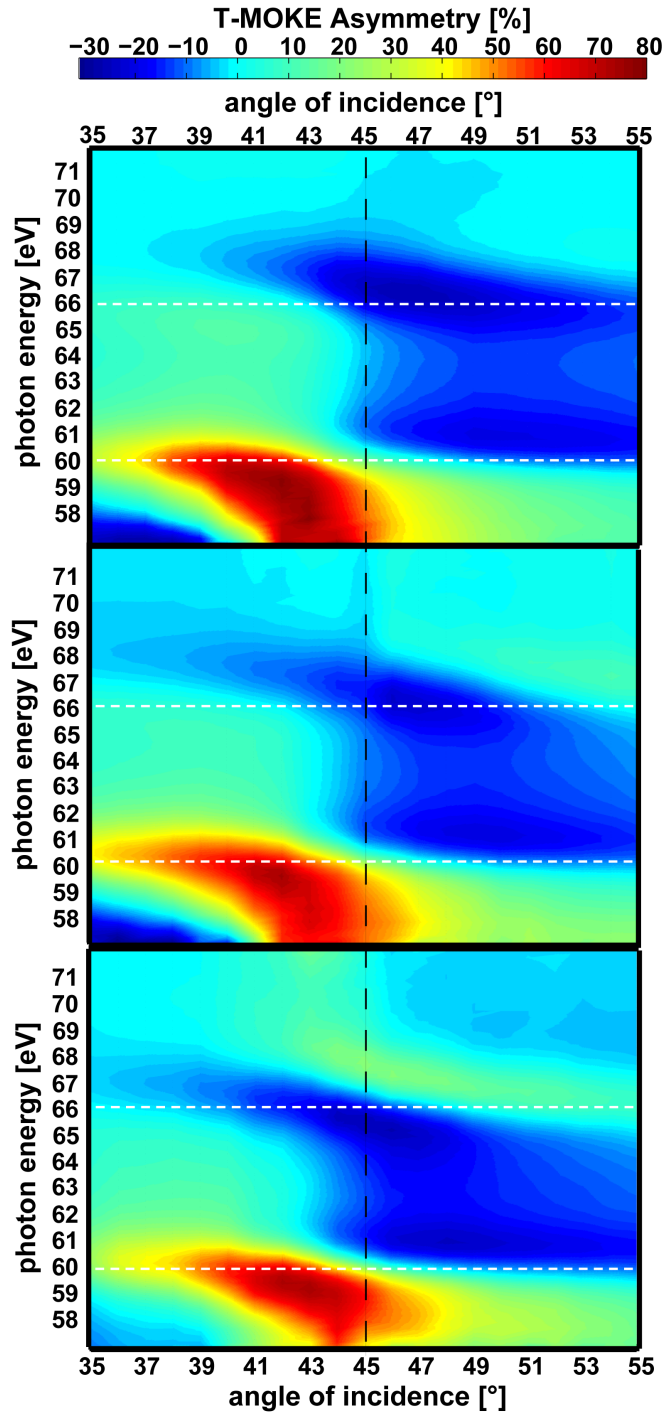


Figure 4.2: Angular and energy dependent magnetic asymmetry of the multilayer wedge system taken at a Si spacer thickness of 1.5 nm (top), 2.5 nm (middle) and 4 nm (bottom). The positions of the atomic absorption edges of Co (60 eV) and Ni (66 eV) are indicated by horizontal white dashed lines.

At first glance, the overall appearance of the asymmetry distributions $A(\theta, h\nu)$ for different Si interlayer thicknesses is quite similar. A closer inspection, however, reveals distinct differences of the magneto-optical signal associated with the absorption edges of Co and Ni. As the main spectral feature, a pronounced bipolar peak structure can be identified in the asymmetry distribution at an energy of 59.5 eV (61 eV) and an angle of 42° (50°) with an amplitude of about 80 % (-25 %) in all three regions of the stepped wedge system. This feature can be clearly attributed to the resonant excitation of the Co layer at the M absorption edge (~ 60 eV) and it is consistent with earlier findings [33]. A totally different behavior of the asymmetry $A(\theta, h\nu)$ can be observed at the M absorption edge of Ni (~ 66 eV). At the lowest Si interlayer thickness (top graph) the magnetic asymmetry has only a dip shape with a negative extremum of about -25 % at an energy of 66.75 eV and an angle of 47°. With increasing spacer thickness the resonance moves towards an energy of 65.5 eV (67.5 eV) and an angle of 45° (46°). At the same time it also changes its shape to a bipolar resonance with an overall amplitude of about ± 20 %.

In an effort to further exemplify and elaborate on this behavior, magnetic asymmetry spectra $A(h\nu)$ have been calculated for all three sample configurations using the formalism outlined in section 2.3. The calculation has been carried out for a fixed angle θ of 45°. This position is marked by a dashed line in figure 4.2, along which corresponding experimental spectra have been extracted. The calculated spectra are compared to the experimental data in figure 4.3.

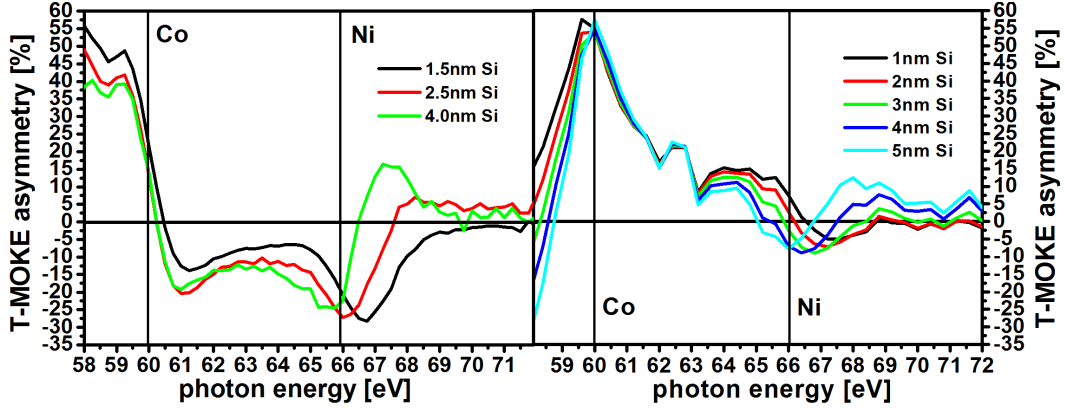


Figure 4.3: Measured (left) and calculated (right) T-MOKE asymmetry spectra of the multilayer for an incidence angle of 45° and various Si spacer thicknesses.

The experimental data for various Si interlayer thicknesses (black, red and green curve) are compiled in the left graph of figure 4.3. From these curves clear differences

can be again discerned for the spectral ranges related to Co and Ni. It is found that the measured asymmetry below 59.5 eV remains at around 45 % for all three regions with a tendency to decrease for increasing Si spacer thicknesses. The curves drop sharply and simultaneously to about -20 % at 61 eV, leveling off with increasing photon energy at approximately -10 %. This magneto-optical response indicates that the Co top layer behaves magnetically and optically similar in all three samples. Clear changes of the asymmetry induced by the spacer thickness are observed in the vicinity of 67 eV, where strong variations of the shape and energy position of the spectral features can be identified. Above 70 eV no significant magnetic signal can be found.

The colored curves in the right graph of the same figure represent the calculated asymmetry spectra for this multilayer system based on optical constants taken from Henke [71] and magneto-optical constants extracted from previously measured rotation spectra [37]. Furthermore, surface and interfacial roughnesses have been neglected in this calculation, since previous simulations have proven them to play a minor role in the response of the multilayer. As the Si interlayer thickness may deviate from the nominal value, the magneto-optical response for several interlayer thicknesses ranging from 1 nm to 5 nm has been calculated.

The simulations indicate a clear trend with respect to the spectral behavior. The Co-related signal is almost independent of the interlayer thickness, whereas the Ni-related features exhibit a clear modulation. With increasing Si interlayer thickness, the Ni signal becomes more pronounced and its features shift towards lower photon energies. In particular, the transition from an unipolar to a bipolar resonance is clearly visible. Most of these trends are qualitatively reproduced by the experimental data in a very reasonable manner. The strong deviation in the energy range of 61 eV to 65 eV can be explained by relatively noisy data of the before-mentioned rotation spectra taken to extract the magneto-optical constants, which are the basis of this simulation - see figure 5 in [37]. Nonetheless, the qualitative agreement between the calculated and the measured magneto-optical response of the multilayer at the Ni edge suggests that the observed shift can be related to interferences of the reflected EUV light at the interfaces of the multilayer stack. A characteristic trend at photon energies below 60 eV can also be noted. With increasing Si thickness the signal drops and even changes sign. This is related to the response of the buried Fe layer, whose response could not be accessed entirely in this study, because of the limited spectral range. However, the trend is somewhat visible in the experimental curves, although the effect is much smaller. This deviation is most likely related to the low photon flux and thus bad signal-to-noise ratio introducing a relatively high uncertainty in the absolute value of the asymmetry below 59 eV. At these photon energies the undulator gap reaches its minimum and it cannot be reliably synchronized with the monochromator any further.

4.1.3 Magnetic Switching Behavior

Having identified maxima of the magnetic contrast at the M absorption edges of Ni and Co, the incidence angle and photon energy can be tuned to probe the magnetic switching behavior element-selectively, which in the case of a multilayer system translates into a layer-specific response. For this purpose, the magnetic field dependence of the magneto-optical signal $A(\mu_0 H)$ was recorded. This measurement results in hysteresis-like loops which do not, however, directly reflect the behavior of the magnetization, as the signal comprises a convolution of magnetic and optical contributions. Therefore, they are called *magneto-optical loops*. The loops, which are displayed in red and green in figure 4.4, have been recorded at a fixed angle of 41° , where local, element-specific maxima of the magnetic contrast are clearly separated, for reasons that are explained further below. The response at the Co edge was taken at a photon energy of 59.5 eV for all three regions (green curves), whereas the response at the Ni edge was recorded at a photon energy of 67.5 eV for a 1.5 nm Si spacer, at a photon energy of 67 eV for a 2.5 nm Si spacer and at a photon energy of 66.5 eV for a 4 nm Si spacer (red curves). These data are compared to the conventional Kerr loops displayed in figure 4.1, which have been inserted as black curves into figure 4.4.

The top graph in figure 4.4 shows magneto-optical loops associated with a sample region having a Si spacer thickness of 1.5 nm. All three loops exhibit a very similar rectangular shape with a coercivity of about 40 mT. The shape of both magneto-optical loops taken at the absorption edges of Co and Ni, reflecting a layer specific response, closely agrees with that of the loop taken in the visible range, which reflects the collective response of the multilayer system. From this result it can be concluded that the entire layer stack undergoes a magnetization reversal as a single magnetic unit. All ferromagnetic layers in the stack are strongly coupled to each other and the coupling across the Si interlayer is of ferromagnetic nature. This ferromagnetic coupling can be a consequence of either intrinsic interlayer exchange coupling, or pinholes or other imperfections in this very thin interlayer, which permit a direct ferromagnetic exchange interaction between the magnetic layers. It remains to be seen whether the coercive field is determined by the magnetic properties of the constituent layers or whether it is directly related to the ferromagnetic interlayer coupling.

The center graph in figure 4.4 displays the data taken from a region of the sample where top and bottom magnetic layers are separated by a Si spacer of 2.5 nm. In the visible range two distinct steps and a third small step at ± 50 mT can be identified in the hysteresis loop. This already points towards a more complex switching behavior, which may be related to a rather individual behavior of the ferromagnetic layers and therefore a weakly coupled state in the multilayer. In the element-selective magneto-optical loops both steps around ± 75 mT agree very well with the coercivity

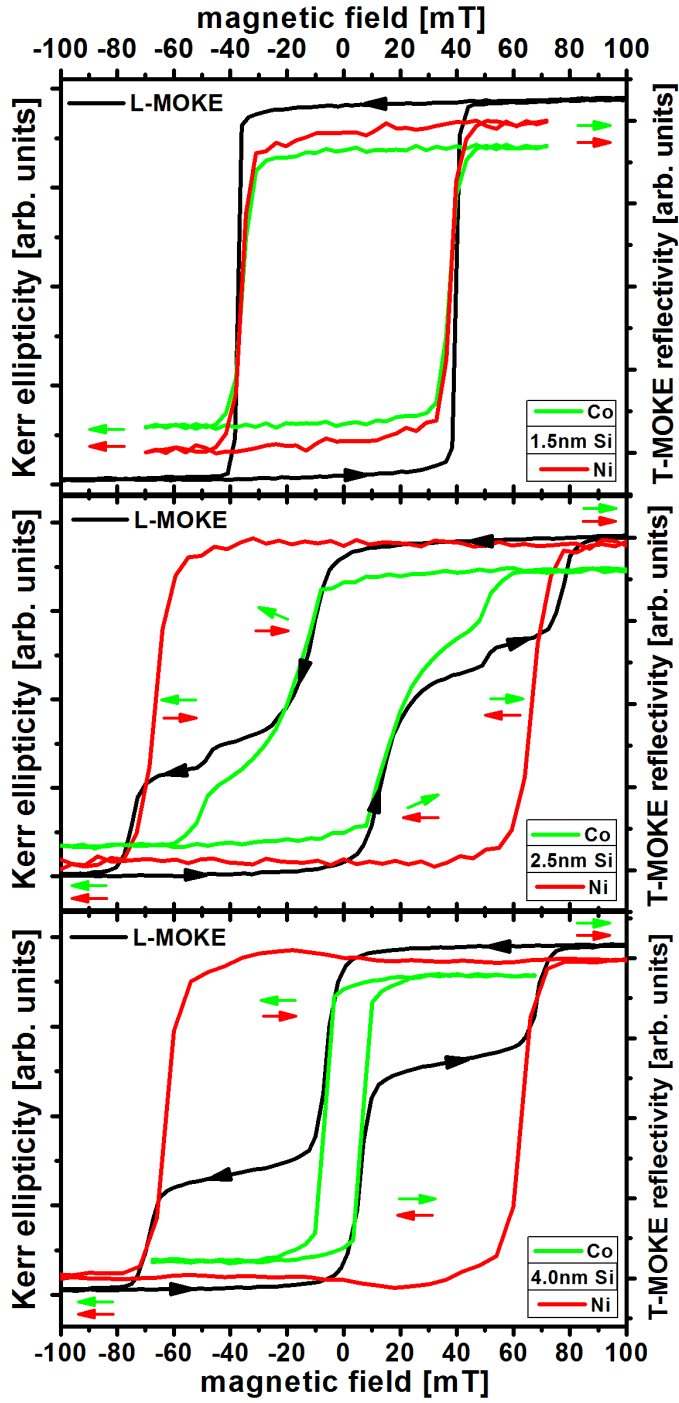


Figure 4.4: Magneto-optical loops of the multilayer wedge system taken at a Si spacer thickness of 1.5 nm (top), 2.5 nm (middle) and 4 nm (bottom).

of the loops taken at the Ni edge. The second switching event around ± 50 mT and the third step around ± 15 mT, coincide with steps of the magneto-optical loop taken at the Co edge. This analysis reveals that the Ni film in the Ni/Fe bilayer is magnetically harder and switches at higher magnetic fields. Whether this is an intrinsic property of the Ni film at that particular thickness, or whether the coercivity is caused by the ferromagnetic coupling to the adjacent Fe layer cannot be distinguished at this point. In any case, it is interesting to note that the larger coercivity of the Ni/Fe bottom layer is not dominating the magnetic response of the sample with strong ferromagnetic interlayer coupling, but rather moderately increases the coercivity to a value in between $H_C^{Co} \approx 15$ mT and $H_C^{Ni/Fe} \approx 75$ mT.

The bottom graph in figure 4.4 shows loops taken at a region where top and bottom ferromagnetic layers are separated by a Si spacer of 4 nm. Here, the conventional longitudinal MOKE loop (black curve) reveals only two pronounced steps, one of which can be clearly associated with the rectangular magneto-optical loop taken at the Ni absorption edge having a coercivity of $H_C^{Ni/Fe} \approx 70$ mT. The second step at ± 10 mT in the L-MOKE loop can be clearly related to the switching of the Co layer. This is the typical magnetization loop of a pseudo spin valve system with a negligible magnetic coupling between the hard (Ni/Fe) and soft (Co) magnetic layers.

Summarizing the findings and arguments given above, the switching behavior of this multilayer system can be mapped out and explored in detail. For a thin Si spacer, the layer stack is strongly ferromagnetically coupled throughout. The system behaves as one layer, having a coercivity that lies in between the coercivities of the individual decoupled layers, H_C^{Co} and $H_C^{Ni/Fe}$. The region of the layer stack with a thick Si interlayer is magnetically decoupled allowing for an independent switching of the top and bottom layers. For an intermediate spacer thickness the top Co layer switches first, but it is still weakly coupled to the bottom Ni layer, which governs the switching behavior because of a much higher volume magnetization. This also explains a higher coercivity and a gradual rather than abrupt switching of the Co layer as compared to the decoupled case. Moreover, the system is probably not homogeneous with respect to the coupling strength. This is suggested by the small additional steps in the Co-related loops, which can be found around ± 50 mT. These may be related to areas with an increased ferromagnetic coupling (for example, due to pinholes), which switch at higher magnetic field values.

4.1.4 Magneto-Optical Crosstalk and Interferences

It is important to note that layer-selective magneto-optical loops, which can be directly compared with their corresponding classical Kerr effect counterparts, as shown in figure 4.4, can usually be obtained only for a specific set of angles and photon energies. In order to elaborate on this finding a set of hysteresis loops taken at a fixed angle of 45° , in a photon energy range of 57 eV to 68 eV and at a Si spacer thickness of 4 nm is shown in figure 4.5. By scanning the photon energy across the Co and Ni absorption edges the shape of the recorded magneto-optical loops changes significantly. It is striking that all loops are considered to be a linear combination of the pristine loops associated with the individual switching of the Co and Ni layers. Even at local extrema of the magnetic asymmetry, namely at 59 eV, 61 eV and 66 eV - compare figure 4.3, supposedly layer-selective magneto-optical loops leave doubt about a decoupled state of the sample.

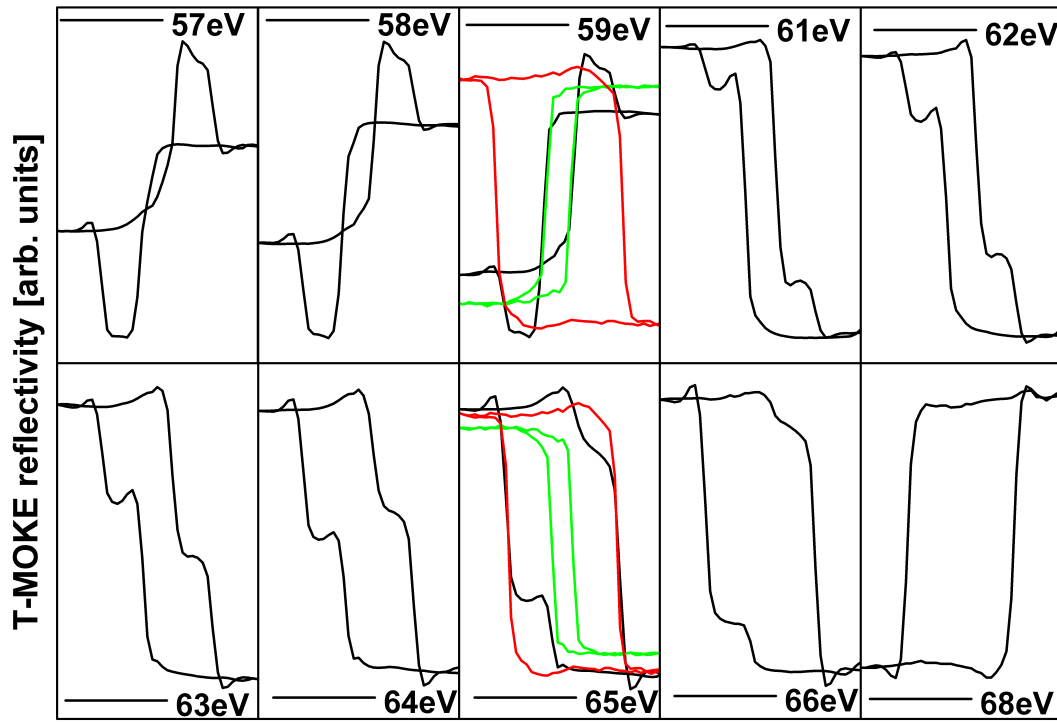


Figure 4.5: Magneto-optical loops taken at an angle of 45° , a Si spacer thickness of 4 nm and in a energy range of 57 eV to 68 eV.

But this behavior can be understood by firstly taking into account the switching of the 2 nm thin Fe layer at the very bottom of the multilayer and by secondly considering the strength and character of the magnetic dichroism at the M absorption edges. The Fe and Ni layer, having direct contact to each other, are strongly coupled and switch simultaneously. That is why recording a magneto-optical loop at the Fe and Ni edge would yield the same shape. Due to the energetic proximity of the M absorption edges of Fe (54 eV), Co (60 eV) and Ni (66 eV) and the width of the 3d bands, the electrons are excited into for magnetic contrast generation, the magneto-optical response of a single element is spread over several eV, thereby reaching into the response of a neighboring element. This context is depicted in figure 4.6, which shows the real and imaginary part of the dielectric tensor element ϵ_{xy} for the elements of iron, cobalt and nickel. The shown curves are derived from the magneto-optical constants determined by measurements of Faraday rotation spectra in previous experiments [37] and the off-diagonal tensor element has been linked to the origin of the magneto-optical Kerr effect in section 2.1. Therefore, as can be seen from the left graph in figure 4.6, the magneto-optical responses of Fe and Ni are clearly separated, basically vanishing in a region of 60 eV to 62 eV. The right graph in figure 4.6 reveals, on the other hand, that the response at the Co absorption edge reaches from approximately 56 eV to about 64 eV, thereby extending into the resonances of Fe and Ni.

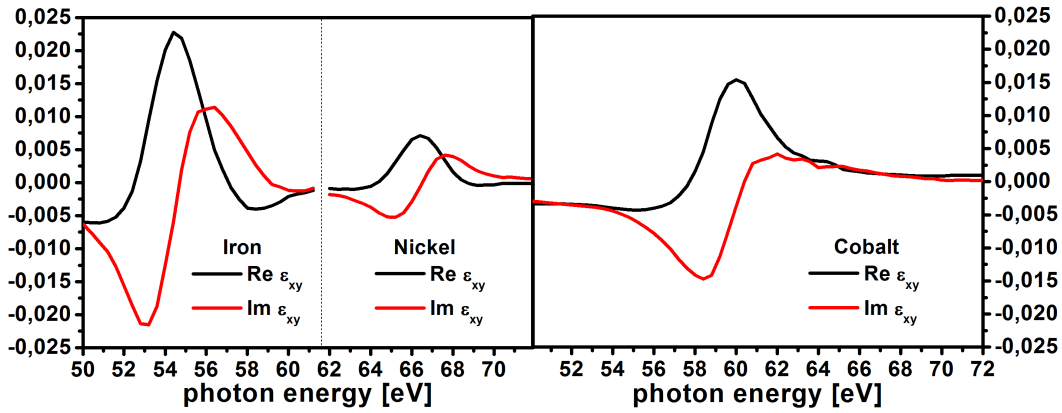


Figure 4.6: Real and imaginary part of the dielectric tensor element ϵ_{xy} of Fe, Ni (left) and Co (right) single films, derived from Faraday rotation spectra[37].

Besides this crosstalk, interferences play a role in the magneto-optical response of the multilayer. As has been outlined above, changing the thickness of the non-magnetic interlayer can influence the magneto-optical response of individual layers as well as the

multilayer as a whole, resulting in an energetic shift of the magneto-dichroic signal. As a consequence, the overall magneto-optical response at the Co layer is influenced by the response of the Fe and Ni layer and vice versa resulting in an energy dependent superposition of the measured magneto-optical loops. Figure 4.5 and basic calculations reveal, for photon energies below 60 eV, that the measured magneto-optical loops can be reproduced by the weighted *difference* of two rectangular loops associated with the switching of the Fe and Co layers - compare layer-selective loops extracted from figure 4.4 and inserted into figure 4.5 at 59 eV. Whereas for photon energies above 60 eV, the measured magneto-optical loops can be reproduced by the weighted *sum* of two rectangular loops associated with the switching of the Ni and Co layers - compare layer-selective loops extracted from figure 4.4 and inserted into figure 4.5 at 65 eV. Only by recording a loop at the far end of the photon spectrum at 68 eV, it is possible to obtain a pristine magneto-optical loop proving that the multilayer is magnetically decoupled. The weight and relative sign of the magneto-optical loop superposition depends on the magneto-optical constants which can be calculated for each individual layer as well as the entire multilayer system on the basis of the magneto-optical formalism outlined above [54]. And that is also how layer-selectivity can be gained at arbitrary sets of angles and energies. Nevertheless, it has been demonstrated in the example above that it is preferable to choose the angle of incidence such that the magneto-optical response of individual layers is clearly separated.

4.1.5 Summary and Conclusion

Resonantly enhanced reflection spectra of a polycrystalline Co/Si/Ni/Fe multilayer wedge system have been measured in a T-MOKE geometry across the M absorption edges of Co and Ni. The character of the magnetic dichroism in the EUV and its potential for layer-selective investigations has been explored. To this end, the magneto-optical response as well as the switching behavior of the Co (5 nm) and Ni/Fe (8 nm, 2 nm) layers as a function of the interlayer coupling was measured by varying the angle of incidence, the photon energy and the Si spacer thickness.

It has been shown that the magnetic contrast at the M absorption edges of Co and Ni (59.5 eV and 66.5 eV) can be as large as 80 % and 25 %, respectively, near the Brewster angle in a comfortable 90° reflection geometry. By means of magneto-optical calculations it has been proven that the shift of local magnetic contrast maxima is related to interference effects in the multilayer system. By recording hysteresis loops for various incidence angles and photon energies it was possible to characterize the role played by magneto-optical interferences and crosstalk with regard to a layer-selective response of the multilayer stack. This consequently facilitated to understand the switching behavior of individually selected layers as a function of the ferromagnetic interlayer coupling, whose strength decreases with increasing spacer thickness.

4.2 An Anti-Ferromagnetically Coupled Multilayer

In contrast to the previous section where spatially separated but homogeneous and ferromagnetically coupled layers were studied, the following pages deal with magneto-optic investigations of a multilayer containing anti-ferromagnetically coupled heterogeneous layers, i.e. alloys based on the 3d transition metals iron, cobalt and nickel. It was shown that layer-selectivity can be obtained in the former class of systems, whereas it has to be proven for the latter type. By answering this imposing question for a wide range of multilayer systems and shifting magnetic studies into the little-explored extreme ultraviolet range, a potentially new point of view into fundamental mechanisms behind magnetic coupling phenomena can be added.

Even though multilayer systems, such as Fe/Cr/Fe, have been extensively studied over the past years, the variety as well as complexity of the interaction between two adjoining ferromagnetic layers can still not be accounted for entirely. On the one hand, their interesting coupling properties can be related to phenomena, such as dipolar or interlayer exchange coupling [92, 93], but on the other hand, complicated effects associated with the interface of the involved materials, such as twisted states or proximity effects [94, 95], aggravate a deeper understanding. That is why the following experiment studies a multilayer system, which is based on a well-known, strongly exchange coupled Fe/Cr/Fe trilayer. In order to benefit from element- and thus layer-selectivity, however, the bottom and top layers are alloyed with Co and Ni, respectively, with regard to an elaborate investigation of a magnetic contrast mechanism which overcomes rather bulk sensitive approaches in the visible range.

4.2.1 Sample Preparation and Characterization

The sample consisted of a magnetic bilayer structure and was prepared by thermal evaporation at a base pressure of 5×10^{-11} mbar [90]. In a first step a substrate system for the magnetic multilayer was manufactured comprising a 150 nm thick Ag $\langle 001 \rangle$ buffer layer [91], which was grown on an iron precovered GaAs $\langle 001 \rangle$ wafer at a temperature of 380 K. After annealing at a temperature of 570 K, a 10 nm $\text{Co}_{40}\text{Fe}_{60}$ layer was deposited onto the buffer at room temperature by co-evaporation of Co and Fe at individually monitored deposition rates, which are characteristic for the pursued stoichiometry. A 0.6 nm Cr interlayer and a 5 nm $\text{Ni}_{80}\text{Fe}_{20}$ (permalloy) layer from a single target were deposited on top of that and finally this multilayer was capped by 3 nm Al to prevent oxidation. The thickness of the Cr interlayer was derived from previous experiments, which investigated the influence of the interlayer thickness on the coupling behavior in this multilayer system. For reference purposes single $\text{Co}_{40}\text{Fe}_{60}$ as well as $\text{Ni}_{80}\text{Fe}_{20}$ layers of 5 nm thickness were manufactured on the same buffer system.

The magnetic switching behavior in the plane of the multilayer system was first characterized by MOKE measurements in the visible range (compare section 3.4). Recording hysteresis loops in a longitudinal MOKE setup for various angles of all three samples with respect to the external magnetic field revealed a fourfold magneto-crystalline anisotropy in the $\text{Co}_{40}\text{Fe}_{60}$ layer exhibiting an easy axis along the $\langle 100 \rangle$ direction and a hard axis along the $\langle 110 \rangle$ direction. Only a negligible magneto-crystalline anisotropy could be found in the presumably polycrystalline $\text{Ni}_{80}\text{Fe}_{20}$ layer. The anisotropy of both single layers was measured to be translated into the multilayer system, whose magneto-optical hysteresis loop along its easy axis can be seen in the left graph of figure 4.7.

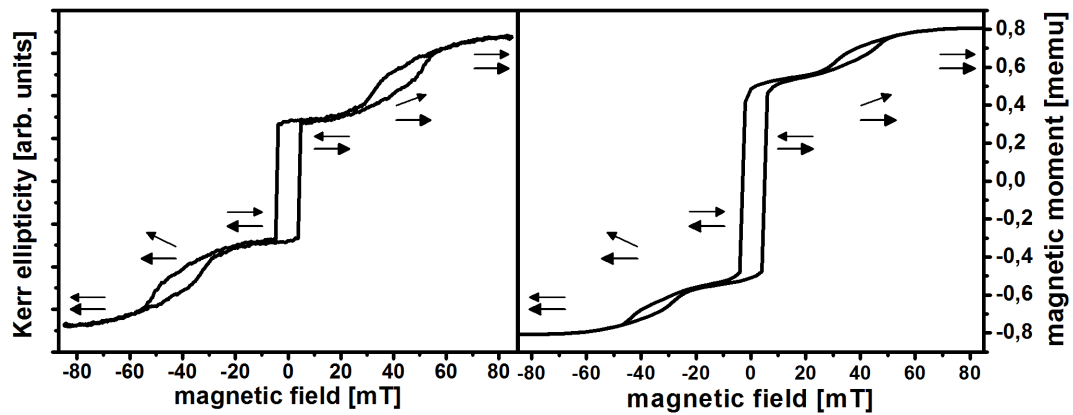


Figure 4.7: Hysteresis loops of the $\text{Ni}_{80}\text{Fe}_{20}/\text{Cr}/\text{Co}_{40}\text{Fe}_{60}$ multilayer measured at room temperature with MOKE (left) and SQUID (right). The arrows indicate the orientation of the magnetic layers as a function of the applied magnetic field.

For the sake of simplicity, the hysteretic behavior of all samples was investigated by applying a magnetic field only along their easy axes in the following. A SQUID magnetometer was employed in order to account for magneto-optical effects by referring to the absolute magnetic moment. Both single layers showed a rectangular hysteresis loop with a coercivity of 4 mT for the $\text{Co}_{40}\text{Fe}_{60}$ layer and a coercivity of 1.5 mT for the permalloy layer. The multilayer, on the other hand, produced a hysteresis loop which could be attributed to the anti-ferromagnetic coupling of the bottom layer and the top layer, as can be clearly concluded from the loops depicted in figure 4.7.

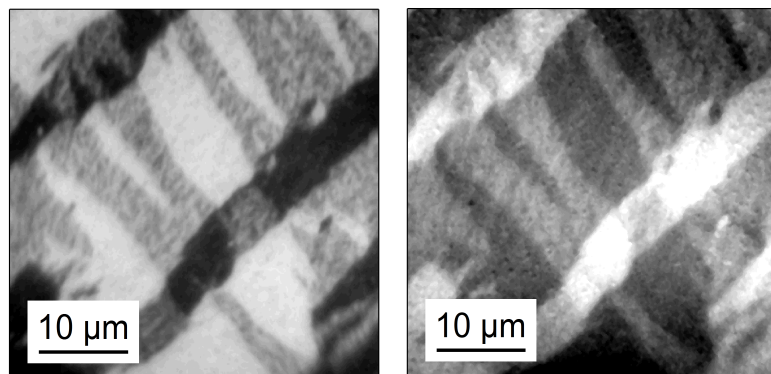
By taking into account the thicknesses of the top layer (5 nm) and the bottom layer (10 nm) as well as the saturation magnetization derived from SQUID measurements of the individual materials, $\text{Ni}_{80}\text{Fe}_{20}$ (≈ 1 T) and $\text{Co}_{40}\text{Fe}_{60}$ (≈ 2 T), the switching behavior of the multilayer can be understood in detail. Above 50 mT the multilayer is saturated and both layers point into the same direction. As the magnetic field

decreases, the top layer starts to reverse its magnetization until an antiparallel alignment is reached around 10 mT. Once the magnetic field exceeds the coercive field of the bottom layer at -4 mT, its magnetization flips into the field direction followed by an immediate reversal of the top layer to maintain the preferred antiparallel configuration. When the magnetic field is decreased even further, the top layer starts to reverse again until the multilayer saturates in a parallel state below -50 mT.

A comparison of the loops recorded with the MOKE setup and the SQUID reveals a qualitative agreement and a quantitative discrepancy. This observation can be explained by the fact that both techniques can accurately detect changes of the magnetization and thus the switching behavior is properly reflected by both methods. However, only the SQUID can determine the absolute magnetic moment, whereas the MOKE signal depends on the strength and direction of the magneto-optical effect in a ferromagnetic layer, the reflectivity at the interfaces, and the penetration depth of the light. And this is also the most likely explanation for the signal of the top permalloy layer to be more pronounced in the MOKE than in the SQUID hysteresis loop.

The anti-ferromagnetic configuration was confirmed in remanence by exploiting the x-ray magnetic circular dichroism (XMCD) in combination with a photoemission electron microscope (PEEM) [96]. Tuned to the L_2 absorption edges of Ni (854 eV) and Co (780 eV), the PEEM is capable to image the magnetic domain structure of this multilayer and to distinguish between the bottom and the top layer due to the resonant excitation of the electron system. In the generated pictures, which are displayed in figure 4.8, the grey scale represents the orientation of the in-plane magnetization. By comparing both images, it can be seen that the magnetic contrast is spatially correlated in a complementary manner, which proves the magnetic alignment for each domain to be anti-ferromagnetic. Moreover, the complex domain structure indicates that a magnetization reversal proceeds mainly via domain wall nucleation and motion rather than magnetization rotation.

Figure 4.8: PEEM images of the top $\text{Ni}_{80}\text{Fe}_{20}$ (left) and the bottom $\text{Co}_{40}\text{Fe}_{60}$ (right) layer taken in remanence at the L_2 edge of Ni (854 eV) and Co (780 eV).



4.2.2 Magneto-Optical Response in the EUV

In order to further characterize the magnetic multilayer, resonant magnetic reflectivity measurements were performed in a T-MOKE geometry at the synchrotron. The sample was placed in a reflectometer (see section 3.5) and the reflectivity of linearly p-polarized EUV light was measured across the M absorption edges of Fe, Co and Ni from 52 eV to 72 eV with an energy resolution of 0.1 eV and in steps of 0.25 eV. The absorption edge of the Al filter located at 72 eV, placed on the photodiode to block visible stray light, determined the upper photon energy limit of this study. In contrast to the previous reflectivity experiment focusing on only the Co and Ni M edges; however, the lower photon energy limit of 57 eV could be artificially decreased to 52 eV to include the Fe M edge around 54 eV at the expense of the overall photon flux.

This has been accomplished by slightly misaligning the optical path of the beam emitted from the undulator to admit a more red-shifted portion of the generated synchrotron light into the beamline. By changing the observation angle ϑ with respect to the undulator axis longer wavelengths are accessible, as can be seen from the undulator equation 3.2 in section 3.1. This reduction in the photon energy is accompanied by a reduction of the photon flux, as the observation angle moves away from the maximum of the Lorentzian dipole emission cone. In order to decrease the photon energy from 58 eV to 52 eV, a ϑ of 0.25 mrad was introduced by the focusing mirrors behind the undulator and the undulator-monochromator synchronization had to be reprogrammed, resulting in 85% reduction of the photon flux.

In a first step of the synchrotron T-MOKE experiment, we scanned the photon energy across the Fe, Co and Ni edges from 52 eV to 72 eV for all three samples in order to determine the conditions for a maximum of the element-specific magneto-dichroic signal, the result of which is displayed in figure 4.9. In this energy range we measured the magnetic asymmetry A around the Brewster angle from 38° to 52° with a magnetic field reversing between ± 100 mT, i.e. magnetically saturating each sample in opposite directions.

In the top graph of figure 4.9 the angular and energy dependent magnetic asymmetry of the single $\text{Ni}_{80}\text{Fe}_{20}$ layer is shown. Two pronounced bipolar peak structures can be identified in this asymmetry distribution associated with the elements of Ni and Fe. The former is located at an energy of 66 eV (68 eV) and an angle of 45° (49°) with an amplitude of about 25 % (-11 %), whereas the latter can be found at an energy of 54 eV (57 eV) and an angle of 46° (47°) with an amplitude of about 21 % (-10 %).

In the middle graph of figure 4.9 the angular and energy dependent magnetic asymmetry of the single $\text{Co}_{40}\text{Fe}_{60}$ layer is shown. Similar to the permalloy layer, two pronounced bipolar peak structures can be identified in this asymmetry distribution, one which can be associated with the Co and the other with the Fe M absorption edge, respectively. Interestingly, the overall appearance of the magneto-optical response of this layer resembles the response of the $\text{Ni}_{80}\text{Fe}_{20}$ layer, whose Ni is replaced by the

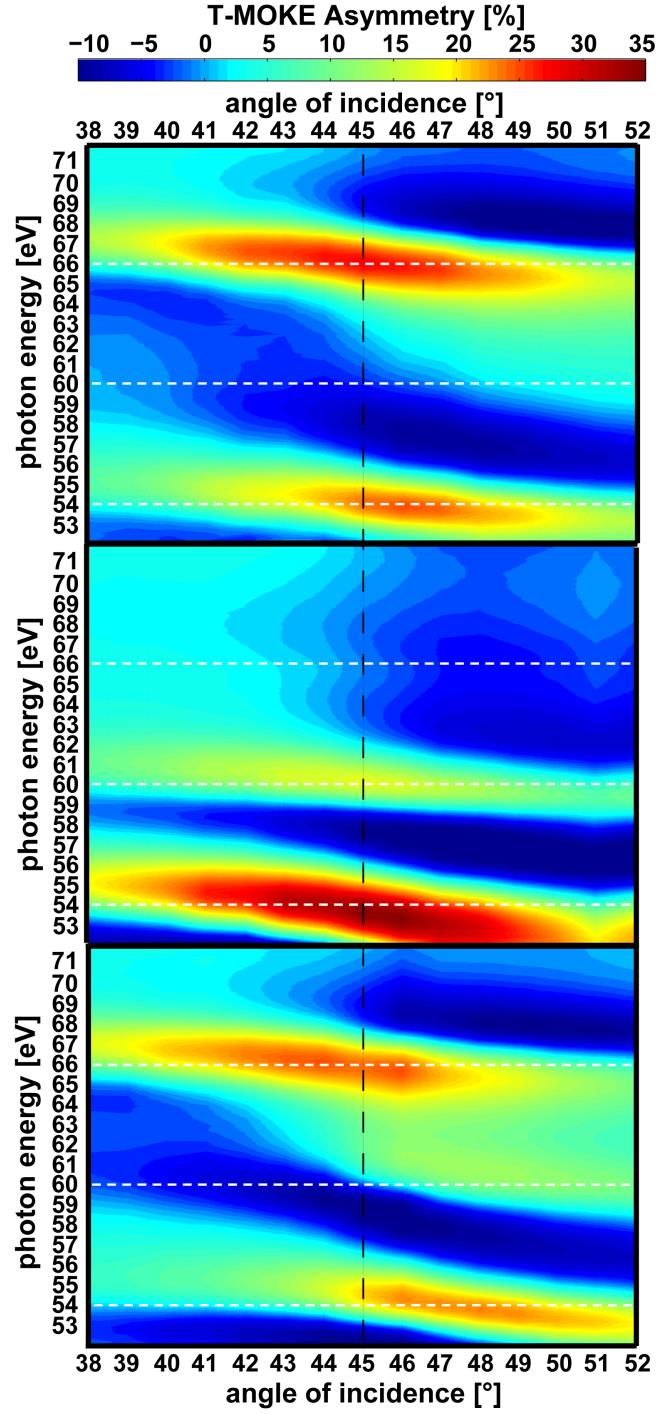


Figure 4.9: Angular and energy dependent magnetic asymmetry of the single $\text{Ni}_{80}\text{Fe}_{20}$ layer (top), the single $\text{Co}_{40}\text{Fe}_{60}$ layer (middle) and the entire $\text{Ni}_{80}\text{Fe}_{20}/\text{Cr}/\text{Co}_{40}\text{Fe}_{60}$ multilayer (bottom). The positions of the atomic absorption edges of Fe (54 eV), Co (60 eV) and Ni (66 eV) are indicated by horizontal white dashed lines.

element of Co. For the latter element, the angle of the resonance at 45° (49°) remains the same, changing to lower photon energies of 60 eV (62 eV), and to an amplitude of about 12 % (-9 %) only. The response at the Fe edge changes mostly in amplitude 34 % (-12 %), while the angle 45° (47°) and the photon energy 54 eV (57 eV) of this resonance stay approximately the same.

In the bottom graph of figure 4.9 the angular and energy dependent magnetic asymmetry of the multilayer is shown. Although the bipolar peak structures appear to have relocated, the magneto-optical response seems to be a superposition of the individual single layer responses in first approximation. In order to elaborate on this behavior scans of the magnetic asymmetry have been extracted from all three graphs of figure 4.9 for a fixed incidence angle of 45° . These are marked by a dashed line in the same figure and are displayed separately in figure 4.10.

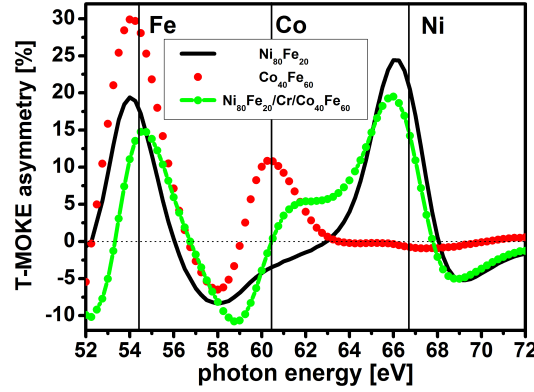


Figure 4.10: Magnetic asymmetry spectra for a single $\text{Ni}_{80}\text{Fe}_{20}$ layer (5 nm), a single $\text{Co}_{40}\text{Fe}_{60}$ layer (5 nm) and the $\text{Ni}_{80}\text{Fe}_{20}/\text{Cr}/\text{Co}_{40}\text{Fe}_{60}$ multilayer stack (5 nm/0.6 nm/10 nm) taken at a fixed incidence angle of 45° .

Again, it can be seen that the magneto-optical response of the single layers show distinct extrema of the magnetic asymmetry located around their respective absorption edges, whose approximate positions are indicated by vertical lines in figure 4.10, whereas the response of the multilayer can approximately be considered a superposition thereof. The magnetic asymmetry of the single $\text{Ni}_{80}\text{Fe}_{20}$ layer (black line) has a maximum of 20 % at 54 eV accompanied by a minimum of -10 % at 58 eV both located around the Fe absorption edge, and a maximum of 25 % at 66 eV with a small minimum of -5 % at 69 eV located around the Ni absorption edge. The single $\text{Co}_{40}\text{Fe}_{60}$ layer (red dots) shows maxima of the magnetic asymmetry at the Fe (30 %) and Co (10 %) absorption edges which seem to share a common minimum of -7 % close to 58 eV. The merging of several bipolar shaped resonances of the magnetic asymmetry, which are located around an absorption edge, can be understood by taking into ac-

count the energetic proximity and width of the absorption edges causing a spread of the magneto-optical constants and thus response over several electron volt (compare section 4.1.4). The variation in height can most likely be explained by the unequal mixing ratios of the Fe and the Co/Ni forming the respective alloys. The magnetic asymmetry of the multilayer system (green dotted line) resembles the response of both single layers. It is striking that not only the amplitude of the extrema at the Fe and Co absorption edges have changed, but also have they moved by about 1 eV to higher photon energies, whereas the maxima and minima at the Ni edge barely moved, changing in amplitude only. As has been shown in section 4.1.2, these phenomena can most likely be attributed to thickness dependent interferences of the EUV light at the interfaces of the multilayer.

4.2.3 Magnetic Switching Behavior

After having identified the maxima of the magneto-dichroic signal at the M absorption edges of Fe, Ni and Co, the photon energy can be tuned to probe the magnetic switching behavior element-selectively, which in the case of a multilayer system is supposed to translate into a layer-specific response. To this end, the magnetic field dependence of the T-MOKE reflectivity has been recorded resulting in hysteresis-like loops which only indirectly reflect the switching behavior of the sample magnetization, as the recorded signal comprises both magnetic and magneto-optical contributions. A set of these *magneto-optical loops* was measured in steps of 1 eV from 52 eV to 72 eV in order to discern the magnetic switching behavior from the magneto-optical response. This discrimination is achieved by comparing the recorded loops with the loops taken by the above-mentioned SQUID magnetometer and L-MOKE setup.

In order to elaborate on how to exploit the magneto-optical response of the multilayer to attain a layer-selective response, selected magneto-optical loops are displayed in figure 4.11. They were recorded at 58 eV for the response of the bottom layer, at 69 eV for the response of the top layer and at 61 eV showing the response of the entire multilayer system. It is important to note that these photon energies had to be specifically chosen, because it was observed that for most photon energies, and even at local extrema of the magnetic asymmetry at the Co M edge, the recorded magneto-optical loops feature a strong superposition of the hysteretic behavior associated with the individual bottom and top layers. In contrast to the magneto-optical loops depicted in this figure, the majority of recorded loops share strong similarities with the pristine loops related to the switching properties of the top permalloy layer. It turned out that unlike in section 4.1.3, there is no simple procedure on how to choose the photon energy or incidence angle in order to isolate the response from a single element or layer, respectively.

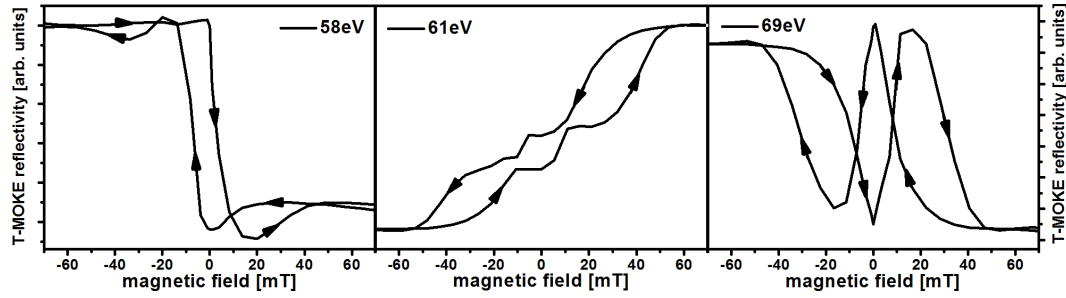


Figure 4.11: Magneto-optical hysteresis loops of the $\text{Ni}_{80}\text{Fe}_{20}/\text{Cr}/\text{Co}_{40}\text{Fe}_{60}$ multilayer taken at 45° and at photon energies of 58 eV, 61 eV and 69 eV.

The magneto-optical loop shown in the left graph of figure 4.11 mainly exhibits a rectangular shape reflecting an instant switching of the sample magnetization around ± 4 mT previously associated with the flipping of the bottom $\text{Co}_{40}\text{Fe}_{60}$ layer. The right graph of figure 4.11, on the other hand, shows a magneto-optical loop which exemplifies the multiple reversal of the top $\text{Ni}_{80}\text{Fe}_{20}$ layer. It begins to reverse its magnetization around 50 mT with a decreasing magnetic field until an anti-parallel alignment is reached at about 10 mT. Once the the magnetic field exceeds the coercive field of the $\text{Co}_{40}\text{Fe}_{60}$ layer around -4 mT, its magnetization flips to maintain the preferred anti-parallel configuration. When the magnetic field is decreased even further, this layer starts to reverse again until it saturates in parallel to the bottom layer below -50 mT.

The magneto-optical loop shown in the middle graph of figure 4.11 basically illustrates the switching behavior of the entire multilayer and falls into place if compared with both graphs of figure 4.7. Because the SQUID measurement is only sensitive to absolute magnetic moments, the amplitude of the recorded signal is not superimposed by a magneto-optical response, which may lead to a misrepresentation of the switching behavior. Depending on the strength and direction of the magneto-optical effect, the reflectivity at the interfaces and the penetration depth of the light, the response of one layer can dominate the recorded signal. This explains why the amplitude ratio between the signal from the top and bottom layers change from 1:3 in the case of the SQUID, to 1:1 in the case of the magneto-optical loop taken in the visible range and finally to about 3:1 in the case of the magneto-optical loop taken at 61 eV. As has been shown previously, interferences at the interfaces and the spread of the magneto-optical constants of Fe, Co and Ni in the EUV region over several electron volt can result in a magneto-optical crosstalk which affects a layer-selective response, because the reflected signal of both layers can be resonantly enhanced by

the same order of magnitude. In addition, it has to be considered that it is the top permalloy layer which is penetrated by the reflected light most thoroughly resulting in a dominance of the magnet-optical response. This can also explain the bumps in the magneto-optical loop shown in the right graph of figure 4.11 around ± 30 mT.

4.2.4 Summary and Conclusion

Resonantly enhanced reflectivity measurements of a $\text{Ni}_{80}\text{Fe}_{20}$ (5 nm) layer, a $\text{Co}_{40}\text{Fe}_{60}$ (5 nm) layer and a $\text{Ni}_{80}\text{Fe}_{20}/\text{Cr}/\text{Co}_{40}\text{Fe}_{60}$ (5 nm/0.6 nm/10 nm) multilayer system have been performed in a T-MOKE geometry across the M absorptions edges of Fe, Co and Ni. These measurements served as a starting point to explore the character of the magneto-dichroic signal in the EUV and its potential for layer-selective investigations of multilayers comprising 3d transition metal based alloys. For this purpose, the magneto-optical response as well as the switching behavior of the strongly anti-ferromagnetically coupled multilayer was measured by varying the angle of incidence and the photon energy.

It has been shown that the magnetic contrast at the M absorption edges of Fe, Co and Ni (54 eV, 60 eV and 66 eV) can be as large as 30 %, near the Brewster angle in a comfortable 90° reflection geometry. A comparison of the magneto-optical loops with hysteresis loops recorded by means of a MOKE in the visible range and a SQUID revealed that the response of the multilayer is dominated by the top $\text{Ni}_{80}\text{Fe}_{20}$ layer. Even though the individual switching of the bottom $\text{Co}_{40}\text{Fe}_{60}$ layer could be isolated for distinct photon energies and incidence angles, it was observed that for most photon energies and angles - even at local extrema of the magnetic asymmetry at the Co absorption edge - the recorded magneto-optical loops feature a strong superposition caused by magneto-optical crosstalk and interferences between neighboring elements and layers. In conclusion, it has to be acknowledged that there is no simple recipe for layer-selectivity in multilayer systems whose targeted layers comprise elements with energetically close absorption edges. Here, magneto-optical calculations and simulations may help to isolate the response of individual layers, which unfortunately could not be performed due to the lack of appropriate magneto-optical constants.

Magnetization Dynamics

This chapter deals with results obtained in pump-probe experiments employing a synchrotron light source as well as a table-top soft x-ray source. The following pages aim at examining the feasibility of resonantly scattered EUV light to serve as an element-selective probe for magnetization dynamics induced by ultrafast laser pulses exciting the magnetic system under investigation. For this purpose two types of experiments have been conducted in a T-MOKE geometry, one of which focuses on magnetization dynamics in the picosecond range of a thermally equilibrated magnetic system, whereas the other experiment studies ultrafast magnetization dynamics on the femtosecond timescale away from the thermal equilibrium of the magnetic system.

In the first experiment, precessional dynamics of the magnetization in thin permalloy films patterned to form a coplanar waveguide is induced by ultrashort laser pulses. The resulting oscillatory response is probed by synchronized EUV pulses originating from a synchrotron tuned to the M absorption edge of Ni. The obtained results in combination with reference measurements in visible range not only prove the practicability, but also explore the limitations of this pump-probe approach.

The second experiment is concerned with the ultrafast demagnetization of permalloy which is optically driven by intense laser pulses. The response is probed by inherently synchronized EUV pulses generated by a table-top soft x-ray source tuned to the M absorption edges of Fe and Ni. It is shown that a large magnetic contrast of up to 30% can be exploited to element-selectively probe the evolution of the magnetic system with an unprecedented temporal resolution. The results suggest that the local spin environment at the atomic level plays a vital role in the dynamic response of magnetic materials, and must be included for a complete understanding of the microscopic physics underlying ultrafast demagnetization processes.

Both experiments show the feasibility of pump-probe experiments on magnetic model systems in the extreme ultraviolet range. They pave the way to element-selectively probe magnetization dynamics and imaging domain structure on ultrafast femtosecond-to-attosecond time scales with a spatial resolution on the nanometer scale in a laboratory environment.

5.1 Time-Resolved Precessional Dynamics

The preceding chapter explored the potential for layer-selective measurements of the magnetization in complex multilayer systems in the extreme ultraviolet range. In the following, these experiments have been extended into the time domain to examine whether the response of a magnetic system to an external excitation can be probed element-selectively as well as time-resolved by exploiting the same magnetic contrast mechanism. Within this context, this study focuses on investigations of the magnetic precession for mainly two reasons. Besides photo-induced switching processes [16, 97, 98], precessional switching is known to be the fastest magnetic reversal process [14], worthwhile to be examined in the light of magnetic recording. Secondly, precessional dynamics proceeds on a timescale of picoseconds, which is still within the temporal resolution of the electron storage ring determined by the time structure of the synchrotron light pulse train (compare section 3.3). Thus, the limit for time-resolved experiments at the synchrotron can be scrutinized with regard to magnetic investigations by means of EUV radiation.

In a proof of principle pump-probe experiment precessional magnetization dynamics of a thin ferromagnetic film was measured by resonantly scattered EUV light in a T-MOKE geometry. For this purpose a thin layer of permalloy was placed onto a GaAs and Au based coplanar waveguide (CPW) provided with a photo-conductive switch. Focused laser pulses from a Ti:Sapphire oscillator triggered this electrically biased switch, which induced a magnetic pulse propagating along the CPW. Thus, the magnetization of the film system is excited out of its equilibrium direction. An external magnetic field applied along the waveguide forces the magnetization to precess into its original position. The temporal evolution of this reversible process is monitored by synchronized EUV pulses tuned to the M absorption edge of the material under investigation.

5.1.1 Sample Preparation and Characterization

The generation and propagation of a magnetic field pulse for the excitation of magnetization dynamics in the picosecond regime can be technically accomplished by a coplanar wave guide equipped with a photo-conductive switch [99]. A CPW comprises a microstrip line made from a highly conductive material, such as gold, which is placed in between two extended ground electrodes, as is schematically depicted in the left graph of figure 5.1. To provide electric pulses with a reasonable current density in the picosecond range, this structure is lithographically patterned on top of a GaAs substrate and it is interrupted by a photo-conductive switch. When ultra-short laser pulses are focused onto this electrically biased fingered structure,

electron hole pairs are generated in the substrate material. They are immediately accelerated towards the fingered electrodes closing the photo-conductive switch for a couple of picoseconds. Thus, an electric pulse is induced to propagate along the CPW. From the law of Biot-Savart follows that this electric current pulse is accompanied by an Oersted-field. This field can be large enough to magnetically excite a magnetic material deposited on top of the CPW.

In the first step of the sample fabrication, a set of cleaned and dried epitaxial GaAs substrates with a size of $1 \times 1 \text{ cm}^2$ have been spin coated at a speed of 4000 rpm with a UV sensitive photoresist (MicroChemicals - AZ5214E). After baking the coated substrates at a temperature of 90°C for 5 min, a negative development process by means of optical lithography followed. Using a mask aligner (Karl Süss - MA6), the resist was initially exposed to UV light for about 15 s through an optical mask structured with a CPW containing a photo-conductive switch. Subsequently, the substrates were baked for another 60 s at a temperature of 120°C and the hardened resist was subjected immediately thereafter to a flood exposure for 90 s without the optical mask. The substrates were finally immersed for up to 60 s into the developer (MicroChemicals - AZ326), which removed the portion of the resist illuminated in the very first exposure. The development process was terminated by rinsing the substrates with deionized water for about 2 min. The quality of the lithographic process was inspected by an optical microscope, before the patterned substrates moved on to the metal deposition. A microscope picture of this patterned structure can be seen in the right graph of figure 5.1.

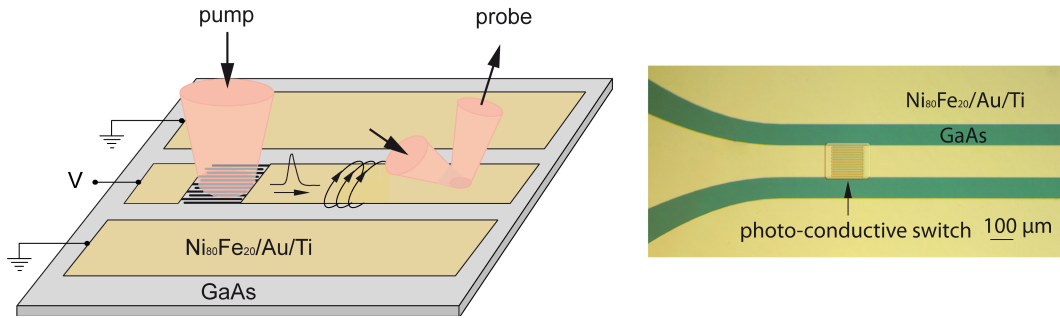


Figure 5.1: Schematic illustration of the coplanar waveguide equipped with a photo-conductive switch and the generation as well as propagation of a laser-induced magnetic field pulse (left); a microscope image of the lithographically fabricated structure (right).

Prior to the deposition process, all samples were cleaned by an Argon ion plasma for 15 s in the employed ion-beam sputtering machine [100, 101]. Subsequently, a 5 nm

Ti adhesion layer followed by a 150 nm Au layer were sputtered onto the patterned substrates. In the second step, a 50 nm permalloy layer capped with 2 nm Au was deposited on top of the Au/Ti bilayer, the latter of which serves to conduct the laser triggered current pulse along the patterned CPW. Finally, the patterned structures were uncovered by dissolving the remaining resist in a lift-off process in acetone. Again, the quality of the deposition and lift-off processes was visually inspected by means of an optical microscope, the result of which is displayed in the right graph of figure 5.1.

All samples were first characterized by static MOKE measurements in the visible range and a SQUID magnetometer with regard to a magneto-crystalline anisotropy as well as the switching behavior in the sample plane. Recording hysteresis loops for all samples in a longitudinal MOKE setup (see section 3.4) for various angles of the sample with respect to the external magnetic field revealed a negligible magneto-crystalline anisotropy. The SQUID measurement of the switching behavior showed nearly rectangular hysteresis loops with a coercivity of about 0.1 mT and a saturation magnetization of about 1 T.

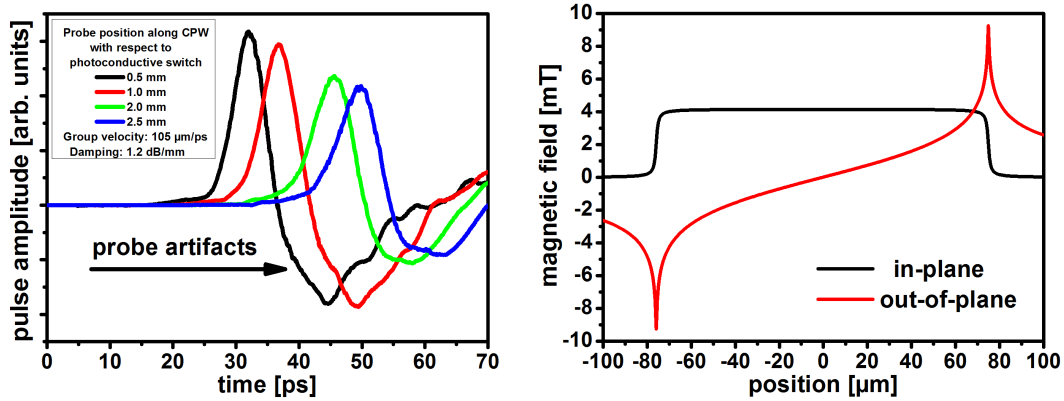


Figure 5.2: Resulting plot of the CPW characterization by photo-conductive sampling (left), which has been performed by the group of Dr. Michael Nagel at the IHT of the RWTH Aachen, and the simulation of the magnetic in-plane as well as out-of plane component generated by a current flowing through a rectangular waveguide of 150 μm x 150 nm (right).

For the following characterization steps, each sample was glued with silver paste to a single custom made holder based on a printed circuit board provided with electrical copper lines. Both ends of the CPW were wire-bonded to a spatially separate pair of lines, each of which was attached to a coaxial radio frequency connector

(SubMiniature version A - SMA). Thus, the CPW including the photo-conductive switch could be electrically biased via the central SMA line, whereas the ground pads of the sample remained on ground being bonded to the shield of the SMA plug. In order to minimize reflections of the current pulse at either end of the waveguide, one end was terminated by 50 Ohm via a corresponding SMA connection. This was made possible by paying attention to the impedance of the CPW in the development process of the waveguide. The impedance depends on the dimensions of the stripline, the gaps and the ground pads as well as the dielectric constants of the employed materials. A simulation program facilitated to adjust the appropriate parameters in the design of the optical mask defining the dimensions of the waveguide in the lithography process [102]. The other end of the waveguide was connected via the remaining SMA line to a bias tee, once the sample was placed in the corresponding setup for a laser induced excitation.

In order to determine the electric response of the switch and the waveguide, the mounted sample was characterized by photo-conductive sampling [103], the result of which is displayed in the left graph of figure 5.2. The graph reveals that a 20 fs laser pulse generates a nearly Gaussian current pulse with a length of about 5 ps (FWHM) at a distance of about 0.5 mm from the switch. By moving the photo-conductive probe along the stripline of the CPW with respect to the switch, the group velocity as well as the damping of the current pulse was determined to be $105 \mu\text{m}/\text{ps}$ and $1.2 \text{ dB}/\text{mm}$, respectively. The observed negative signal amplitudes at the end of each pulse are measurement artifacts related to internal reflections of the electric field probe, which can be disregarded. In addition, the distribution of the magnetic field around a rectangular bar with a width of $150 \mu\text{m}$ and a height of 150 nm has been simulated according to the law of Biot-Savart [104], assuming a current flow of 1 A. As can be seen from the right graph of figure 5.2, this calculation demonstrates that the magnetic in-plane component can be assumed constant right above the waveguide, whereas the out-of-plane component exhibits a strong variation over the width of the stripline. However, in the middle of the waveguide the out-of-plane component is close to zero and can therefore be neglected. Thus, the assumption of the magnetic field exciting the material in the sample plane and perpendicular to the CPW is justified.

5.1.2 Time-Resolved MOKE in the Visible Range

Before proceeding to the pump-probe experiments at the synchrotron, the magneto-dynamic response of the fabricated samples was characterized in a time-resolved MOKE experiment in the visible range, the setup of which has been introduced in section 3.4. As already indicated schematically in the left graph of figure 5.1, the central line of the waveguide is biased with a voltage of about 10-20 V. Laser

pulses from a Ti:sapphire oscillator with a pulse length of about 100 fs and with a central wavelength of 760 nm are focused onto the photo-conductive switch. This triggers a train of 5 ps long current pump pulses to propagate along the CPW which is accompanied by a magnetic field of the same temporal structure. The field of the magnetic pulse is oriented perpendicular to the CPW and in the plane of the magnetic system deposited on top. The resulting precessional motion of the magnetization in the permalloy film is probed by inherently synchronized *p*-polarized light pulses generated by the same laser. To this end, the probe beam is attenuated and focused onto the stripline a few hundred microns off the switch at an incidence angle of about 30°. At this geometry and wavelength a change in the magnetization of the material induces a polarization change in the reflected beam. Thus, the magneto-dynamic response is detected as a function of the delay between pump and probe pulses as well as plotted against a magnetic field applied along the waveguide. It can be shown that the recorded magneto-optical signal is still dominated by the polar Kerr effect [80]. Therefore, this experiment determines the temporal evolution of the average magnetic out-of-plane component, projecting the three dimensional precession of the magnetization into an one dimensional oscillation.

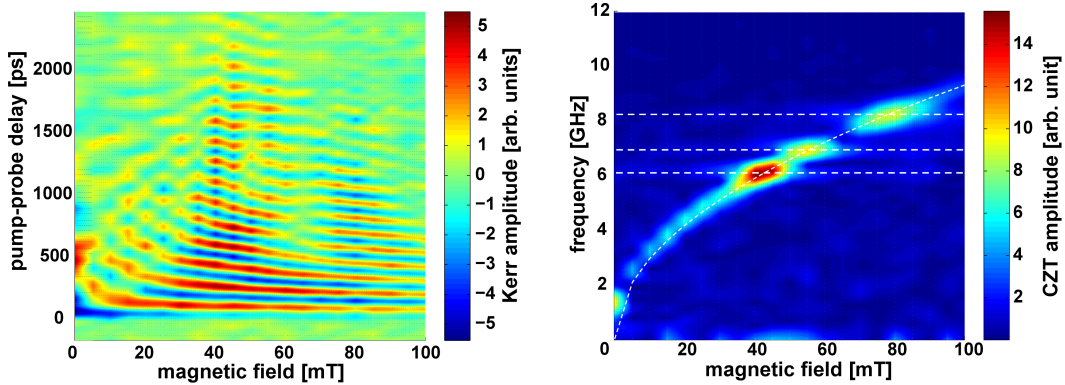


Figure 5.3: Temporal evolution of the Kerr signal as a function of the pump-probe delay and the magnetic field applied along the coplanar waveguide (left); the chirp-z-transform of the corresponding Kerr signals into the frequency domain (right).

The result of the experiment is displayed in figure 5.3, which shows the Kerr signal in the time domain on the left side and the corresponding transformations into the frequency domain on the right side. As can be seen from the left graph, the Kerr amplitude starts to oscillate with a period of about 650 ps at no magnetic field applied along the CPW, when the delay between the pump and the probe pulses equals zero, which in the following is referred to as $\Delta t = 0$. The period of the oscillation steadily de-

creases with an increasing field to about 160 ps at a field strength of 100 mT. Although the maximum of the oscillation amplitude does not change much as a function of the magnetic field, the duration of the oscillation varies significantly with its strength. The damping of the oscillation minimizes at 45 mT, 55 mT and 80 mT.

This behavior can be understood by analyzing the time-resolved Kerr signal in the frequency domain, which is displayed in the right graph of figure 5.3. The transformation has been accomplished by a chirp Z transform (CZT) algorithm allowing for an arbitrary scaling of the frequency axis as opposed to a Fourier transform [105]. The graph mainly shows four frequency modes, which have been marked by white dashed lines. The most pronounced mode, the leading frequency of the Kerr signal, shifts to higher values with an increasing magnetic field. In addition, it can be seen how the amplitude of this mode is enhanced at 45 mT, 55 mT and 80 mT, when it crosses three modes oscillating at 6.2 GHz, 6.9 GHz and 8.3 GHz, which do not seem to be affected by the external magnetic field. The observed shift of the field dependent mode is in very good agreement with calculations of the ferromagnetic resonance (FMR) frequency in a plane material with a saturation magnetization M_s subjected to an external static field H_0 [106]:

$$\omega = \gamma \sqrt{H_0 4\pi M_s}, \quad (5.1)$$

with ω being the resonance frequency and γ denoting the gyromagnetic ratio. Assuming a γ of $2.93 \frac{\text{GHz}}{10\text{T}}$ and taking into account the previously measured saturation magnetization of the permalloy sample $4\pi M_s = 1\text{T}$, the measured frequency shift closely follows the so-determined root function, which has been inserted as a dashed white line into the right graph of figure 5.3. The non zero response around $H_0 = 0$ can be explained by the shape anisotropy of the waveguide, since the width of the signal line is finite [107].

In order to elaborate on the behavior observed at the crossing of two modes, resulting in the enhancement of the frequency amplitude as well as the length of the Kerr oscillation, several time-resolved traces and their corresponding frequency transforms have been extracted from figure 5.3 in a vicinity of 45 mT and are separately displayed in figure 5.4. It can be seen from the left graphs of this figure how the damping of the oscillation slowly decreases with an increasing magnetic field, minimizing around 45 mT and how it increases once this field strength is exceeded. Even though it is hard to identify several frequency modes in the time-resolved amplitudes of the Kerr signals, the beating pattern in some traces already point towards their presence. In the right graphs, on the other hand, several modes can be observed in the frequency domain, which are constant with respect to the external magnetic field. The most pronounced modes are indicated by vertical black lines in the same figure and they

correspond to the horizontal white dashed lines in figure 5.3. As the magnetic field is increased the mode previously associated with the FMR traverses the spectrum and its frequency amplitude is amplified when it approaches and crosses the constant mode. Interestingly, the amplitude of the enhanced mode is much higher than the sum of the single modes separated in frequency space. This points towards a resonantly enhanced mode-mode coupling and energy conversion, which has already been observed in previous studies focusing on rather confined magnetic geometries [80, 108]. The origin of the constant modes may be related to reflections of the magnetic field pulse at the the end of the waveguide or to the shape-anisotropy introduced by the finite dimensions of the CPW. However, it is of little importance to the objective of this study to perform an element-selective pump-probe experiment at the synchrotron.

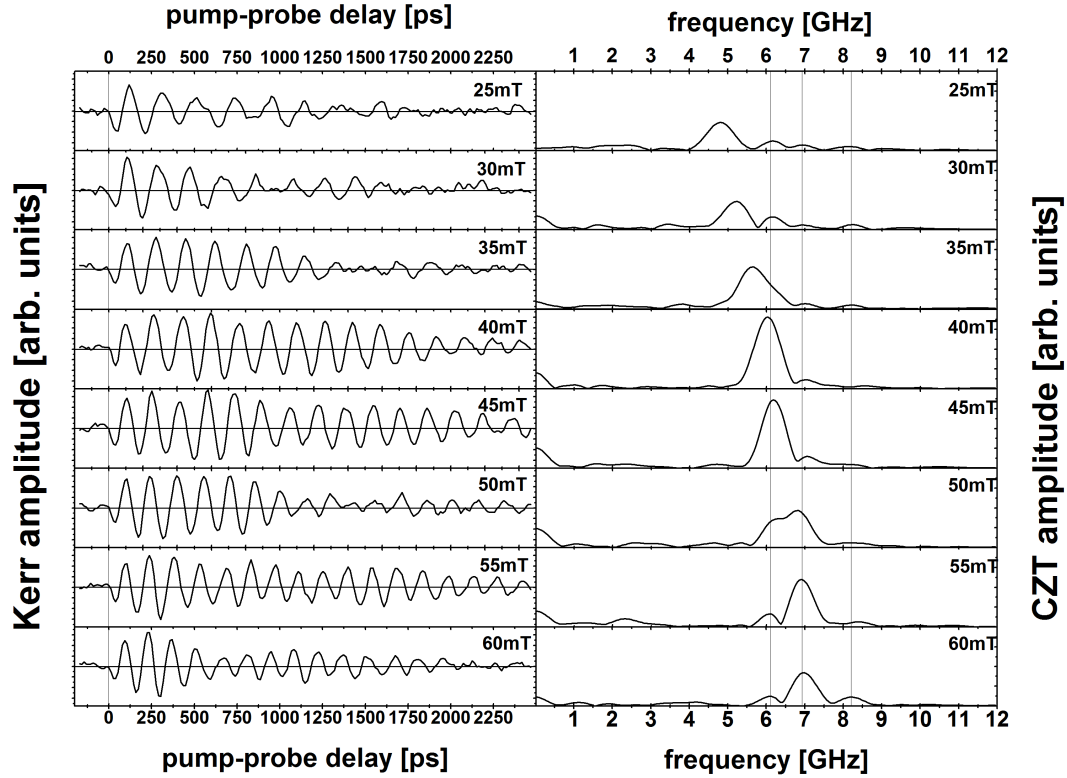


Figure 5.4: Temporal evolution of the Kerr signal as a function of the pump-probe delay for selected magnetic fields applied along the coplanar waveguide (left); the chirp-z-transform of the corresponding Kerr signals into the frequency domain (right).

5.1.3 Time-Resolved MOKE in the EUV

After having characterized all samples statically as well as dynamically in the visible range, a single sample was placed into the reflectometer described in section 3.2. Similar to the dynamic experiment in the visible range, the axis of the stripline was aligned in the plane of incidence thereby maximizing the sensitivity of the dynamic T-MOKE experiment to a precessional trajectory of the magnetization. In first approximation, the magnetization is assumed to move on a spiral oriented perpendicular to the CPW. As a consequence, the arrangement of the magnetic coils in the sample chamber required to be modified to admit two sets of coils instead of one. The new pairs were capable to generate static magnetic fields of up to ± 80 mT and ± 100 mT along the vertical and the horizontal sample axes, respectively. After the adjustment of the reflectometer, all preparations were made to perform time-resolved experiments at the undulator beamline UE56/1-SGM at BESSY (compare section 3.3).

In the first step of the EUV experiment, the maximum of the magneto-dichroic contrast was determined. For this purpose, the static magneto-optical response of the magnetic film on the stripline was measured as a function of the incidence angle and the photon energy. In a T-MOKE geometry, the magnetic asymmetry was quantified in an angular range of 38° to 52° across the M absorption edge of Ni from 58 eV to 72 eV in steps of 0.2 eV. The sample was magnetically saturated in opposite directions by a vertical magnetic field reversing between ± 10 mT. The lower and the upper limits of the energy scans were determined by the minimum of the undulator gap and the absorption edge of the 200 nm Al filter covering the photodiode. The filter was placed in front of the avalanche photodiode to block the intense 1.55 eV light of the femtosecond laser employed to trigger the photo-conductive switch.

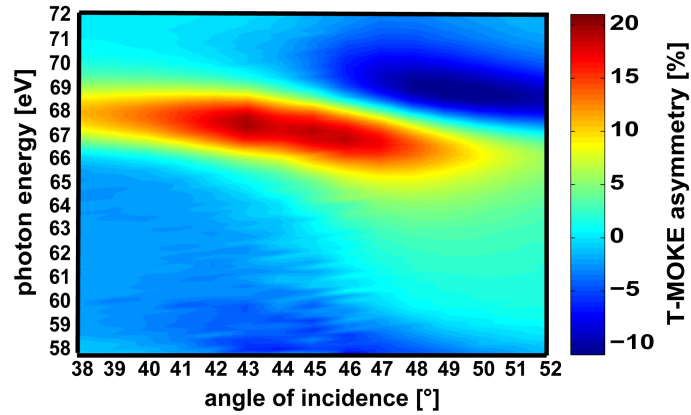


Figure 5.5: Angular and energy dependent magnetic asymmetry of the 50 nm permalloy layer capped with 2 nm Au taken at the stripline in the vicinity of the photo-conductive switch.

A comparison of the recorded asymmetry, which is displayed in figure 5.5, with measurements of a plane permalloy film shown previously in figure 4.9 reveals a strong similarity. A pronounced bipolar peak structure can be identified at the Ni M absorption edge. It can be clearly located at a photon energy of 67.5 eV (69 eV) and an incidence angle of 45° (49°) with an amplitude of about 20% (-11%). Small shifts in the asymmetry distribution regarding the incidence angle, the photon energy and the amplitude can be most likely explained by interferences due to the difference in the film thickness of the respective samples. It may also be related to calibration issues of the monochromator or the sample manipulator. Nevertheless, small shifts do not play a major role in the following pump-probe experiment.

As has been outlined in section 3.3, both the pulse train of the laser and the pulse train of the synchrotron, illustrated in the left graph of figure 5.6, have to be synchronized before time-resolved traces of magnetization dynamics can be recorded. This is accomplished by firstly biasing the switch and moving the sample in the horizontal plane until the synchrotron beam triggers the photo-conductive switch. The resulting pulse train is monitored by an oscilloscope connected to the CPW by means of a bias tee, the result of which is displayed in the bottom right graph of figure 5.6. In the second step, the laser beam is focused onto the switch in addition and the electronic synchronization unit is switched on. Thus, the pulse train of the synchrotron as well as the pulse train of the laser should be visible on the oscilloscope with a firm and jitter-free phase relation, as can be seen from the top right graph of figure 5.6. By moving the optical delay stage, the temporal shift of the pump pulse with respect to the probe pulse can be adjusted and monitored by the oscilloscope. That is also how the approximate position of $\Delta t = 0$ is determined. Finally, the sample is returned into the position, where the static EUV characterization has been performed, and the laser spot position has to be adjusted accordingly to trigger the photo-conductive switch.

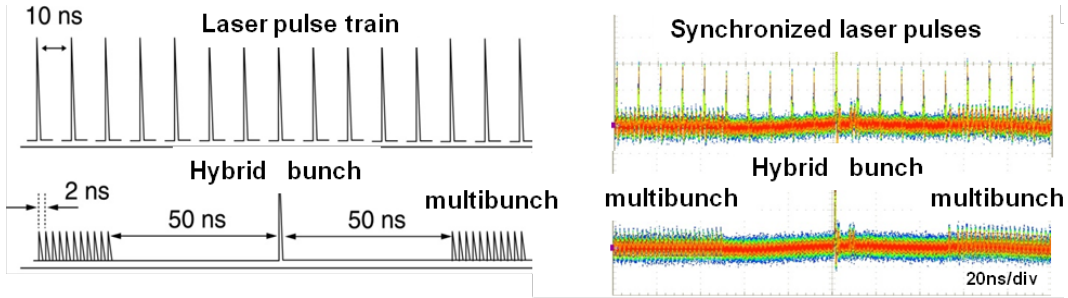


Figure 5.6: Schematic of the laser pulse train (top left) and the synchrotron pulse train in the multibunch mode (bottom left); oscilloscope picture of the synchrotron pulse train (bottom right) and the synchronized laser and synchrotron pulse trains (top right) measured with the photo-conductive switch of the CPW.

Once the alignment and synchronization procedures are accomplished, the photon energy is tuned to the predetermined maximum of the magnetic asymmetry. Here at 67.5 eV, traces of the T-MOKE reflectivity have been recorded as a function of the delay between pump and probe pulses, which are displayed as black curves in the left graphs of figure 5.7. Due to the limited amount of beamtime, transients for only three different magnetic fields could be measured, each of which was averaged over several injection periods of the storage ring. The right graphs of the same figure show their corresponding transformations into the frequency domain, which have been performed by the CZT algorithm. In order to compare the observed oscillation in the EUV with the data taken in the visible range, a single trace of the time-resolved Kerr amplitude as well as its frequency transform have been extracted from the preceding section and have been inserted as red curves into the middle graphs of the figure found below.

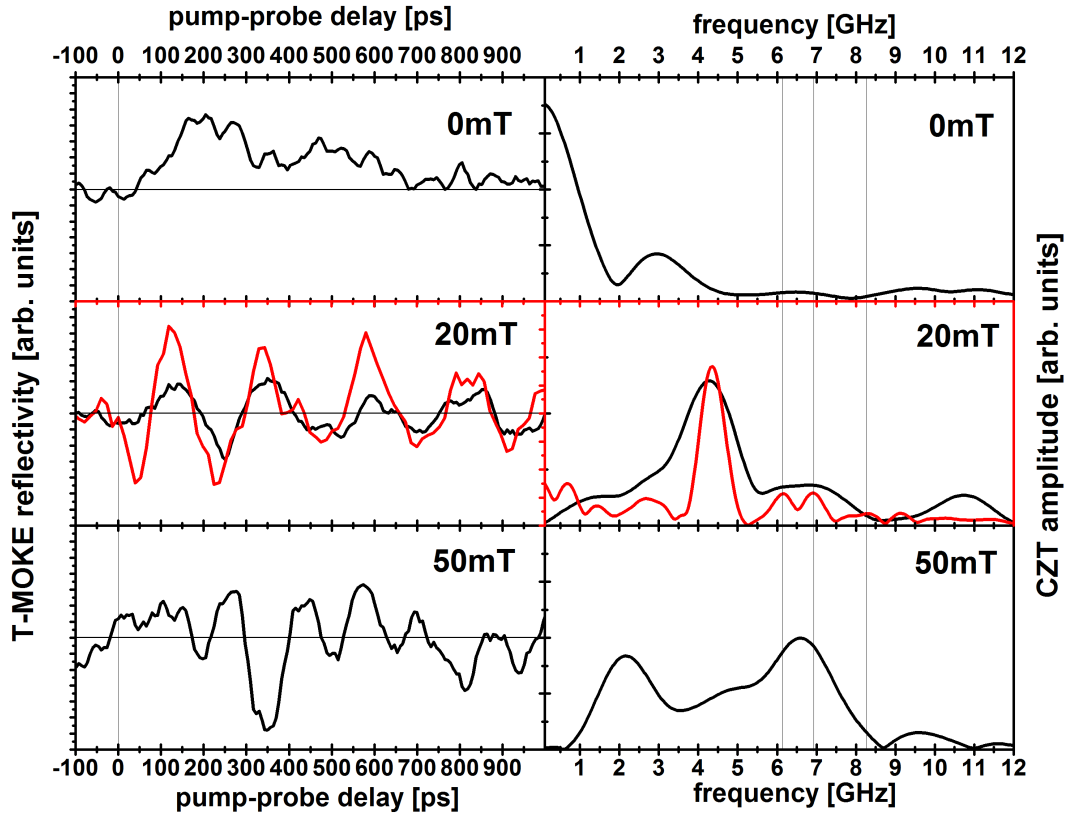


Figure 5.7: Temporal evolution of the T-MOKE reflectivity as a function of the pump-probe delay for selected magnetic fields applied along the coplanar waveguide (left); the chirp-z-transform of the corresponding Kerr signals into the frequency domain (right).

Similar to the the pump-probe experiment in the visible range, the oscillation period decreases with an increasing static magnetic field. The duration of the oscillations behaves oppositely, basically vanishing after 700 ps for no field applied along the CPW and extending beyond the recorded region for a finite field strength. The frequency spectra reveal that the leading frequency closely follows the previously identified root function related to the ferromagnetic resonance.

Comparing the time-resolved traces obtained in the visible range with the signal recorded in the EUV shows that both pump-probe experiments can reliably reproduce the precession of the magnetization in the permalloy film with a comparable signal-to-noise ratio. This also confirms the resonant nature of the latter technique, as no signal can be observed if the photon energy is tuned off the M absorption edge. Even though the oscillations match well in the time domain at 20 mT, a difference in the frequency domain can be identified. The positions of the maxima in the frequency space correspond quite accurately, whereas the width of the peaks differs significantly. The modes located at 6.2 GHz, 6.9 GHz and 8.3 GHz, which were identified in the visible range seem to have merged to a single mode in the case of the EUV. This observation is related to the sizable discrepancy of the probe pulse width, which is about 100 fs in the case of the fs-laser as opposed to 100 ps in the case of the synchrotron. That is also why, for magnetic fields above 50 mT no precession dynamics was observed. Here, the magnetic oscillation period becomes comparable to the EUV probe-pulse duration, thus setting a temporal resolution limit for time-resolved measurements in the single-bunch synchrotron operation mode.

In spite of the fact that a very large magnetic asymmetry has been observed in the static measurement (20%), the time-resolved investigation yields a unexpectedly weak signal. This is even more surprising, as the data acquisition time at the synchrotron exceeded the integration time dedicated for the same sample system in the optical laboratory. In addition, the lock-in detection scheme employed at the storage ring resembled the reference experiment in the visible range, to which end a much weaker magnetic contrast mechanism was exploited. From a general point of view, it has to be considered that in a static magneto-optical characterization, the sample magnetization reverses by a full 180° , whereas in the time-resolved measurement the signal only arises from a small perturbation of the magnetic alignment. Moreover, during the static measurement, the signal originates from a homogeneously magnetized film in contrast to the case of a pulse excitation, where the magnetic pulse propagates along the CPW thereby introducing a temporal smearing of approximately 3–5 ps. This is about the time necessary for the excitation pulse to traverse the probe spot. But these arguments apply to both pump-probe experiments and are independent of the wavelength employed.

Therefore, the reason for observing only relatively weak oscillations in the time-resolved synchrotron experiment in spite of a superior magnetic contrast has to be related to the temporal structure of the EUV pulse train and its synchronization to

the laser system. The performed measurements prove that the length of the probe pulse approaches and even exceeds the time resolution limit of the synchrotron. This fact in combination with any temporal jitter introduced to the synchronization of the pump and probe pulse trains impede the accurate mapping of the magneto-dynamic precession for magnetic fields larger than 50 mT. Due to the complexity of the setup and especially of the light source employed many origins can be asserted, starting with the electronic jitter of the 500 MHz bunch clock reference signal in the RF cables.

5.1.4 Summary and Conclusion

A thin layer of $\text{Ni}_{80}\text{Fe}_{20}$ was deposited onto a lithographically fabricated coplanar waveguide provided with a photo-conductive switch based on GaAs and Au. A characterization of this patterned structure revealed that focused laser pulses from a Ti:Sapphire oscillator generate electromagnetic pulses propagating along the CPW with a pulse length of about 5 ps (FWHM). Thus, the magnetization of the permalloy film is excited out of its equilibrium and an external magnetic field applied along the waveguide forces the magnetization to precess into its original position. A thorough magneto-dynamic characterization in the optical MOKE laboratory employing a pump-probe technique shows that the induced magnetization dynamics closely follows the ferromagnetic resonance and a strong resonantly enhanced energy conversion among various excited frequency modes is present.

At the synchrotron the magneto-optical characterization of the ferromagnetic film was performed employing extreme ultraviolet radiation tuned to the M absorption edge of Ni around 66 eV. Static reflectivity measurements in a T- MOKE geometry show a large magnetic contrast of up to 20 %. The magneto-dynamic response of this magnetic thin film to an ultrashort laser induced magnetic field pulse exhibits oscillations in a frequency range of up to 6.5 GHz associated with precessional magnetization dynamics of the ferromagnetic layer. These results can be correlated with the measurement performed in the visible range and demonstrate the feasibility of element-specific magneto-dynamic studies employing resonantly enhanced reflectivity at the M edges in the EUV.

Despite the huge magnetic contrast in the static experiment at short wavelengths, however, only a relatively weak oscillation amplitude is observed in relation to the approach at visible wavelengths. This is ascribed to the experiment approaching and exceeding the time resolution limit of the synchrotron and it might be even related to synchronization issues of the employed light sources. Considering the complexity of the experiment and a limited access to the required infrastructure, it remains to be seen whether the end justifies the means. As can be seen in the following section, a tabletop soft x-ray source producing ultrashort and coherent EUV pulses in a laboratory environment represents a viable alternative, especially so since photon energies of up to 100 eV can be attained with moderate effort.

5.2 Ultrafast Demagnetization Dynamics

In the previous section it was demonstrated that element-specific magneto-dynamic investigations employing resonantly enhanced reflectivity at the M absorption edges can be performed. Even though the feasibility of pump-probe experiments in the extreme ultraviolet range was proven, several limitations of a synchrotron based technique surfaced during the development as well as measurement process, such as the probe pulse duration of about 100 ps, concerns about the synchronization among the pump-probe pulse trains and the complexity as well as the limited availability of the required infrastructure. Currently, the former constraints are overcome if suitable light sources, such as free-electron lasers [32], or appropriate techniques, such as femto-slicing [31], are employed. This, however, not only adds to the experimental complexity, but also narrows down the availability of this kind of methods. As has been outlined in section 3.5, a table-top and laser-based light source producing ultrafast as well as coherent soft x-ray pulses represents a viable alternative [38]. That is how the dynamic behavior of complex magnetic systems can be addressed element-selectively at a fundamental level, beyond precessional magnetization dynamics and far from the thermal equilibrium on the femtosecond timescale. To this end, the following section deals with employing soft x-ray pulses from higher-harmonic-generation to probe the dynamic response of thin permalloy films during an ultrafast optically driven demagnetization process.

The underlying physics of all ferromagnetic behavior is the cooperative interaction between individual atomic magnetic moments resulting in a macroscopic magnetization. The understanding of this cooperative phenomenon, commonly related to exchange coupling, and the resultant ferromagnetic phase is based on concepts of equilibrium thermodynamics. However, many technologically important applications, such as heat-assisted magnetic recording [109] and all optical switching [110], rely on the non-equilibrium, dynamic response of magnetic materials, compounds, or multilayer structures. This raises important questions regarding far-from-equilibrium dynamic behavior in complex magnetic systems.

Ever since the first experiment demonstrated that the quenching of the magnetization in metallic ferromagnets can be directly induced by an ultrashort optical pulse [21], the exact mechanism behind this process has been a controversial issue. Within the commonly accepted and phenomenologically derived three-temperature-model, it is assumed that an ultrafast dissipation channel for spin angular momentum is required for the demagnetization process to proceed at the order of a few hundred femtoseconds. Various approaches are currently debated to describe this fast spin-flip process, such as a Stoner excitation, an inelastic magnon scattering, an Elliott-Yafet-type of phonon scattering [15, 111], laser-induced spin flips [112, 113], spin-flip Coulomb scattering [114], or relativistic quantum electrodynamic processes [24]. Even spin-dependent

transport theory of laser-excited electrons seems to provide a considerable contribution [115, 116], which can explain the ultrafast demagnetization in a semi-classical model without having to resort to any angular momentum dissipation channel at all.

Since any theoretical explanation has to be substantiated by an experiment, the following investigation aims at exploring the basic question of whether magnetization dynamics of individual elements in an exchange-coupled magnetic alloy are truly identical. Addressing this question not only potentially uncovers whether site-specific individual magnetic moments must be considered to accurately describe ultrafast magnetization processes, but also explores the limitations of the employed technique including the exploited magneto-dichroic contrast mechanism. Here, permalloy is qualified to serve as a model system for various reasons. Due to a low coercivity, its magnetization reverses easily and therefore minimizes the effort to apply an appropriate magnetic field. The M absorption edges of Fe and Ni have proven to deliver a strong magnetic contrast and they are 12 eV apart facilitating their magneto-dichroic separation.

5.2.1 Sample Preparation and Characterization

To optimize the photon flux in a HHG based T-MOKE experiment, a permalloy grating was fabricated in a direct lift-off process employing optical lithography and thermal evaporation. First, a grating with a line width of $1\ \mu\text{m}$ and a periodicity of $2\ \mu\text{m}$ was patterned into photoresist covering a thermally oxidized Si $\langle 100 \rangle$ wafer via optical lithography. Prior to the deposition of 10 nm permalloy by thermal evaporation, a thin 3 nm Ta seed layer was sputtered onto the Si wafer to provide a strong $\langle 111 \rangle$ texture as well as good adhesion. Finally, the lift-off process was carried out in an acetone bath and the quality of the uncovered permalloy grating was inspected by a scanning electron microscope (SEM) and by an atomic force microscope (AFM), pictures of which are displayed in figure 5.8.

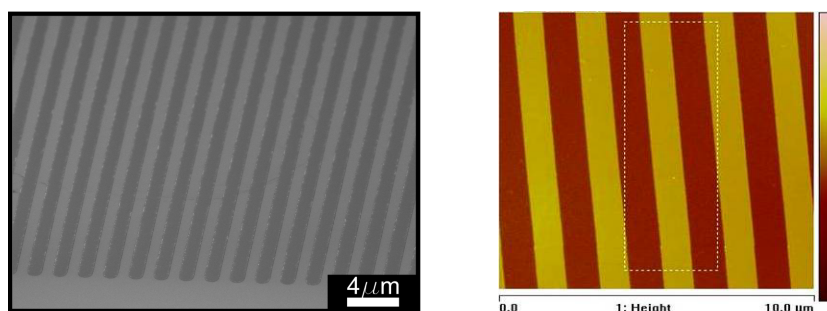


Figure 5.8: SEM (left) and AFM (right) pictures of the permalloy grating samples - fabricated and characterized by the group of Dr. Tom Silva at the NIST in Boulder, Colorado USA.

Additionally, the composition of this alloyed sample has been adjusted by intermixing permalloy with Cu in order to lower the Curie temperature T_C and to study its dynamics having shifted the critical point closer to room temperature. Various permalloy:Cu samples $((\text{Ni}_{80}\text{Fe}_{20})_x\text{Cu}_{1-x})$ were fabricated by co-sputtered deposition of permalloy ($\text{Ni}_{80}\text{Fe}_{20}$) and Cu from single targets onto the same substrate system with a 3 nm Ta seed layer at individually monitored deposition rates. Subsequently, a grating with the above-mentioned line width and density, serving as an etching mask, was patterned on top of the magnetic film via optical lithography. In an etching process, Ar ions with an energy of 300 eV have been used to remove the sputtered material, which was not covered by the patterned grating leaving behind a grating-like magnetic sample after finally removing the etching mask in an oxygen plasma.

All samples were first characterized by SQUID measurements with a magnetic field applied along the lines of the grating. Measurements of the switching behavior showed nearly rectangular hysteresis loops with a coercivity of about 2 mT for the pure permalloy sample, 0.5 mT for the permalloy:Cu samples and 8 mT for a Ni sample manufactured for reference purposes. The saturation magnetization of the Cu diluted permalloy samples was measured as function of the temperature from 10 K to 400 K, from which T_C was determined via extrapolation from the power law dependence of M vs. T , as indicated in the left graph of figure 5.9. In addition, a smooth and continuous change of T_C was measured as a function of the Cu doping for a full series of samples where the Cu content was varied from 60% to 40%, which is displayed in the right graph of figure 5.9. From this measurement, it can be concluded that all Cu doped permalloy samples consist of a complete intermixture of Fe, Ni, and Cu, without segregation and the permalloy sample with a Cu content of 40 % seems to be the most appropriate candidate for the following pump-probe experiment, since the Cu doping has shifted T_C of the sample close to the room temperature.

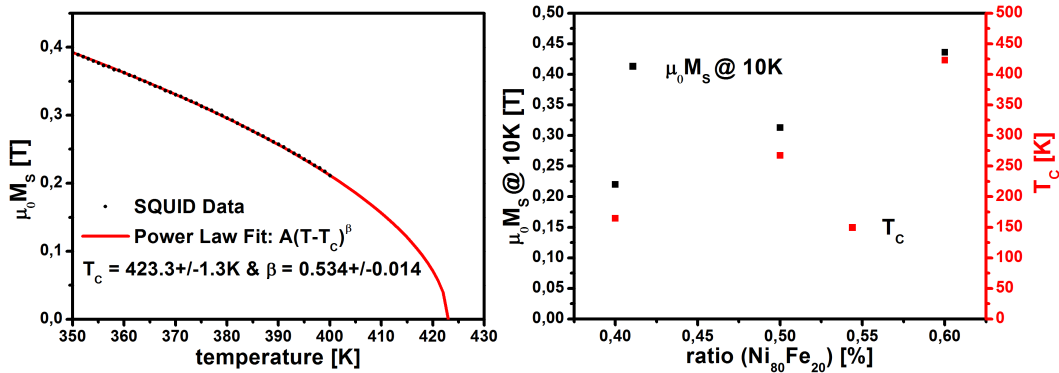
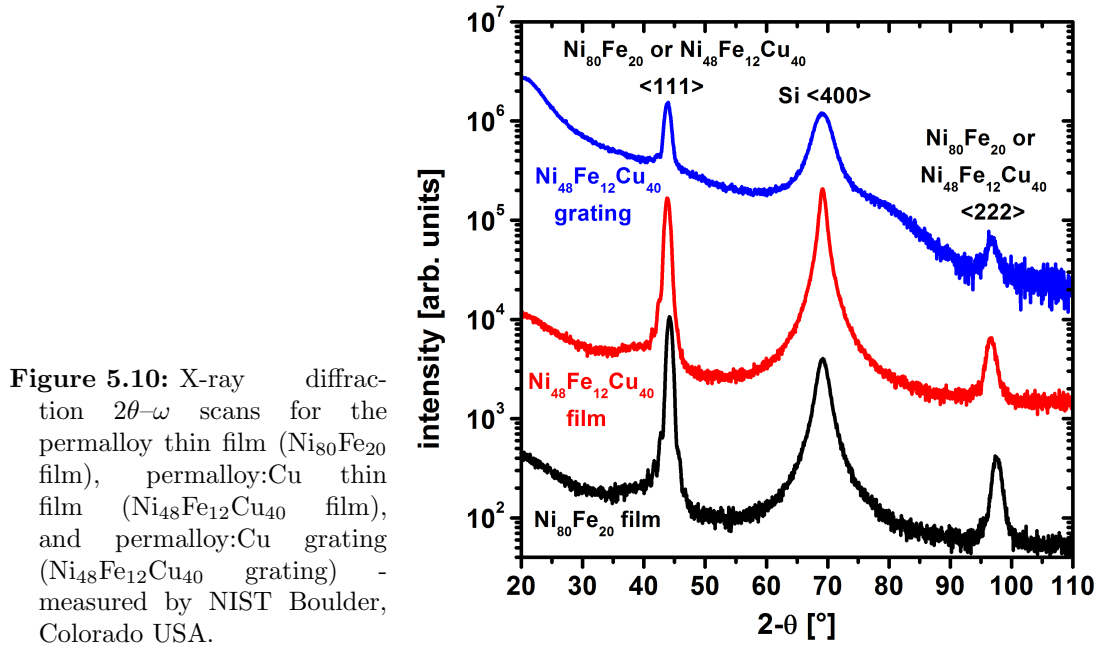


Figure 5.9: SQUID measurements of T_C and M_s - measured by NIST Boulder, Colorado USA.

Furthermore, x-ray diffraction (XRD) measurements were performed using a parallel beam configuration where a Cu K_α source was conditioned by a wavelength-specific x-ray mirror. The diffracted beam optics consisted of a parallel plate collimator, a Soller slit, and a graphite monochromator, whereas the reflected beam was detected by a proportional counter. The sample was mounted on a 4-circle goniometer with an instrumental resolution of 0.0001° in 2θ and ω . Figure 5.10 displays 2θ - ω scans of the plane permalloy and permalloy:Cu films as well as the permalloy:Cu grating sample chosen for the HHG experiment. Both the $\langle 111 \rangle$ and $\langle 222 \rangle$ peaks are present in all the spectra and they are consistent with a well $\langle 111 \rangle$ -textured face centered cubic (fcc) structure. Narrow peak widths of 3 – 4° at FWHM on the $\langle 111 \rangle$ peaks further point towards a high quality of the $\langle 111 \rangle$ -texture. No additional peaks corresponding to additional phases or segregation of species are present. The measured values of the lattice parameters are 0.3547 nm, 0.3573 nm, and 0.3572 nm for the permalloy thin film, permalloy:Cu thin film and permalloy:Cu grating, respectively. Moreover, if a linear relationship of the lattice constant is assumed, then the ideal lattice constant of a solid solution of 60% permalloy and 40% Cu is calculated to be 0.3574 nm (considering the measured lattice constant for permalloy above and a bulk value of 0.3615 nm for Cu). The good agreement between the measured and calculated lattice parameters in combination with the lack of any additional peaks in the XRD spectra, prove that the sample consists of a single fcc phase and the patterning process does not have a detrimental impact on the sample structure.



In order to provide an accurate determination of the magnetic homogeneity in the material, the ferromagnetic resonance (FMR) of the permalloy:Cu grating was measured with a broadband FMR spectrometer in a perpendicular applied field geometry [117, 118]. Figure 5.11 shows the FMR field and linewidth as a function of the microwave frequency for the $\text{Ni}_{48}\text{Fe}_{12}\text{Cu}_{40}$ grating sample. Most importantly, only a single FMR peak is observed, as expected for an alloy without segregation. By fitting the measured resonant fields with the following equation [106]:

$$H_0(f) = \frac{2\pi f}{|\gamma|\mu_0} - M_{eff} \quad \text{with} \quad \gamma = \frac{g\mu_B}{\hbar}, \quad (5.2)$$

a $\mu_0 M_{eff}$ of 0.295 T and a γ of 2.034 is obtained, with M_{eff} denoting the effective magnetization, γ being the gyromagnetic ratio, μ_0 corresponding to the vacuum permeability, f relating to the frequency of the applied microwave, μ_B representing the Bohr magneton, and g resembling the spectroscopic splitting factor. The value for $\mu_0 M_{eff}$ is lower than the value for the saturation magnetization $\mu_0 M_s$ measured by the SQUID, which can likely be ascribed to edge effects and anisotropy. The measured linewidth $\Delta H(f)$ is fitted with the phenomenological equation [119]:

$$\Delta H(f) = \Delta H_0 + \frac{4\pi\alpha}{\gamma\mu_0} f, \quad (5.3)$$

where ΔH_0 is the inhomogeneous linewidth broadening, generally related to locally varying magnetic properties of the sample and α denotes a dimensionless damping constant. The linear fit yields a $\mu_0 \Delta H_0$ of 5.2 mT and α of 0.0174. Both of these values are elevated as compared to permalloy films without alloying Cu [120], which is expected since T_C of the permalloy:Cu sample is relatively close to room temperature. The inhomogeneity of the perpendicular anisotropy quantified by ΔH_0 is indicative of a high quality thin film with a relatively small variation of its magnetic properties.

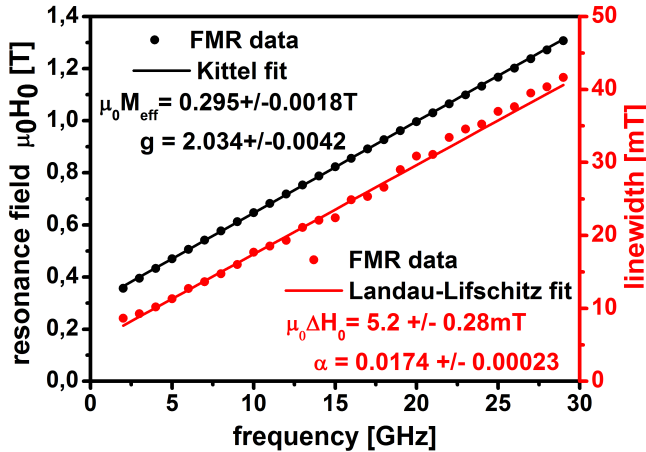


Figure 5.11: Ferromagnetic resonance field (black circles) and the corresponding linewidth (red circles) as a function of the applied microwave frequency for the $\text{Ni}_{48}\text{Fe}_{12}\text{Cu}_{40}$ grating sample. The black and red lines through the data are fits employed to extract the magnetic parameter $\mu_0 M_{eff}$, γ , $\mu_0 \Delta H_0$ and α - measured by NIST Boulder, Colorado USA.

The synchrotron provided the opportunity to take a closer look at the domain structure of the permalloy grating. By recording XMCD spectra of the total electron yield (TEY) across the L absorption edge of Fe, displayed in the left graph of figure 5.12, it was possible to obtain a magnetic contrast of up to 16 % for opposite incident photon helicities. This contrast mechanism has been exploited to take a PEEM picture of the magnetic configuration, which is displayed in the right graph of figure 5.12. The grey scale represents the orientation of the in-plane magnetization and the lines of the grating can be clearly seen, which seem to have no domains structure at all. Magnetically saturated bulk permalloy is known to provide an asymmetry of approximately 40% at the Fe L edge. In this experiment, however, an asymmetry of only 16 % has been observed, which can be explained by a partly oxidized surface indicated by the double peak in the TEY spectrum between 710 eV and 715 eV as well as the fact that the synchrotron light was not aligned exactly parallel to the lines. Thus, a high degree of magnetic homogeneity can be assumed, concluding that the grating is fully magnetized along the lines during a magnetic reversal process.

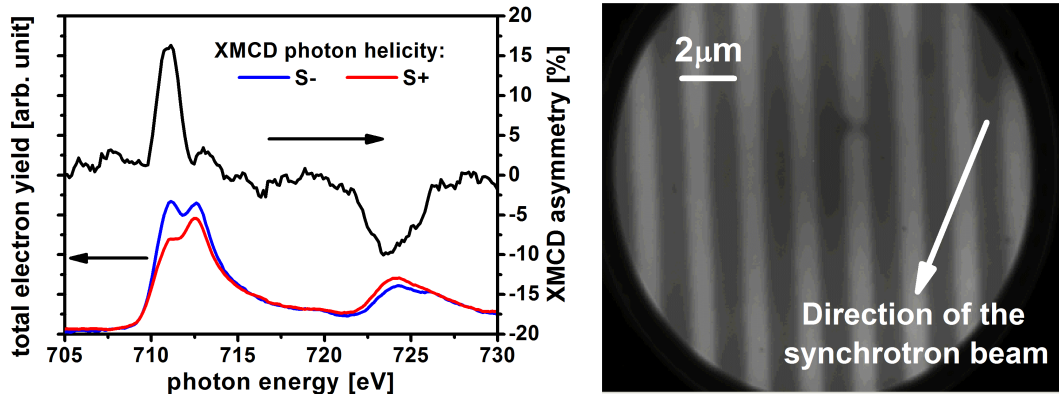


Figure 5.12: XMCD spectrum detecting the total electron yield (left) and PEEM image of the permalloy grating (right) taken at the Fe L absorption edge.

As has been outlined in section 3.5, the grating nature of the sample has been introduced to optimize the EUV photon flux in the light of a T-MOKE based pump-probe experiment employing a table-top soft x-ray source. Various techniques have been used to characterize the structural as well as magnetic properties of plane magnetic films and their corresponding grating samples. By summarizing and comparing the gathered information, it can be concluded that the magnetic homogeneity of both the grating and the plane samples closely resemble and that all alloy samples consist of a single, segregation-free fcc phase. Thus, all grating samples are assumed to exhibit the same magnetic behavior as plane thin films in the following analysis.

5.2.2 Demagnetization Dynamics of Nickel

After having thoroughly characterized the structural and magnetic properties of all samples, each of them was consecutively placed in the HHG setup introduced in section 3.6. To start with, a gold grating, manufactured in the same manner as the magnetic gratings, has been placed into the chamber in a 45° reflection geometry to align and characterize the setup. In the HHG experiment, intense *s*-polarized laser pulses from a Ti:sapphire amplifier, operating at a repetition rate of 2 kHz, are focused into a hollow fused-silica waveguide with a pulse energy of about 2 mJ. The waveguide is filled with neon gas, within which a broad range of harmonics, spanning 45 eV to about 72 eV, can be generated and phase-matched. The comb of harmonics emerging from the waveguide features a pulse length of less than 10 fs [121] and it is separated from the residual driving laser light using several 200 nm thick aluminum filters. This light is directed by a gold coated toroidal mirror onto the gold grating, where the HHG beam reaches a spot size of about $500\ \mu\text{m}$, as determined by simulations mentioned below. Behind the grating sample, the diffracted beam is focused onto a window-less x-ray CCD camera, a typical picture from which is displayed in figure 5.13.

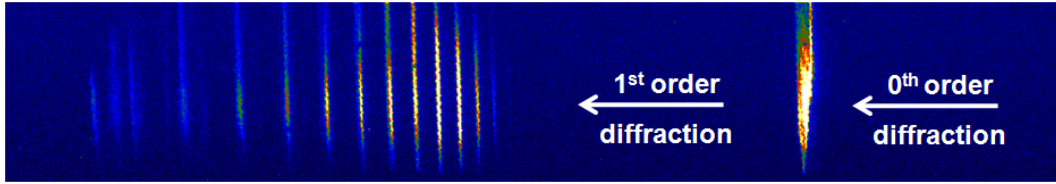


Figure 5.13: Intensity graph of the HHG beam diffracted off the gold grating and focused onto the CCD chip by means of a toroidal mirror placed in front of the grating.

Reading out the CCD camera the false color picture displayed above is obtained showing the 0^{th} order diffraction of the generated harmonics beam in specular reflection on the right side and the spectrally separated harmonics in first order reflection on the left side. It can be clearly seen that both the individual harmonics and the specular reflection are elongated along the vertical axis of the CCD chip. This can be understood by taking into account the curvatures of the employed toroid (long radius 3220 mm and short radius 90.5 mm), the incidence angle of the HHG beam (8°) and the approximate distances between the respective optical elements (source–toroid 600 mm, toroid–sample 300 mm, sample–CCD chip 300 mm). Simulations by means of RAY reveal (compare section 3.7) that the source, determined to be a point of $25\ \mu\text{m}$ at FWHM, cannot be imaged onto a circular spot due to inappropriately chosen parameters of the toroid. Nonetheless, by vertically binning the CCD chip it is possible to obtain a proper HHG spectrum, such as displayed in figure 5.14, in which the energy of the individual harmonics can be easily identified. As the sharp cut-off

at the absorption edge of the Al-filter is known to be located at 73 eV and the energy separation of the harmonics is about 3.16 eV corresponding to double the fundamental laser frequency centered at 780 nm, the energy scale can be calibrated via the grating equation [48] and a simple computer fitting algorithm (see appendix).

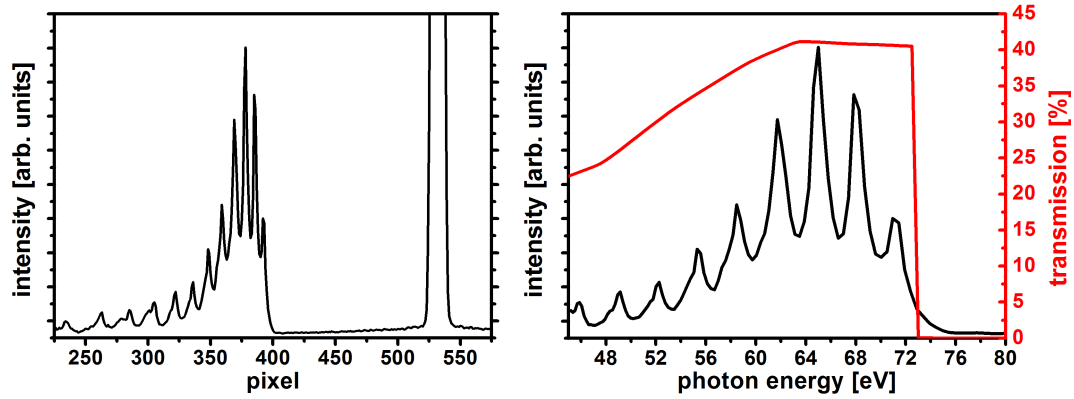


Figure 5.14: HHG spectrum of a laminar Au grating obtained by vertical binning of the x-ray CCD camera (left) and the corresponding calibrated HHG spectrum of the Au grating including the transmissivity of two 200 nm Al filters (right).

The left graph of figure 5.14 shows the recorded read out of the CCD camera in the full vertical binning mode displaying the detected photon intensity as a function of the horizontal pixel number. This graph can be clearly related to the CCD image shown in figure 5.13, thereby allowing for an identification of the specular reflection and the first order diffraction harmonics. The right graph in the same figure shows the detected photon intensity with a calibrated energy axis in the vicinity of the first diffraction order, which has been derived from the left graph exploiting the grating equation (see appendix). Moreover, the red curve marks the simulated transmissivity of two 200 nm thick Al-filters, each of which is assumed to have a 3 nm Al_2O_3 -layer on the front and back side [71]. It can be seen that in first approximation equally spaced harmonics qualitatively follow the absorption characteristics of the Al-filters cutting off the spectrum at 73 eV. The quantitative discrepancy can be addressed by taking into account the grating efficiency of the sample, which is displayed in the right graph of figure 5.15, rather than the reflectivity of the bulk material, which is displayed in the left graph of figure 5.15. Both properties have been simulated by the program REFLEC that comes as an add-on with the before-mentioned program RAY. As can be seen from this figure, the reflectivity of the Au bulk material is a monotonically decreasing function of the photon energy as opposed to the grating efficiency of the first diffraction order, which exhibits a modulation strongly influenced by the grating

groove depth. By comparing the grating efficiency of the Au grating having a groove depth of 32 nm with the calibrated HHG spectrum, it is striking that the extrema of the detected intensity and the calculated efficiency correspond. Thus, it can be concluded that the observed intensity distribution of the harmonics is dominated by the absorption characteristics of the Al-filters as well as the diffraction properties of the grating if an intensity plateau of harmonics is presumed (compare section 3.5).

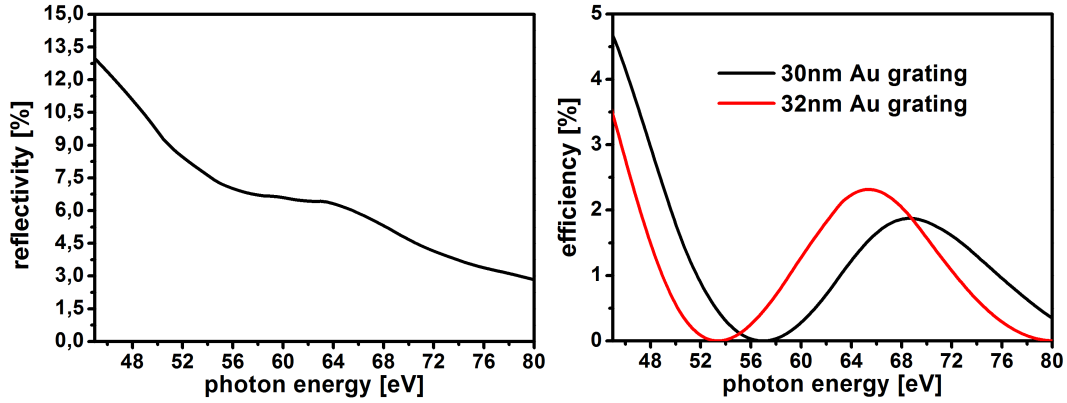


Figure 5.15: Simulated reflectivity of a Au mirror for s-polarized EUV light (left); Simulated grating efficiency of a Au grating with a groove depth of 30 nm and 32 nm, both of which feature the same grating line widths of $1\ \mu\text{m}$ and line densities of 500 lines/mm (right).

After having aligned and characterized the experimental setup, the Ni grating was inserted under the same optical geometry into the sample chamber. Since the generated EUV beam retains the polarization state of the driving laser field, a standard $\lambda/2$ waveplate was introduced right in front of capillary to comfortably change between s- and p-polarized radiation. Thus, the photon flux could be optimized with s-polarized photons prior to the magnetic T-MOKE experiment conducted with p-polarized light. Once a reasonable signal-to-noise ratio for a p-polarized EUV beam was obtained and the sharp cut-off of the Al-filters is unambiguously visible on the CCD camera, the magnetic field is reversed in an oscillatory manner by means of the Helmholtz coils sandwiching the sample. For each direction of the sample magnetization several spectra were recorded, averages of which are displayed in left graph of figure 5.16. A strong magnetic field dependent change in the reflected HHG spectrum is visible around 66 eV previously associated with the M absorption edge of Ni. This magneto-dichroic signal vanishes if the light polarization is rotated to the s-state. The right graph of figure 5.16 shows the magnetic asymmetry derived from the HHG spectra. Here, a bipolar peak structure with an amplitude of about 30% can be identified and matched with previously recorded asymmetry spectra taken at the synchrotron (compare figure 4.2).

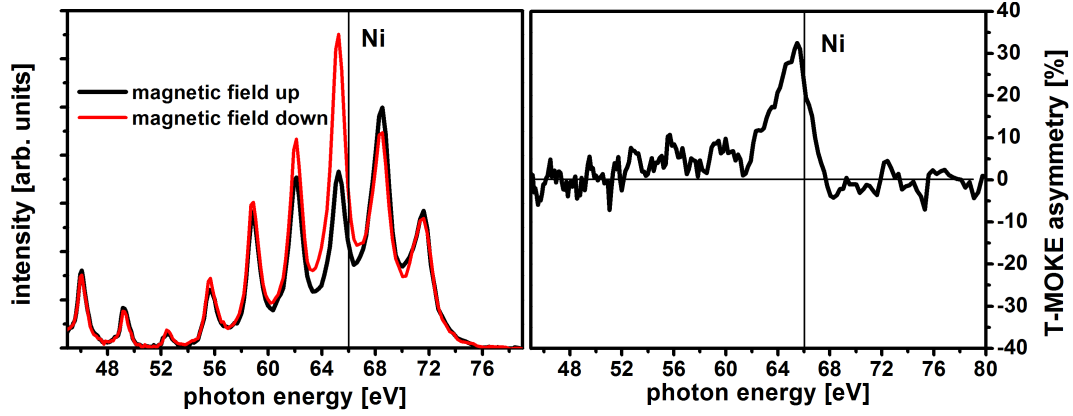


Figure 5.16: HHG spectra for p-polarized light and opposite sample magnetizations (left); Corresponding magnetic asymmetry showing bipolar peak structure around 66 eV (right).

As soon as a magnetic contrast is confirmed, the pump-probe experiment can be initiated by the determination of $\Delta t = 0$, the temporal overlap of the pump and probe pulse trains. To this end, the sample holder is equipped with a $100\ \mu\text{m}$ thick β -bariumborat crystal (BBO), which is placed right next to the sample in a transmission geometry. The sample holder is mounted on a translation manipulator allowing for interchanging the magnetic grating and the BBO without having to break the vacuum. In order to measure $\Delta t = 0$, the Al-filters behind the capillary are removed, the gas inlets are closed and the BBO is subjected to the appropriately attenuated fundamental laser light of the probe beam. In addition, temporally shifted pump pulses are spatially overlapped with the probe light on the crystal. Thus, by moving the delay stage and searching for the frequency doubled autocorrelation signal, located on the bisecting line of the angle enclosed by the pump and the probe beam, the temporal overlap of the pump and probe pulses can be determined with an accuracy in the femtosecond range. In this pump-probe geometry, the probe beam with a diameter r of approximately 0.5 mm overlaps with the pump beam at a relative angle ϑ of about 1.5° introducing a time smear of $t_{res} \approx r/c \sin\vartheta = 55\text{ fs}$, with c denoting the speed of light in vacuum. It is only this smear in combination with the pulse length of the pump light (30 fs), which finally determines the temporal resolution limit of this pump-probe experiment, as the generated harmonics have a pulse length below 10 fs [121] and the pump-probe pulse trains are inherently synchronized due to the coherent HHG process.

Once $\Delta t = 0$ has been pinpointed, the setup can be returned into the original state for the laser excited EUV experiment. The nickel is transiently demagnetized by focusing the infrared pump-pulse onto the sample, to strongly excite the electronic system with a pump fluence of approximately 2 mJ/cm^2 . The magnetic asymmetry

is then extracted as function of the delay between laser pump and HHG probe pulses in the vicinity of the previously determined pump-probe overlap $\Delta t = 0$. Figure 5.17 shows the asymmetry for both a negative and a positive pump-probe delay in the left graph, whereas the temporal evolution of the magnetic asymmetry extracted from the harmonic at about 65 eV is depicted in the right graph of the the same figure.

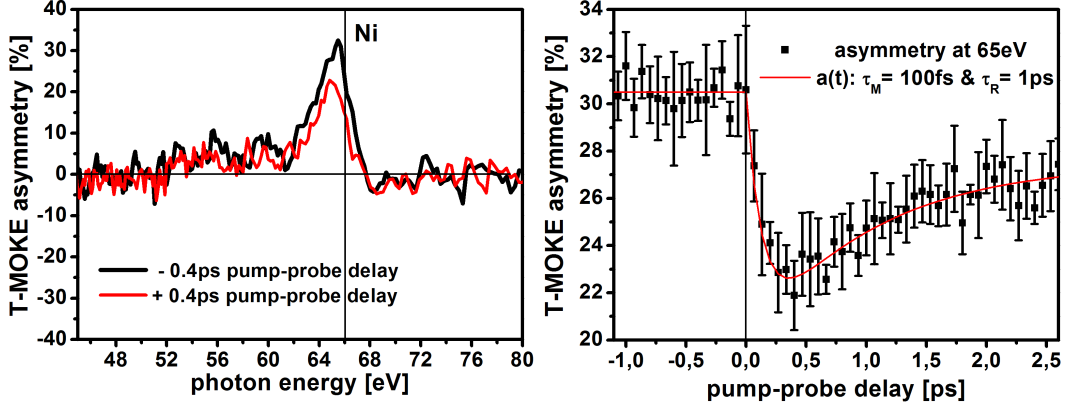


Figure 5.17: Magnetic asymmetry for a single negative and positive pump-probe delay (left); Temporal evolution of the magnetic asymmetry in the vicinity of 65 eV(right).

As can be seen from the left graph of this figure, there is a pronounced decrease in the maximum amplitude of the asymmetry as a function of the pump-probe delay changing from about 31% for a negative pump-probe delay to approximately 22% for a delay of 0.4 ps at a photon energy of 65 eV. A comparison of the HHG spectra and the asymmetry reveal that the largest magneto-dichroic signal as well as its change coincide with a single harmonic. Therefore, an algorithm has been developed and programmed (see appendix), which locates the maxima of the harmonics and calculates as well as integrates the magnetic asymmetry in a given environment around the peak position. Subsequently, several traces can be averaged and error bars are determined, the result of which is plotted against the pump-probe delay, such as displayed in the right graph of figure 5.17. It can be seen from this graph that the asymmetry $a(t)$ drops sharply at the pump-probe delay $\Delta t = 0$ from 31% to about 22% within a few hundred femtoseconds and finally, $a(t)$ starts to recover on the picosecond time scale. In order to quantify this behavior, the following phenomenological fit function has been exploited presuming a simplified two temperature model [23, 122]:

$$a(t) = \theta(t)[A(1 - e^{-t/\tau_M})e^{-t/\tau_R} + B(1 - e^{-t/\tau_R})] \approx \theta(t) A(1 - e^{-t/\tau_M})e^{-t/\tau_R}, \quad (5.4)$$

with $\theta(t)$ denoting a Heaviside function, τ_M representing the demagnetization time, τ_R considering the recovery time and A as well as B being exponential amplitudes with $B \ll A$. As can be seen from the red curve in the right graph of figure 5.17, which reproduces the function above with a τ_M of 100 fs and a τ_R of 1 ps, the measured data is very well described by this equation. Apart from slight shifts of $\Delta t = 0$, which have been corrected and lie within the accuracy of the alignment procedure, the demagnetization time can be brought into agreement with previous findings [15].

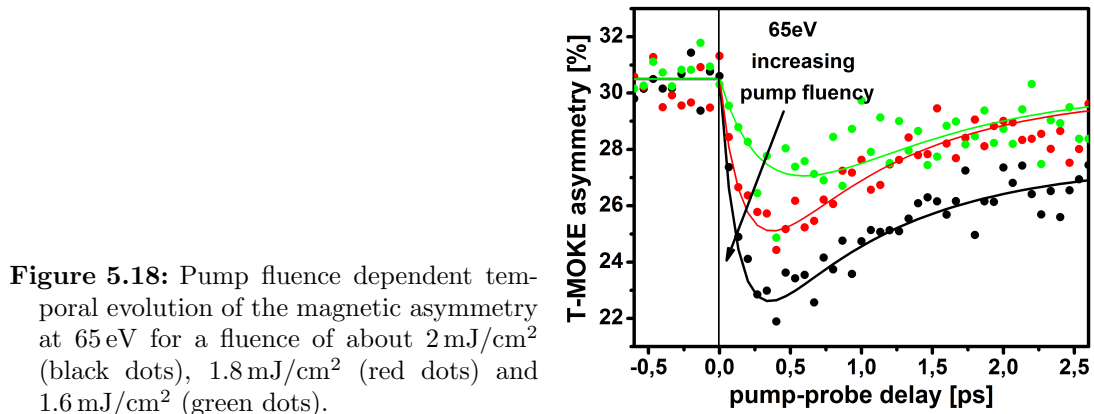


Figure 5.18: Pump fluence dependent temporal evolution of the magnetic asymmetry at 65 eV for a fluence of about 2 mJ/cm² (black dots), 1.8 mJ/cm² (red dots) and 1.6 mJ/cm² (green dots).

By changing the intensity of the pump pulse, a distinct fluence dependent variation of the time-resolved asymmetry is observed. Figure 5.18 displays the temporal evolution of the magnetic asymmetry for a pump fluence of about 2 mJ/cm² (black dots), 1.8 mJ/cm² (red dots) and 1.6 mJ/cm² (green dots), whereas the lines in the corresponding colors are fits based on equation 5.4 resulting in a τ_M of 95 fs \pm 49 fs, 105 fs \pm 78 fs and 156 fs \pm 125 fs, respectively. For the sake of illustration the error bars have been omitted. A simple comparison of these numbers with results obtained by time-resolved MOKE demagnetization experiments of thin Ni films in the visible range reveal that the trend of decreasing demagnetization times accompanied by decreasing pump fluencies is opposed to previous findings and predictions [15].

However, this claim cannot be substantiated due to a poor signal-to-noise ratio and a high uncertainty in the determined demagnetization time constants. Seemingly, the fluence dependent contradiction points towards the question of whether and how an ultrafast laser induced quenching of the magnetization is reflected in the recorded T-MOKE signal in the extreme ultraviolet range. But without supporting simulations of the underlying contrast mechanism and appropriate experimental statistics this question reaches beyond the scope of this thesis. From this experiment it can be concluded though, that the observed demagnetization of the nickel sample is sufficiently mirrored in the EUV as compared to experiments in the visible range, thereby laying the basis for element-specific investigations.

5.2.3 Demagnetization Dynamics of Permalloy

In order to address the question whether any element-specific differences can be observed on the ultrafast femtosecond timescale, the permalloy grating has been placed into the sample chamber in a right angle T-MOKE geometry thereafter. Similarly, the photon flux has been optimized, the position of $\Delta t = 0$ has been checked and the magnetic asymmetry has been measured. Figure 5.19 shows the HHG spectra of the permalloy grating for two opposite sample magnetizations in the left graph, whereas the corresponding asymmetry is shown as a black curve in the right graph. The energy axis was not only calibrated via the grating equation, but also by means of previously recorded T-MOKE asymmetry spectra of a plane permalloy film measured at BESSY.

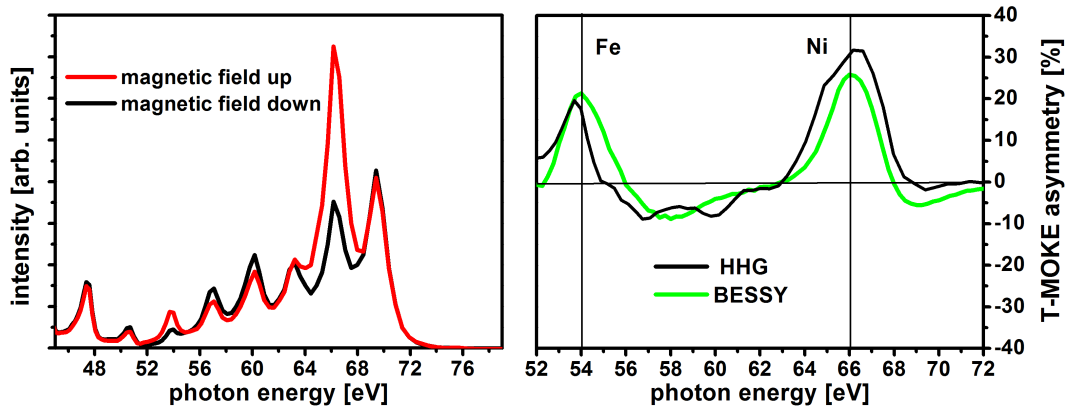


Figure 5.19: HHG spectra of a permalloy grating for opposite sample magnetizations (left); Magnetic asymmetry derived from HHG spectra (black) and from spectra taken at BESSY (green), both of which show bipolar peak structures at the Fe and Ni M edges (right).

The shown asymmetry measured with the HHG source exhibits two pronounced bipolar peak structures with amplitudes of about 20% and 30% located around 54 eV and 66 eV, respectively, which have been previously associated with the M absorption edges of Fe and Ni. A comparison with the asymmetry spectra taken at the synchrotron (green curve - compare figure 4.10) reveals a good agreement. It is interesting to note that the HHG derived asymmetry features a modulation, whose period corresponds to the spacing of the harmonics. The discontinuous spectral emittance of the table-top source explains why the asymmetry is unexpectedly interrupted, such as at around 54 eV, in comparison to the data taken at the synchrotron. Nonetheless, the resulting magnetic signal is sufficiently strong and the frequency spacing of the harmonics comb is small enough to extract element-specific information in a time-resolved experiment.

Following the pump-probe experiment on the nickel grating, the electron system of the permalloy grating has been excited by pump pulses with a fluence of 2 mJ/cm^2 . The temporal response of the system was probed in an oscillatory magnetic field with a comb of harmonics by delaying the pump with respect to the probe pulses and evaluating the asymmetry of the harmonics. The result of this experiment is shown in figure 5.20, in which the normalized asymmetry extracted from six harmonics is plotted as a function of the pump-probe delay.

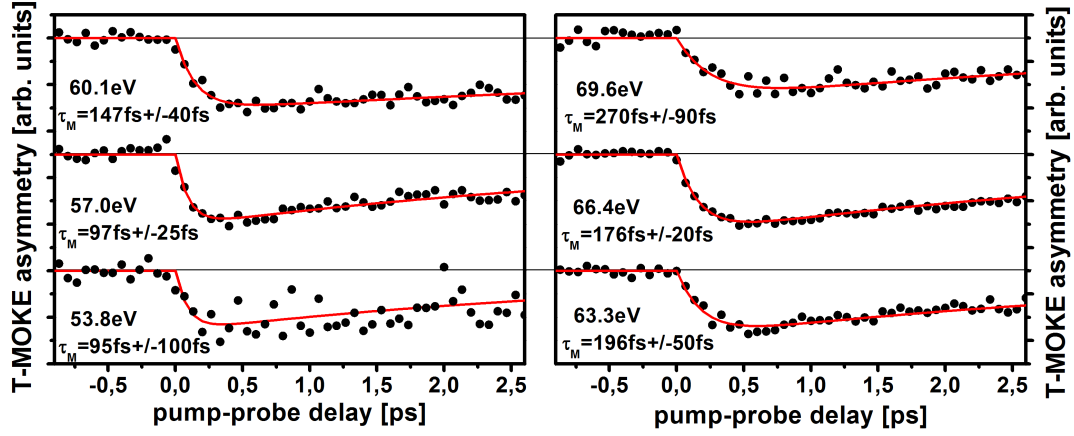


Figure 5.20: Time-resolved magnetic asymmetry of the permalloy grating for a pump fluence of 2 mJ/cm^2 extracted from various harmonics.

All traces basically show a similar behavior by starting to drop at $\Delta t = 0$ within the first hundred femtoseconds to a minimum of about 70% as compared to the initial value for negative delays and finally the asymmetry enters the recovery on the picosecond timescale. The main difference of the displayed traces is related to their signal-to-noise ratios and the time constants for the demagnetization and recovery period. To quantify this observation, all traces have been fitted by equation 5.4 and the corresponding fits (red curves) have been inserted into the graph along with the determined demagnetization times. It is interesting to note, that a clear trend of the demagnetization behavior crystallizes, as the time constants start at about 100 fs at the lower energy region of the spectrum associated with the Fe edge and constantly increases to more than 200 fs at the higher end of the energy spectrum related to the Ni edge. By having a closer look at harmonics at the respective absorption edges (53.8 eV and 57.0 eV for Fe – 63.3 eV and 66.4 eV for Ni), it can be clearly seen that the demagnetization time constants differ almost by a factor of two. This observation is supported by considering two harmonics located at the Fe edge (57.0 eV) and at the Ni edge (66.4 eV) with the highest signal-to-noise ratios resulting in small error

bars of the extracted time constants, which are determined to be $97 \text{ fs} \pm 25 \text{ fs}$ and $176 \text{ fs} \pm 20 \text{ fs}$, respectively. This data strongly suggests that magnetization dynamics in an exchange coupled compound material decouples under extreme non-equilibrium conditions.

The coupling of the magnetic moments in a ferromagnetic alloy, such as permalloy, is mediated by a large exchange interaction, as indicated by a high Curie temperature T_C of 850 K. Therefore, different demagnetization times for Fe and Ni in permalloy necessarily require a significant weakening of the exchange interaction between neighboring magnetic moments. Motivated by this fundamental understanding of ferromagnetic order, the experiment was repeated with the Cu doped permalloy sample, as the adding of Cu results in the continuous reduction of T_C . Prior to the pump-probe experiment, a static characterization of the grating sample was performed in the EUV.

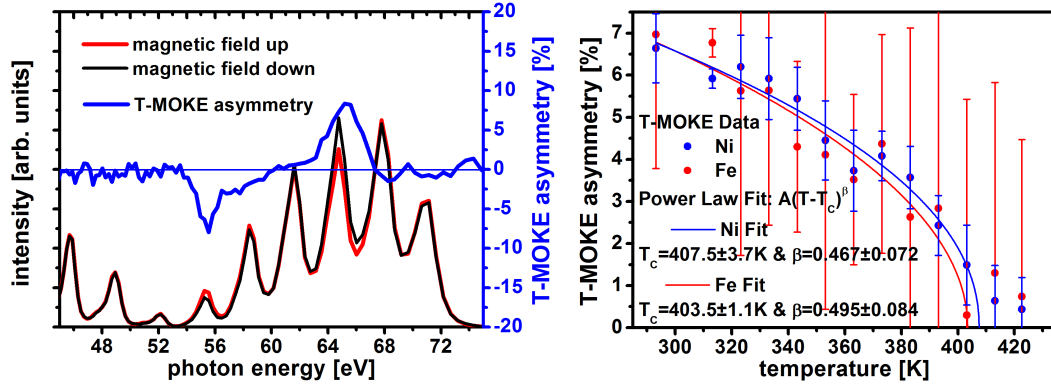


Figure 5.21: HHG spectra of the Cu:permalloy grating for opposite sample magnetizations and magnetic asymmetry (left); Magnetic asymmetry as a function of the sample temperature extracted from two harmonics 55.3 eV and 64.8 eV representing Fe and Ni (right).

As can be seen from the left graph of figure 5.21, the recorded asymmetry of the permalloy:Cu sample shows two pronounced extrema with an amplitude of $\pm 7\%$ located at a photon energy of approximately 55 eV and 66 eV, respectively. In contrast to the pure permalloy, where the asymmetry was found to be as high as 30%, the extrema are also shifted by about 1.5 eV on the energy axis calibrated via the grating equation. Both the differing amplitude and the shifted energy position can be related to a much smaller saturation magnetization of 0.4 T as compared to 1 T for the pure permalloy sample as well as the varying sample thickness. Since the extrema of the asymmetry coincide very well with two harmonics, each of which is approximately located at a respective absorption edge, their change in amplitude is chosen to represent the elements Fe and Ni in the following.

The asymmetry was also measured as a function of the sample temperature up to 425 K, the result of which is displayed in the right graph of figure 5.21. It can be seen that the absolute values of the magneto-dichroic signal representing Fe and Ni show the same temperature dependence and both asymmetries gradually reduce to zero near T_C . In this measurement, the sample is magnetized to saturation by a magnetic field of approximately ± 4 mT, which creates a smearing of the asymmetry near T_C , because of a large magnetic susceptibility related to a paramagnetic contribution close to the critical point. A fit by the power law $A(T - T_C)^\beta$ results in a Curie temperature of $403.5 \text{ K} \pm 1.1 \text{ K}$ for Fe and $407.5 \text{ K} \pm 3.5 \text{ K}$ for Ni, with the critical exponent β of a little less than 0.5 – the value predicted by the mean-field theory [62, 123]. The fact that both the Fe and the Ni signals show the same T_C within the error bars of the power law fit (and not 1043 K for bulk Fe and 631 K for bulk Ni) implies that the permalloy:Cu grating consists of a single-phase alloy without any segregation between the Fe and Ni. The value of Curie temperature is 5% less than the value measured by the SQUID, because of expected variations in the sputter deposition rate from different sample fabrications.

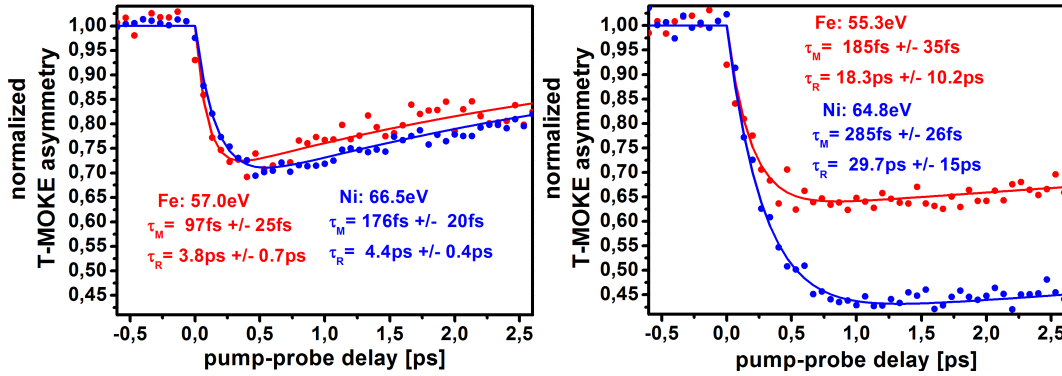


Figure 5.22: Time-resolved magnetic asymmetry of the permalloy (left) and the Cu doped permalloy (right) gratings for a pump fluence of 2 mJ/cm^2 extracted from various harmonics.

Figure 5.22 compares the element-selective and time-resolved T-MOKE signal of the pure permalloy sample on the left side with the recorded signal of the permalloy:Cu sample on the right side. Both curve pairs exhibit a pronounced drop within the first few hundred femtoseconds and show a recovery in the picosecond range. A distinct difference in the drop amplitude, the demagnetization time and recovery time can be clearly identified between the two sample systems. In the case of permalloy the asymmetry related to the elements Fe and Ni drop by about the

same 30%, whereas in the case of the Cu doped permalloy the asymmetry at the Fe edge drops by 35% and the asymmetry at the Ni edge by more than 50%. Even though it has not been proven that a drop of the asymmetry can be directly related to a quenching of the magnetization, it is interesting to note that a reduction of the Curie temperature is accompanied by a more pronounced reduction of the minimum of the time-resolved asymmetry signal. This result agrees well with previous findings presuming an Elliott-Yafet type spin-flip process involving impurities and phonons in the demagnetization process [15]. In addition, the considerable difference in the drop of the asymmetry associated with the respective elements suggests an element-specific demagnetization process, which varies with the alloy composition. Thereby, the hypothesis can be sustained that a rather decoupled behavior of Fe and Ni in the out-of-equilibrium state of the alloy is related to a weakening of the exchange coupling and by shifting the T_C of the compound close to room temperature this effect is further enhanced.

	Ni ₈₀ Fe ₂₀ τ_M	Ni ₈₀ Fe ₂₀ τ_R	Ni ₄₈ Fe ₁₂ Cu ₄₀ τ_M	Ni ₄₈ Fe ₁₂ Cu ₄₀ τ_R
Fe - M edge	97 fs \pm 25 fs	3.8 ps \pm 0.7 ps	185 fs \pm 35 fs	18 ps \pm 10 ps
Ni - M edge	176 fs \pm 20 fs	4.4 ps \pm 0.4 ps	285 fs \pm 26 fs	30 ps \pm 15 ps

Table 5.1: Fitted demagnetization τ_M and recovery τ_R time constants for the permalloy and the permalloy:Cu gratings extracted from the temporal evolution of harmonics located at the M absorption edge of Fe and Ni after a laser induced excitation with a fluence of 2 mJ/cm².

By fitting equation 5.4 to the recorded data of the permalloy:Cu sample the time constants for the demagnetization are determined to be 185 fs \pm 35 fs and 285 fs \pm 26 fs, whereas the recovery time constants are 18 ps \pm 10 ps and 30 ps \pm 15 ps for Fe and Ni, respectively. By comparing these values with the previously extracted time constants of the pure permalloy sample, all of which are also summarized in the table above, it can be noticed that both demagnetization and recovery time constants increase in anticipation of a decreasing T_C [15]. Interestingly, a difference in the demagnetization time τ_M can be observed for Fe and Ni, which increases from about 80 fs for the permalloy system to approximately 100 fs for the permalloy:Cu system. This observed tendency strengthens the advanced hypothesis of elemental demagnetization dynamics, which changes with the alloy composition; especially so, as a segregation of the constituent elements into distinct crystalline phases within the sample can be excluded on the basis of a thorough static characterization in the EUV in combination with FMR, SQUID and XRD techniques.

As has been shown in previous theoretical work [124], a different behavior is predicted for the two atomic species Fe and Ni in permalloy alloyed with Cu. The Cu

introduces small deviations from a collinear alignment of the magnetic moments, which is more pronounced for Ni than for Fe. Even in the case of pure permalloy, a similar behavior was also theoretically predicted [125]. These calculations give a first indication that the static orientation of the Fe and Ni magnetic moments can be non-collinear in such alloys. However, these calculations do not address the question of whether the constituent atomic species can display different dynamical behavior, where the exchange interaction must be sufficiently weakened so that the transient torque, incurred by having the two materials in different magnetic states over time, is small compared to the other torques acting on the spins during the optical pump and the subsequent demagnetization process. In order for the atomic moments to react differently to the optical pump, the magnetic system must be in a regime where every atom and its local magnetic moment reacts independently to the pump-induced excitation. Furthermore, the microscopic processes associated with demagnetization at the atomic sites must depend on the particular species in question, even though the equilibrium magnetization state for a transition metal alloy is a function of the hybridized sp-d band found in such materials [126]. Otherwise, there would be no reason to expect Fe and Ni to demagnetize at different rates, even if they are no longer coupled by the exchange interaction.

The pump-probe experiment starts with the ferromagnetic state at room temperature. Once the infrared pump pulse excites the sample, the electrons near the Fermi energy are placed in highly excited states, at which point electron-electron, electron-phonon, and electron-impurity scattering processes start to act on the electronic system on a femtosecond timescale. Elliott-Yafet type spin-flip processes based on electron-phonon and electron-impurity scattering is one possible mechanism, that can reduce the spin polarization of the excited electronic states over time. Electron-phonon scattering processes transfer thermal energy to the crystal lattice on the picosecond timescale, heating the sample by about 20 K in 100 fs [15, 21]. Thus, this thermal heating process is not fast and strong enough to drive the system above T_C on timescales consistent with the data shown in figure 5.22.

A possible explanation that is consistent with the ultrafast timescale of this observation must involve an optically induced, transient non-equilibrium electronic state that apparently reduces the exchange interaction [127]. The experimental data provide an extremely fast upper limit of only 100 fs for the timescale of such a reduction of the exchange coupling, based on the observation of distinct demagnetization dynamics for Fe and Ni in the Cu doped permalloy grating. It is therefore concluded that the decoupling must be mediated by the highly excited hot-electron gas created by the pump pulse. The absorption of the pump pulse initially creates a transient high density of free charge carriers. These free carriers induce additional Coulomb [128] and exchange screening [129] on a timescale given by the inverse frequency of the plasmon oscillation period [130], referred to as the plasmon screening time τ_{Pl} . This is consistent with the shown experimental data, since in metals τ_{Pl} is

certainly faster than the extracted upper limit of 100 fs for the breakdown of the exchange interaction. This hypothesis is further supported by the fact that at times longer than 1 ps, when the non-equilibrium hot-electron gas has cooled and is in thermal equilibrium with the phonon system [15], the dynamical behavior for Fe and Ni is assumed to be identical again. At long times, the strong exchange coupling is restored, and Fe and Ni show a similar recovery, which is reflected by the time constants of the corresponding relaxation processes within the error bars.

5.2.4 Summary and Conclusion

In summary, it has been demonstrated that ultrafast and coherent EUV light originating from a table-top soft x-ray source can be employed to probe magnetization dynamics element-selectively attaining the fastest time resolution measured to date using any light source. Exploiting the resonant T-MOKE in a right angle reflection geometry, a high magnetic contrast of up to 20% and 30% was obtained near the M absorption edges of Fe (54 eV) and Ni (66 eV) in a permalloy sample, respectively. A short optical pump pulse is used to destroy the magnetic alignment, and inherently synchronized HHG EUV probe light allows for measurements of ultrafast demagnetization dynamics with a temporal resolution of 55 fs in a pump-probe experiment. It is found that the demagnetization times for the elements Fe and Ni differ significantly, despite their strong exchange coupling in the thermodynamic equilibrium. This difference is assumed to be ascribed to a breakdown of exchange interaction on the femtosecond timescale, a process that seems to be further enhanced by alloying permalloy with Cu.

This experiment shows that even in the strongly exchange coupled transition metal alloys, a diversity of demagnetization dynamics of the individual elements Fe and Ni can be observed. This fact has significant impact on the dynamical magnetic behavior for all types of exchange-coupled materials, including both alloys and multilayer structures. Although a detailed theory is still developing, there is evidence that this exceptionally fast decoupling must be induced by the photo excited hot-electron gas, and can be explained by a breakdown of the exchange interaction. Moreover, these findings are very likely a general result present in all ultrafast demagnetization dynamics processes. Most importantly, this data suggests that the local spin environment at the atomic level plays a vital role in the dynamic response of magnetic materials, and must be included for a complete understanding of the microscopic physics underlying ultrafast demagnetization processes. This work opens up the possibility of element-selectively probing magnetization dynamics and imaging domain structure on ultrafast femtosecond-to-attosecond time scales with a nanometer resolution in a laboratory environment.

Conclusion and Outlook

The objective of this thesis was to explore the potential of the extreme ultraviolet region to serve as an element-selective and magnetic contrast mechanism for magneto-optical investigations. Within this context, this work focused on alloy and multilayer model systems based on iron, cobalt and nickel due to their high relevance for both fundamental research and technology. Four reflectivity experiments exploiting the T-MOKE have been performed by tuning the photon energy to the M absorption edges of the respective 3d transition ferromagnets. By exploiting the temporal structure of a synchrotron as well as a laser based soft x-ray light source, not only element-selective but also time-resolved information about the magnetic system under investigation was obtained. The first two result sections studied the potential for layer-selective measurements of the magnetization in multilayer systems, whereas the final two sections dealt with results obtained in pump-probe experiments in the EUV.

In the first experiment spatially separated but homogeneous and ferromagnetically coupled layers in a wedged $\text{Co}(5\text{ nm})/\text{Si}(1\text{-}4\text{ nm})/\text{Ni}(8\text{ nm})/\text{Fe}(2\text{ nm})$ multilayer are studied. Measurements and supporting simulations of the magneto-optical response as a function of the photon energy, the incidence angle and the Si spacer thickness explore the character of the magneto-dichroic signal in the EUV and its potential for layer-selective investigations. In this system a magnetic contrast as high as 80 % can be obtained and the recorded magneto-optical loops of the hysteresis prove that the switching of single layers can indeed be measured layer-selectively.

The second experiment is concerned with magneto-optical investigations of a single multilayer containing two anti-ferromagnetically coupled heterogeneous ferromagnetic layers. Here, the magneto-optical response of the system consisting of a bottom $\text{Co}_{40}\text{Fe}_{60}$ layer (10 nm) and a top $\text{Ni}_{80}\text{Fe}_{20}$ layer (5 nm) separated by a thin layer of Cr (0.6 nm) is compared with the response of the respective individual alloys. The hysteretic switching behavior of the multilayer is analyzed in the EUV with regard to layer-selectivity by referring to the absolute magnetic moment derived from measurements by a SQUID magnetometer. The magnetic contrast reaches 30 % and the individual switching of layers in the multilayer can be observed.

In conclusion, the first two experiments show that the magnetic contrast at the M absorption edges is much larger than in the visible or soft x-ray range. However, due to the energetic proximity of the M absorption edges of Fe, Co and Ni special care has to be taken to attain a layer-selective response from a complex multilayer system. This is accomplished by recording hysteresis loops for various incidence angles and photon energies and by characterizing the role played by magneto-optical interferences and crosstalk with regard to a layer-selective response of the multilayer stacks. This consequently facilitated to understand the switching behavior of individually selected layers as a function of the interlayer coupling, whose strength expectedly decreases with an increasing spacer thickness.

In the third experiment, precessional dynamics of the magnetization in thin permalloy film patterned to form a coplanar waveguide is induced by ultrashort laser pulses. The resulting oscillatory response is probed by synchronized EUV pulses originating from a synchrotron tuned to the M absorption edge of Ni. It is found that the induced magnetic precession closely follows the ferromagnetic resonance and a strong resonantly enhanced energy conversion among various excited frequency modes is present. These results in combination with reference measurements in the visible range not only prove the feasibility, but also explore the limitations of this pump-probe approach. Even though a magnetic contrast as large as 20 % is obtained in static EUV experiments, only relatively weak oscillation amplitudes are observed in relation to the approach at visible wavelengths. This is ascribed to the experiment approaching and exceeding the time resolution limit of the synchrotron given by the length of a EUV pulse at the order of 100 ps. Considering the complexity of the setup and a limited access to the required infrastructure, a table-top soft x-ray source producing coherent femtosecond EUV pulses in a laboratory environment represents a viable alternative.

The fourth experiment deals with the ultrafast demagnetization of a permalloy grating, which is optically driven by intense laser pulses. The response is probed by inherently synchronized EUV pulses generated by a table-top soft x-ray source tuned to the M absorption edges of Fe and Ni. It is shown that a large magnetic contrast of up to 30% can be exploited to element-selectively probe the evolution of the magnetic system with an unprecedented temporal resolution of 55 fs. It is found that the demagnetization times of the recorded signal associated with the elements Fe and Ni differ significantly, despite their strong exchange coupling in the thermodynamic equilibrium. This difference can be ascribed to a breakdown of exchange interaction on the femtosecond timescale, a process that is further enhanced by alloying permalloy with Cu. These results suggest that the local spin environment at the atomic level plays a vital role in the dynamic response of magnetic materials, and must be included for a complete understanding of the microscopic physics underlying ultrafast demagnetization processes.

These experiments show the feasibility of pump-probe experiments on magnetic model systems in the EUV. They pave the way to element-selectively probe magnetization dynamics on ultrafast femtosecond-to-attosecond time scales in a laboratory environment. Moreover, it is promising to combine this approach with imaging capabilities benefiting from a spatial resolution on the nanometer scale, if current methods are extended into the realm of magnetism [42]. Thus, a single technique is within reach to element-selectively address magnetization at fundamental scales in space and time.

Beside the gained insights, first steps have been taken to address questions raised in the wake of the conducted experiments. The most fundamental issue is related to the representation of the sample magnetization in the recorded magneto-optical signal. The second chapter indicated how the magnetization can be connected with the Kerr effect via the Fresnel reflection coefficients and the dielectric tensor. Since this complex quantum mechanical interaction of light and matter can be accounted for by utilizing a quantum mechanical description of phenomenological response functions, *ab-initio* calculations of the electronic band structure can deliver the missing link. Figure 6.1 displays preliminary density-functional theory calculations of the response at the Ni M absorption edge of a mono-crystalline Ni film along the $\langle 100 \rangle$ axis performed by the group of Prof. Peter Oppeneer from the university of Uppsala in Sweden (compare with [70]). The left graph of this figure shows the density of states (DOS) for spin-up and spin-down electrons as a function of the photon energy, whereas the right graph of the same figure displays accordingly derived dielectric tensor elements related to the Kerr effect. Thus, the magneto-optical response can be deduced and directly linked to the sample magnetization. In future work, it is intended to include the influence of ultrafast laser excitations and to extend theory to pump-probe experiments.

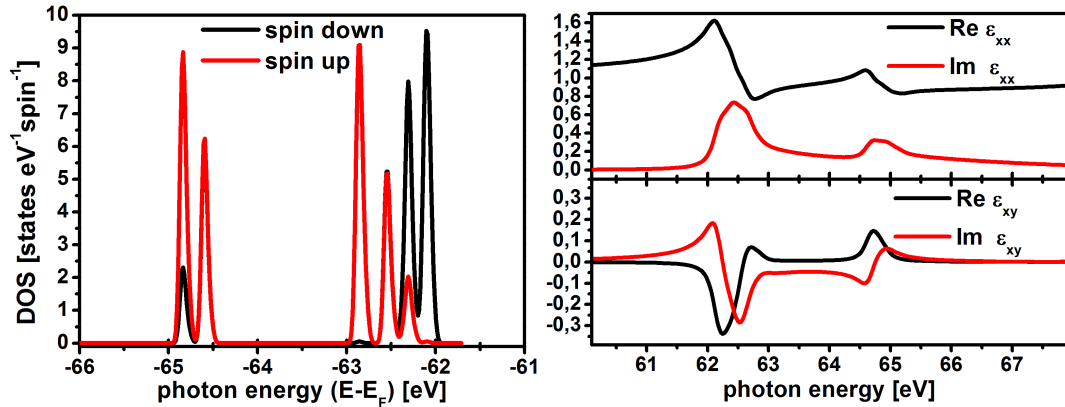


Figure 6.1: Simulation results of the density of states at the Ni 3p edge for a mono-crystalline Ni $\langle 100 \rangle$ sample (left) and the accordingly derived dielectric constants (right).

In addition to the theoretical support, several tentative experiments have been performed, which promisingly continue the experiments shown before. The left graph of figure 6.2 shows a spectrum (black line) and the corresponding asymmetry (red line) of a Ni/Cr/Fe (5 nm/3 nm/5 nm) multilayer grating measured in a T-MOKE reflectivity experiment employing a laser based soft x-ray source. The asymmetry exhibits two pronounced extrema in the vicinity of the M absorption edges of Fe and Ni suggesting that a layer-selective response can be obtained by employing a table-top HHG source rather than a synchrotron. This finding in combination with the experience gathered in this thesis opens the door to perform layer-selective magneto-optical studies of multilayer systems in a laboratory environment, which can be comfortably extended into the time domain benefiting from a high temporal resolution of the HHG based pump-probe approach.

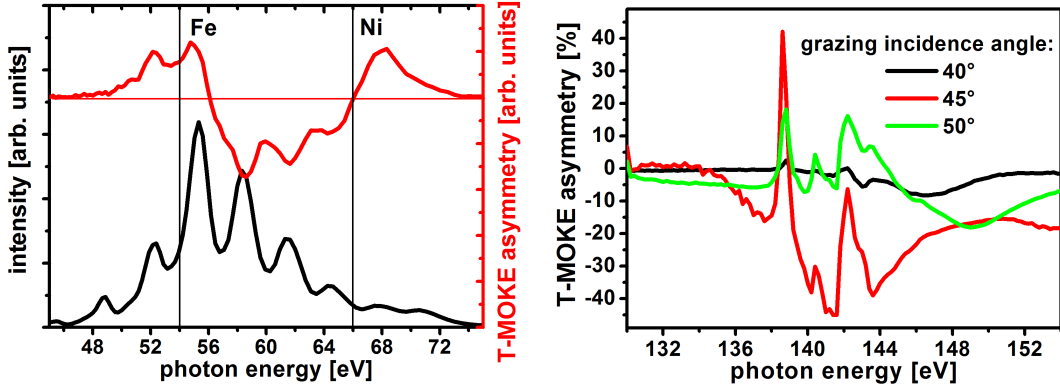


Figure 6.2: HHG spectrum and resulting asymmetry of a Ni/Cr/Fe (5 nm/3 nm/5 nm) multilayer grating (left) and the asymmetry of a Co₆Fe₇₂Gd₂₂ thin film sample at the Gd N_5 absorption edge measured at BESSY for various incidence angles (right).

The right graph of figure 6.2 displays the T-MOKE asymmetry of a Co₆Fe₇₂Gd₂₂ sample, which has been measured at BESSY across the Gd N_5 absorption edge for various incidence angles. This hotly debated sample system containing the 3d transition metals Fe and Co as well as the 4f lanthanide Gd exhibits unique switching properties. So far it has been the first and only system whose magnetic out-of-plane configuration can be optically reversed by a single femtosecond laser pulse exploiting the inverse Faraday effect [98]. Moreover, time- and spin-resolved photoemission experiments on Gd have shown a distinct demagnetization behavior proceeding on the time scale of 100 ps rather than 100 fs in the case of Fe and Ni [131]. Thus, element-selective as well as time-resolved investigations into the underlying magnetic properties of this alloy comprising both 3d and 4f elements are highly desirable.

As can be deduced from the shown asymmetry, a high magnetic contrast of up to 40 % can be exploited at the Gd N absorption edge for an ultrafast element-selective pump-probe experiment, if a table-top soft x-ray source was employed and combined with the gathered experience of the presented work. However, reaching the required photon energy of about 150 eV lies beyond the current capabilities of this laboratory source. Nonetheless, first reports of pushing the cut-off frequency of these table-top soft x-ray sources beyond the water window located around 500 eV raise hopes to perform not only pump-probe experiments at the lanthanide N absorption edge, but also at the L absorption edge of the 3d transition metals in the near future [132].

Appendix

The following drawings and computer code refer to sections 3.3, 3.4, 3.7 and 5.2. These sections introduce custom made electronic and mechanical devices as well as a MATLAB routine, which have been developed and employed in the corresponding experiments. The shown plans are supposed to elucidate the operation of the experiment as well as document the principles behind these unique devices and the computer code programmed to evaluate and display the recorded data.

The first circuit diagram displayed in appendix 1 schematically shows the components of a monopolar power supply providing up to +200 V and featuring an extremely low electronic noise. It has been used to bias the avalanche photodiode via a bias tee in the setup introduced in section 3.3. Thus, a high amplification of the detected EUV photons can be guaranteed in a linear response regime with a good signal-to-noise ratio exploiting the avalanche effect of the employed photodiode.

The second connection diagram shown in appendix 2 illustrates the electric circuit of the stretcher, which electronically extends the photodiode response time from about 10 ns to approximately 110 ns. That is how a sampling ratio of about 1:10 for the 2 MHz digital lock-in amplifier recovering the EUV pulses detected by the avalanche photodiode can be satisfied.

The third connection scheme displayed in appendix 3 diagrams the major electronic components to build an efficient balanced detection scheme for the time-resolved MOKE experiment introduced in section 3.4. It basically comprises two photodiodes, each of which detects either the horizontal or vertical polarization component of the impinging laser light. Both signals are amplified by their respective internal built-in current amplifiers, before they are either subtracted or added by two ICs. Thus, both the difference and the sum of the detected signal can be recorded simultaneously.

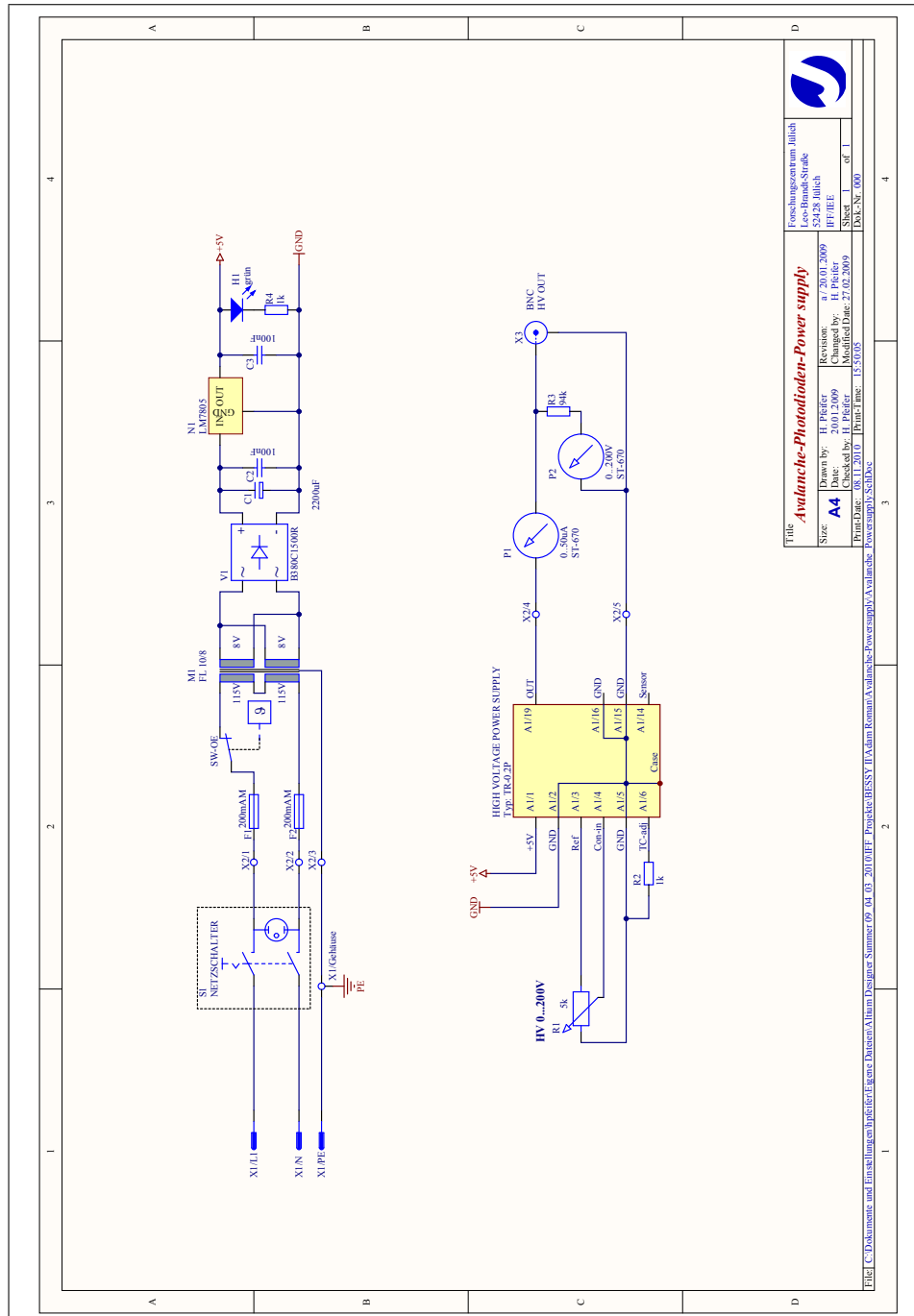
The first mechanical drawing displayed in appendix 4 shows an UHV chamber of the HHG beamline introduced in section 3.7, in the middle of which a toroidal mirror is placed. The toroid is attached to a standard holder, which can be mounted by fork clamps on the triangular baseplate inside the chamber. A turbo pump can be mounted

to either of the CF 60 flanges, whereas the CF 40 flanges serve to guide the laser as well as EUV beam for various reflection geometries.

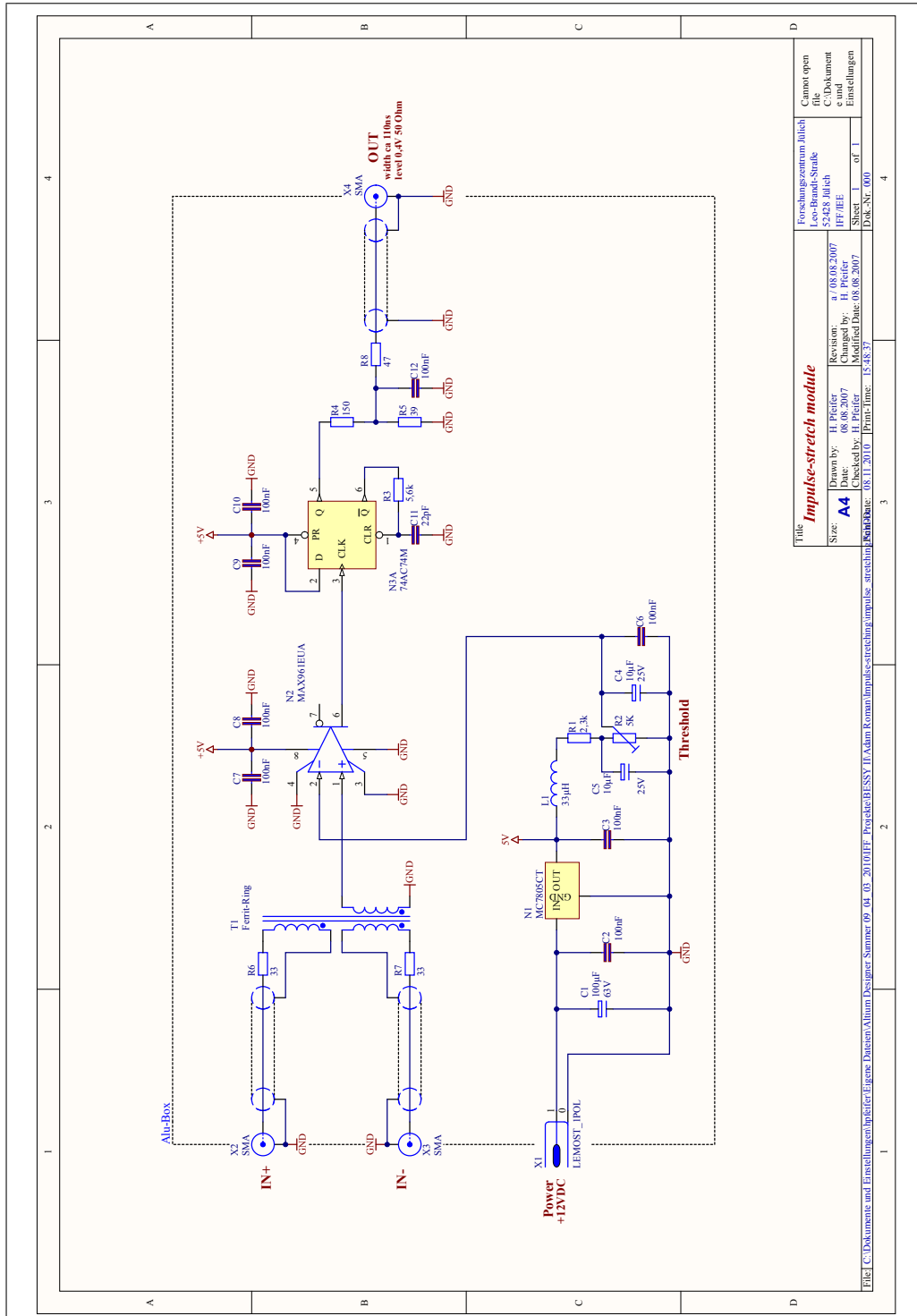
The second mechanical drawing displayed in appendix 5 shows an UHV chamber, which accommodates the sample as well as coils to apply a magnetic field along the vertical sample axis. Similarly, a turbo pump can be mounted to the CF 60 flanges and the CF 40 flanges can admit various gauges, feed-throughs and the EUV beam. The embedded flange, which is connected to the CCD camera via a flexible vacuum tube, allows for the camera to be rotated around the vertical chamber axis and with respect to the embedded flange by about $\pm 10^\circ$. Thus, a robust T-MOKE $\theta - 2\theta$ reflectivity experiment can be realized with θ ranging from about 40° to 50° . An illustration of the assembled chambers and the core of the reflectivity experimental setup is displayed in section 6 of the appendix.

The computer code, written in MATLAB, which has been used to evaluate the data obtained from the HHG T-MOKE experiment is shown in appendix 7. It basically loads the data recorded by the CCD camera and calculates as well as displays the asymmetry extracted from the recorded spectra and harmonics as a function of the applied magnetic field and the pump-probe delay, respectively. Moreover, it includes a routine to energetically calibrate the spectrum by means of the well-known grating equation.

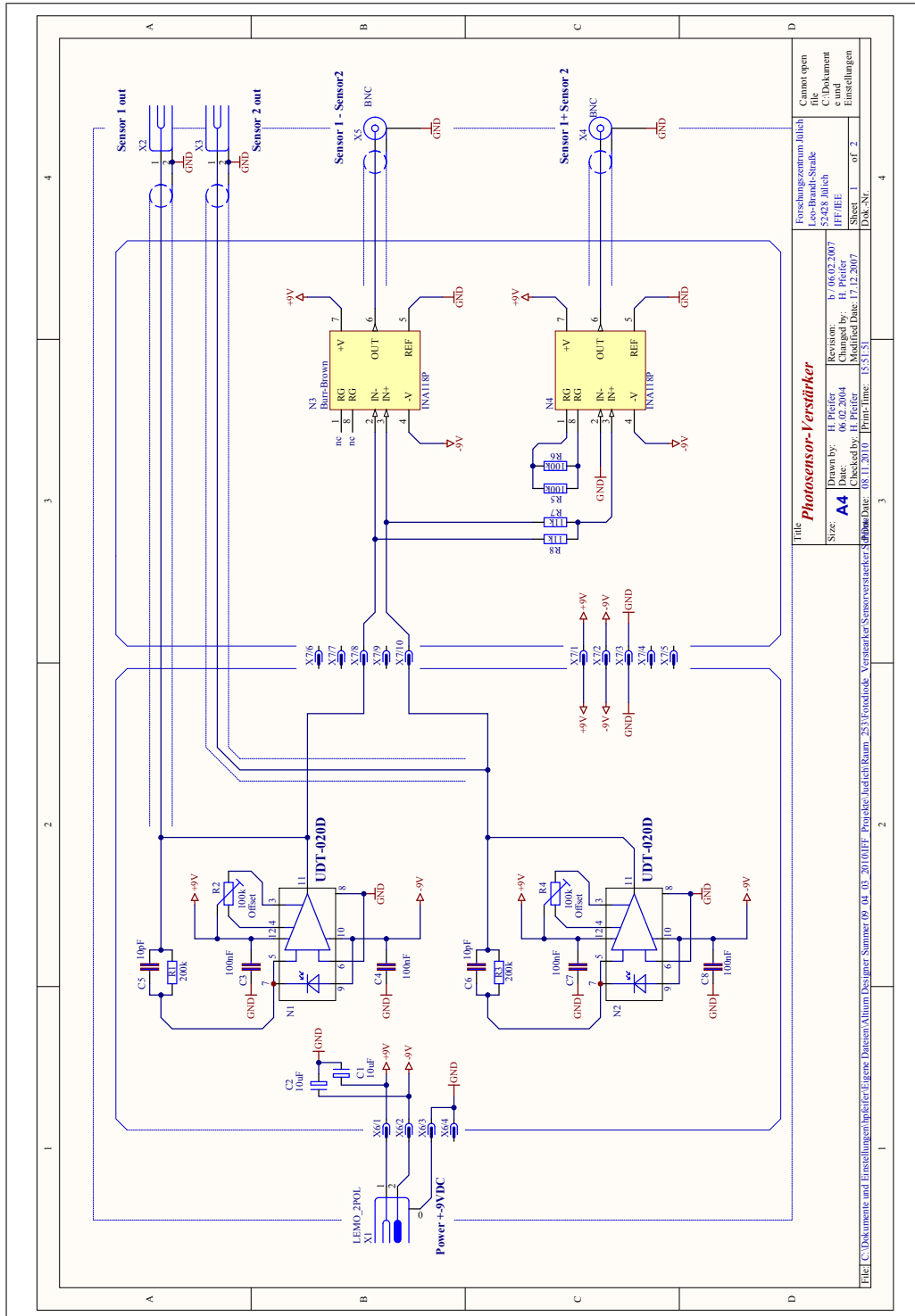
1 APD Powersupply



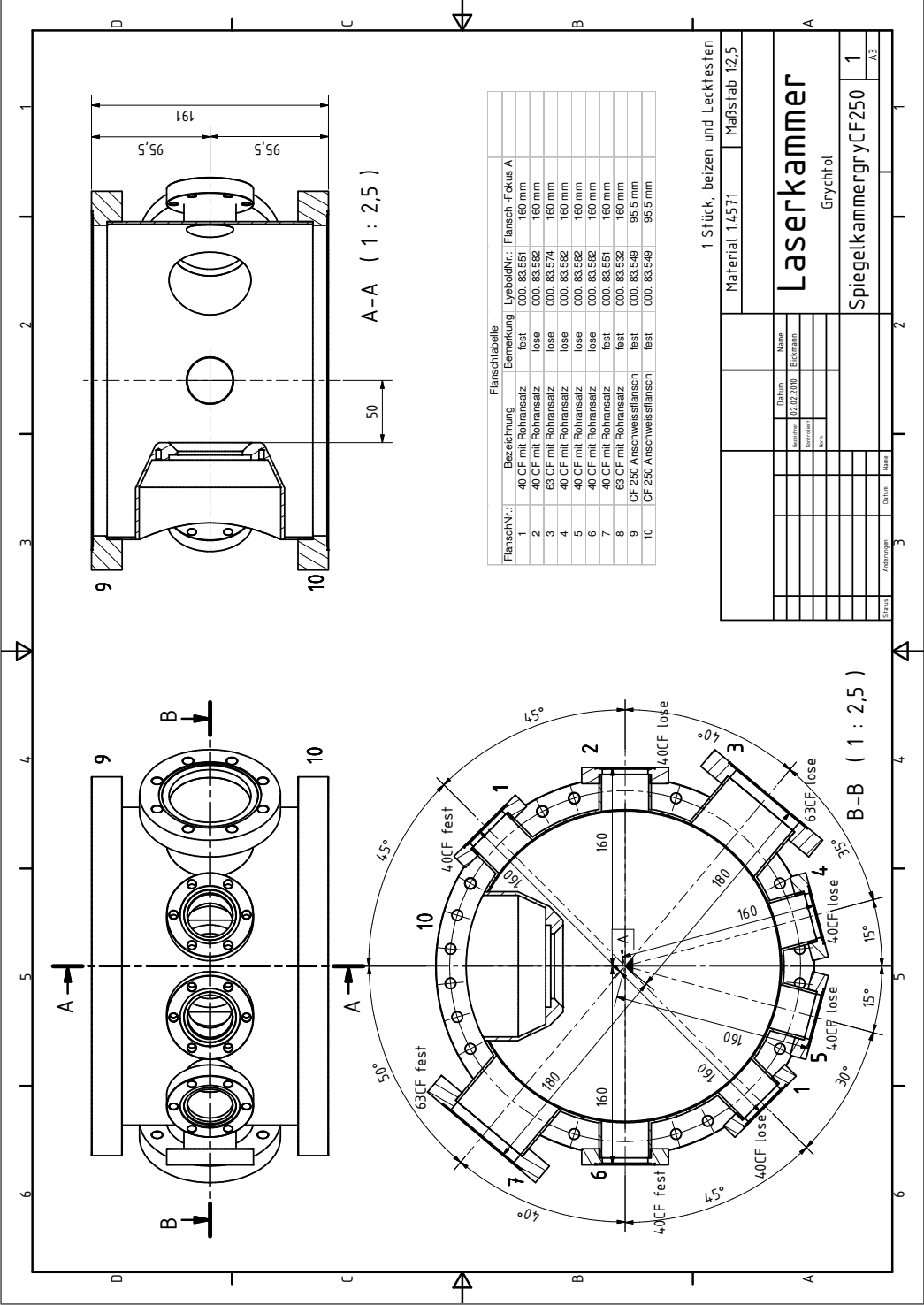
2 Pulse Stretcher



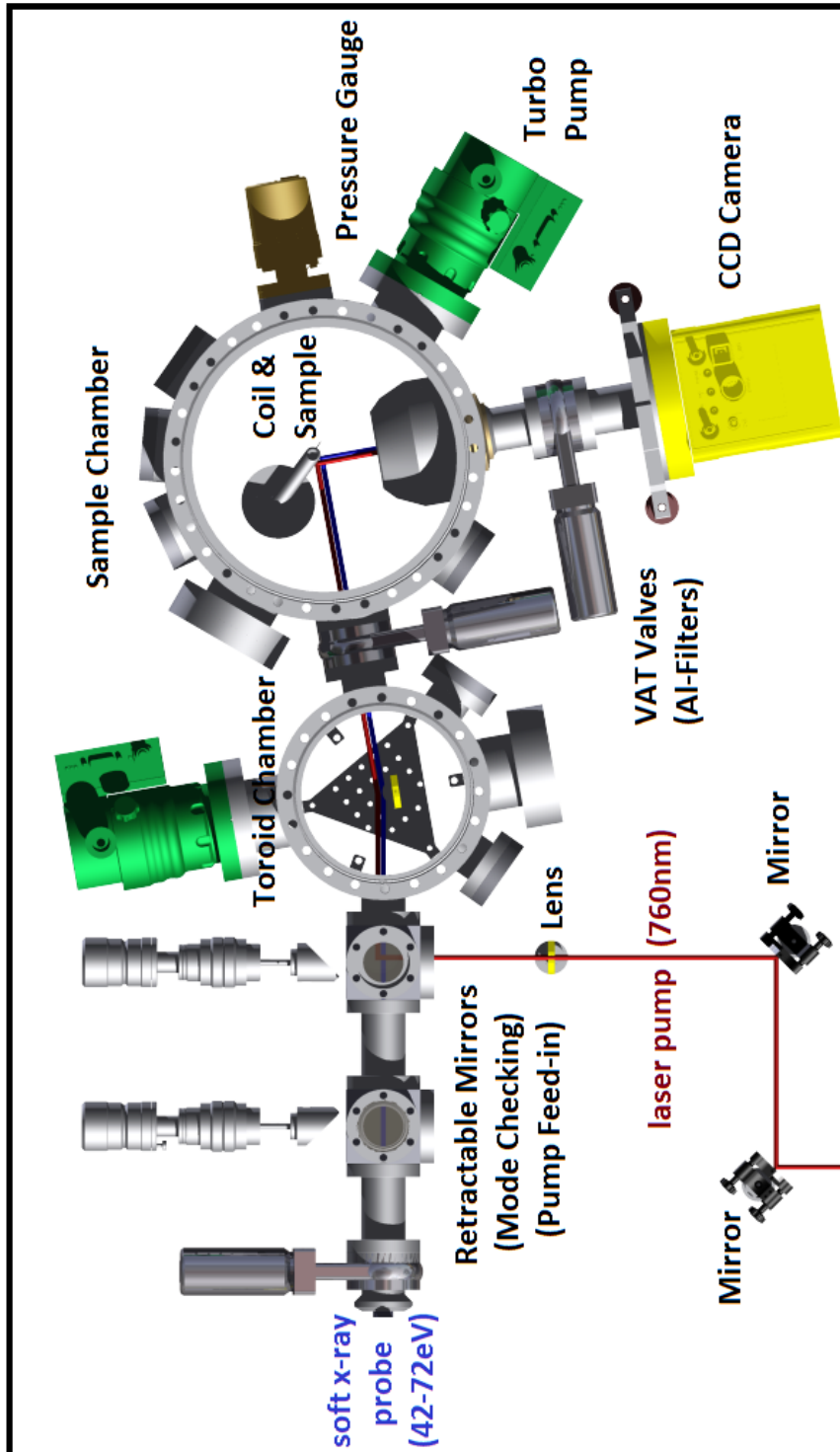
3 Balanced Detection Scheme



5 Sample Chamber



6 HHG Reflectivity Experiment



7 MATLAB Evaluation Routine

```

1  %% loading spectra and evaluating harmonics

3  close all
4  clear all

6  % loading data

8  path=['C:\Boulder\Data\Time-Resolved\PyCu\PyCu7\0813\TR1\'];

10 maximum_number_index = 61; % manual input

12 for i=1:maximum_number_index
13     % specify shortcut of filename
14     shortcut1 = [ num2str(i) ' average signal pos ' '*' '.txt' ];
15     % looking for variable filename in path
16     file1 = dir(fullfile(path,shortcut1));
17     % extracting full name of file to be read
18     filepath1 = [path,file1.name];
19     % finding and considering non-existing data files
20     if ~isdir(filepath1)
21         delay_index(:,i) = str2num( file1.name(findstr('pos',file1.name)
22                                     +3:findstr('.txt',file1.name)-1));
23     else
24         delay_index(:,i) = NaN;
25     end
26 end

28 % sort and find maximum delay
29 sorted_delay = unique(sort(delay_index));
30 finish_at = find(sorted_delay == max(sorted_delay));

32 for i=1:finish_at
33     delay_value = sorted_delay(i);
34     hit = find(delay_index==delay_value);

36     for j = 1:size(hit,2)

38         filepath = [path,num2str(find(delay_index==delay_value)),
39                     ' all spectra pos ',num2str(delay_value),'.txt'];

41         % load all single spectra for the single delay step i
42         all_spectra = importdata(filepath);

44         % calculate averaged spectrum for the single delay step i
45         mean_all_spectra = mean(all_spectra,2);
46         std_all_spectra = std(all_spectra,0,2);

```

```

49      % eliminate cosmic ray events from spectrum
50      for k=1:size(all_spectra,2)
51          mean_rest_of_spectra = (sum(all_spectra,2)-all_spectra(:,k)) /
52                                  (size(all_spectra,2)-1);
53          mask = abs(mean_rest_of_spectra -all_spectra(:,k)) >
54                  5*std_all_spectra;
55          all_spectra(:,k)= all_spectra(:,k).*(~mask)+
56                          mask.*(mean_rest_of_spectra);
57      end

59      % define spectra for magnetic field up (odd) and down (even)
60      for l=1:size(all_spectra,2)
61          if mod(l,2)
62              odd_spectra(:,ceil(l/2))= all_spectra(:,l);
63          else
64              even_spectra(:,l/2) = all_spectra(:,l);
65          end
66      end

68      % background subtraction
69      bg_odd = mean(odd_spectra(450:500,:));
70      bg_even = mean(even_spectra(450:500,:));

72      odd_spectra = odd_spectra-ones(1024,1)*bg_odd;
73      even_spectra = even_spectra-ones(1024,1)*bg_even;
74      all_asymmetry = (odd_spectra-even_spectra)./
75                      (odd_spectra+even_spectra+100);

77      end

79      ave_even_spectrum = mean(even_spectra,2);
80      ave_odd_spectrum = mean(odd_spectra,2);
81      ave_asymmetry = mean(all_asymmetry,2);

83      all_even_spectrum(:,i) = ave_even_spectrum;
84      all_odd_spectrum(:,i) = ave_odd_spectrum;

86      integral = 5; % manual input

88      peakpos_l = [383,394,404,413,420,424,432]; % manual input
89      peakpos_r = [754,742,732,723,715,708,706]; % manual input

91      pos52p1eV_l = peakpos_l(1);
92      Har52p1eV_l(i) = mean(abs(ave_asymmetry(pos52p1eV_l-integral:
93                                          pos52p1eV_l+integral)));

94      pos52p1eV_r = peakpos_r(1);
95      Har52p1eV_r(i) = mean(abs(ave_asymmetry(pos52p1eV_r-integral:
96                                          pos52p1eV_r+integral)));

```



```

97     pos55p3eV_l = peakpos_l(2);
98     Har55p3eV_l(i) = mean(abs(ave_asymmetry(pos55p3eV_l-integral:
    pos55p3eV_l+integral)));

100     pos55p3eV_r = peakpos_r(2);
101     Har55p3eV_r(i) = mean(abs(ave_asymmetry(pos55p3eV_r-integral:
    pos55p3eV_r+integral)));

103     pos58p5eV_l = peakpos_l(3);
104     Har58p5eV_l(i) = mean(abs(ave_asymmetry(pos58p5eV_l-integral:
    pos58p5eV_l+integral)));

106     pos58p5eV_r = peakpos_r(3);
107     Har58p5eV_r(i) = mean(abs(ave_asymmetry(pos58p5eV_r-integral:
    pos58p5eV_r+integral)));

109     pos61p6eV_l = peakpos_l(4);
110     Har61p6eV_l(i) = mean(abs(ave_asymmetry(pos61p6eV_l-integral:
    pos61p6eV_l+integral)));

112     pos61p6eV_r = peakpos_r(4);
113     Har61p6eV_r(i) = mean(abs(ave_asymmetry(pos61p6eV_r-integral:
    pos61p6eV_r+integral)));

115     pos64p8eV_l = peakpos_l(5);
116     Har64p8eV_l(i) = mean(abs(ave_asymmetry(pos64p8eV_l-integral:
    pos64p8eV_l+integral)));

118     pos64p8eV_r = peakpos_r(5);
119     Har64p8eV_r(i) = mean(abs(ave_asymmetry(pos64p8eV_r-integral:
    pos64p8eV_r+integral)));

121     pos67p9eV_l = peakpos_l(6);
122     Har67p9eV_l(i) = mean(abs(ave_asymmetry(pos67p9eV_l-integral:
    pos67p9eV_l+integral)));

124     pos67p9eV_r = peakpos_r(6);
125     Har67p9eV_r(i) = mean(abs(ave_asymmetry(pos67p9eV_r-integral:
    pos67p9eV_r+integral)));

127     pos71p1eV_l = peakpos_l(7);
128     Har71p1eV_l(i) = mean(abs(ave_asymmetry(pos71p1eV_l-integral:
    pos71p1eV_l+integral)));

130     pos71p1eV_r = peakpos_r(7);
131     Har71p1eV_r(i) = mean(abs(ave_asymmetry(pos71p1eV_r-integral:
    pos71p1eV_r+integral)));

133 end

```

```

135 eV = [52.1, 55.3, 58.5, 61.6, 64.8, 67.9, 71.1];

137 HarTR1_l = [Har52p1eV_l', Har55p3eV_l', Har58p5eV_l', Har61p6eV_l',
138             Har64p8eV_l', Har67p9eV_l', Har71p1eV_l'];
HarTR1_r = [Har52p1eV_r', Har55p3eV_r', Har58p5eV_r', Har61p6eV_r',
            Har64p8eV_r', Har67p9eV_r', Har71p1eV_r'];

140 HarPos_l = [pos52p1eV_l, pos55p3eV_l, pos58p5eV_l, pos61p6eV_l,
141             pos64p8eV_l, pos67p9eV_l, pos71p1eV_l];
HarVal_l = [ave_even_spectrum(pos52p1eV_l), ave_even_spectrum(
            pos55p3eV_l), ave_even_spectrum(pos58p5eV_l), ave_even_spectrum(
            pos61p6eV_l), ave_even_spectrum(pos64p8eV_l), ave_even_spectrum(
            pos67p9eV_l), ave_even_spectrum(pos71p1eV_l)];

143 HarPos_r = [pos52p1eV_r, pos55p3eV_r, pos58p5eV_r, pos61p6eV_r,
144             pos64p8eV_r, pos67p9eV_r, pos71p1eV_r];
HarVal_r = [ave_even_spectrum(pos52p1eV_r), ave_even_spectrum(
            pos55p3eV_r), ave_even_spectrum(pos58p5eV_r), ave_even_spectrum(
            pos61p6eV_r), ave_even_spectrum(pos64p8eV_r), ave_even_spectrum(
            pos67p9eV_r), ave_even_spectrum(pos71p1eV_r)];

146 sorted_delay(isnan(sorted_delay))=[];
147 ps = sorted_delay*2/.3/1000;

149 clear pos49p0eV_l pos52p1eV_l pos55p3eV_l pos58p5eV_l pos61p6eV_l
      pos64p8eV_l pos67p9eV_l position integral harmonics all_asymmetry
      all_spectra ans bg delay_index delay_to_look delay_value even_spectra
      file1 filepath1 filepath1 i j k l mask finishFe finishNi finish_at
      hit maximum_number_index odd_spectra path shortcut1 pos49p0eV_r
      pos52p1eV_r pos55p3eV_r pos58p5eV_r pos61p6eV_r pos64p8eV_r
      pos67p9eV_r

151 %% plot a single data set
152 figure(11)
153 hold on

155 plot(ps, Har52p1eV_l/mean(Har52p1eV_l(1:10)), 'Color', 'red')
156 plot(ps, Har55p3eV_l/mean(Har55p3eV_l(1:10)), 'Color', 'blue')
157 plot(ps, Har58p5eV_l/mean(Har58p5eV_l(1:10)), 'Color', 'green')
158 plot(ps, Har61p6eV_l/mean(Har61p6eV_l(1:10)), 'Color', 'yellow')
159 plot(ps, Har64p8eV_l/mean(Har64p8eV_l(1:10)), 'Color', 'magenta')
160 plot(ps, Har67p9eV_l/mean(Har67p9eV_l(1:10)), 'Color', 'cyan')
161 plot(ps, Har71p1eV_l/mean(Har71p1eV_l(1:10)), 'Color', 'black')
162 ylim([0 1.5])

164 xlabel('delay in ps')
165 ylabel('normalized magnetic asymmetry in %')
166 title('Temporal evolution of the magnetic asymmetry - left side')
167 hold off

```

```

169 figure(22)
170 hold on

172 plot(ps, Har52p1eV_r/mean(Har52p1eV_r(1:10)), 'Color', 'red')
173 plot(ps, Har55p3eV_r/mean(Har55p3eV_r(1:10)), 'Color', 'blue')
174 plot(ps, Har58p5eV_r/mean(Har58p5eV_r(1:10)), 'Color', 'green')
175 plot(ps, Har61p6eV_r/mean(Har61p6eV_r(1:10)), 'Color', 'yellow')
176 plot(ps, Har64p8eV_r/mean(Har64p8eV_r(1:10)), 'Color', 'magenta')
177 plot(ps, Har67p9eV_r/mean(Har67p9eV_r(1:10)), 'Color', 'cyan')
178 plot(ps, Har71p1eV_r/mean(Har71p1eV_r(1:10)), 'Color', 'black')
179 ylim([0 1.5])

181 xlabel('delay in ps')
182 ylabel('normalized magnetic asymmetry in %')
183 title('Temporal evolution of the magnetic asymmetry – right side')
184 hold off

187 figure(33)
188 hold on
189 plot(mean(all_even_spectrum,2));
190 plot(mean(all_odd_spectrum,2), 'Color', 'red');
191 hold off
192 xlim([300 800])
193 ylim([0 1000])

196 figure(44)
197 hold on
198 plot(ave_even_spectrum);
199 plot(ave_odd_spectrum, 'Color', 'red');
200 hold off

202 xlim([300 450])

204 for harmonics=1:size(eV,2)
205 label = sprintf('\\leftarrow %.2f eV',eV(harmonics));
206 figure(44),text(HarPos_l(harmonics),HarVal_l(harmonics)+50,label, '
    HorizontalAlignment','left','Rotation',90,'Color','black')
207 end

210 figure(55)
211 hold on
212 plot(ave_even_spectrum);
213 plot(ave_odd_spectrum, 'Color', 'red');
214 hold off

216 xlim([600 800])

```

```

218 for harmonics=1:size(eV,2)
219 label = sprintf('\leftarrow %.2f eV',eV(harmonics));
220 figure(55),text(HarPos_r(harmonics),HarVal_r(harmonics)+50,label,'
    HorizontalAlignment','left','Rotation',90,'Color','black')
221 end

223 clear eV HarVal_l HarVal_r harmonics label sorted_delay peaks value
    Har71p1eV_l Har49p0eV_l Har52p1eV_l Har55p3eV_l Har58p5eV_l
    Har61p6eV_l Har64p8eV_l Har67p9eV_l Off stdpos ave_even_spectrum
    ave_asymmetry ave_odd_spectrum mean_rest_of_spectra mean_all_spectra
    std_all_spectra bg_even bg_odd Har71p1eV_r Har49p0eV_r Har52p1eV_r
    Har55p3eV_r Har58p5eV_r Har61p6eV_r Har64p8eV_r Har67p9eV_r
    pos71p1eV_l pos71p1eV_r pos pos71p1eV_r all_even_spectrum
    all_odd_spectrum

225 %% find maxima of spectrum
226 [value position] = findpeaks(ave_even_spectrum(200:450), 'minpeakheight',
    880, 'minpeakdistance', 5);
227 peak_position = position+199;

229 %% analyze and calibrate HHG spectrum
230 figure(22)
231 plot(ave_spectrum,'black')
232 xlim([200 450]);
233 ylim([820 1700]);
234 xlabel('number of pixel')
235 ylabel('CCD intensity (counts)')
236 title('Reflectivity spectrum of PyCu7')

238 d = 2E-6; % grating peroid
239 x = 26E-6; % CCD pixel size
240 h = 6.6256*10^-34; % Plank'constant
241 c = 299792458; % speed of light
242 e = 1.602*10^-19; % electron charge
243 center = 543; % pixel of zero order harmonic

245 % Locate the pixel number with corresponding energy
246 % Look at asymmetry and Al edge for a hint

248 n = center - [232,261,285,305,322,337,350,362,372,381,389,397,403];

250 %odd multiples of photon energy each harmonics
251 eV = [33.18,36.34,39.5,42.66,45.82,48.98,52.14,55.3,58.46,
252     61.62,64.78,67.94,71.1];

254 lamb = h*c/e./eV;

256 %open up curve fitting toolbox cftool
257 %fit equation y=(asin(x/(2*10^-6))-sin(a))+a)*b/26e-6

```

```

258 %where y=n and x=lamb a=angle of incidence b=sample CCD distance
260 a = -1.183; % actual value -0.77 (45 )
261 b = 0.1531; % actual value 0.3 (30cm)

264 %labeling the plot
265 label = sprintf('angle of incidence = %.2f degree \nCCD to sample
distance = %.2f cm',a*180/pi,b*100);
266 figure(22),text(center-300, ave_spectrum(center)-50000,label);

268 figure(22),text(30, ave_spectrum(center)-50000,'red = first order green
= second order blue=third order');

270 %first order
271 for harmonics=1:size(eV,2)
272 label = sprintf('\leftarrow %.2f eV',eV(harmonics));
273 pixel = round(center-(asin(lamb(harmonics)/d-sin(a))+a)*b/x);
274 figure(22),text(pixel,ave_spectrum(pixel)+50,label,'HorizontalAlignment',
'left','Rotation',90,'Color','red')
275 end

```

Bibliography

- [1] G. Binasch, P. Grünberg, F. Saurenbach, and W. Zinn. Enhanced magnetoresistance in layered magnetic structures with antiferromagnetic interlayer exchange. *PHYSICAL REVIEW B*, 39(7):4828, March 1989.
- [2] J. A. C. Bland and B. Heinrich, editors. *Ultrathin Magnetic Structures I: An Introduction to the Electronic, Magnetic and Structural Properties*. Springer-Verlag Telos, June 1994.
- [3] P. Grünberg, R. Schreiber, Y. Pang, M. B. Brodsky, and H. Sowers. Layered magnetic structures: Evidence for antiferromagnetic coupling of Fe layers across Cr interlayers. *PHYSICAL REVIEW LETTERS*, 57(19):2442, November 1986.
- [4] J. S. Moodera, L. R. Kinder, T. M. Wong, and R. Meservey. Large magnetoresistance at room temperature in ferromagnetic thin film tunnel junctions. *PHYSICAL REVIEW LETTERS*, 74(16):3273, April 1995.
- [5] S. Parkin, X. Jiang, C. Kaiser, A. Panchula, K. Roche, and M. Samant. Magnetically engineered spintronic sensors and memory. *Proceedings of the IEEE*, 91(5):661, May 2003.
- [6] A. Berger. *Spintronics*, chapter Technology of Hard Disk Drives. 40th IFF Spring School. Forschungszentrum Jülich, 2009.
- [7] R. Jansen. The spin-valve transistor: a review and outlook. *JOURNAL OF APPLIED PHYSICS D: APPLIED PHYSICS*, 36(19):R289, October 2003.
- [8] B. Hillebrands. *Spin dynamics in confined magnetic structures*, volume 1, 2, 3. Springer Berlin, 2002, 2004.
- [9] I. Zutic, J. Fabian, and S. Das Sarma. Spintronics: Fundamentals and applications. *REVIEWS OF MODERN PHYSICS*, 76(2):323, April 2004.
- [10] G. Reiss. *Spintronics*, chapter Magnetic Logic. 40th IFF Spring School. Forschungszentrum Jülich, 2009.

- [11] S. S. P. Parkin, K. P. Roche, M. G. Samant, P. M. Rice, R. B. Beyers, R. E. Scheuerlein, E. J. O'Sullivan, S. L. Brown, J. Bucchigano, D. W. Abraham, Yu Lu, M. Rooks, P. L. Trouilloud, R. A. Wanner, and W. J. Gallagher. Exchange-biased magnetic tunnel junctions and application to nonvolatile magnetic random access memory (invited). *JOURNAL OF APPLIED PHYSICS*, 85(8):5828, April 1999.
- [12] D. A. Allwood, G. Xiong, and R. P. Cowburn. Writing and erasing data in magnetic domain wall logic systems. *JOURNAL OF APPLIED PHYSICS*, 100(12):123908, 2006.
- [13] R. Hertel and C. M. Schneider. Exchange explosions: Magnetization dynamics during vortex-antivortex annihilation. *PHYSICAL REVIEW LETTERS*, 97(17):177202, 2006.
- [14] Th. Gerrits, H. A. M. van den Berg, J. Hohlfield, L. Bar, and Th. Rasing. Ultrafast precessional magnetization reversal by picosecond magnetic field pulse shaping. *NATURE*, 418(6897):509, August 2002.
- [15] B. Koopmans, G. Malinowski, F. Dalla Longa, D. Steiauf, M. Fahnle, T. Roth, M. Cinchetti, and M. Aeschlimann. Explaining the paradoxical diversity of ultrafast laser-induced demagnetization. *NATURE MATERIALS*, 9(3):259, March 2010.
- [16] A. Kirilyuk, A. V. Kimel, and T. Rasing. Ultrafast optical manipulation of magnetic order. *REVIEWS OF MODERN PHYSICS*, 82(3):2731, September 2010.
- [17] J. Kerr. XLIII. On rotation of the plane of polarization by reflection from the pole of a magnet. *PHILOSOPHICAL MAGAZINE SERIES 5*, 3(19):321, May 1877.
- [18] J. Kerr. XXIV. On reflection of polarized light from the equatorial surface of a magnet. *PHILOSOPHICAL MAGAZINE SERIES 5*, 5(30):161, March 1878.
- [19] R. L. Conger and J. L. Tomlinson. Magneto-optic readout for computer memories. *JOURNAL OF APPLIED PHYSICS*, 33(3):1059, March 1962.
- [20] M. H. Kryder and F. B. Humphrey. Dynamic kerr observations of high speed flux reversal and relaxation processes in permalloy thin films. *JOURNAL OF APPLIED PHYSICS*, 40(3):1225, March 1969.
- [21] E. Beaurepaire, J.-C. Merle, A. Daunois, and J.-Y. Bigot. Ultrafast spin dynamics in ferromagnetic nickel. *PHYSICAL REVIEW LETTERS*, 76(22):4250, May 1996.

-
- [22] J. Walowski, G. Müller, M. Djordjevic, M. Münzenberg, M. Klaui, C. A. F. Vaz, and J. A. C. Bland. Energy equilibration processes of electrons, magnons, and phonons at the femtosecond time scale. *PHYSICAL REVIEW LETTERS*, 101(23):237401, December 2008.
- [23] I. Radu, G. Woltersdorf, M. Kiessling, A. Melnikov, U. Bovensiepen, J.-U. Thiele, and C. H. Back. Laser-induced magnetization dynamics of lanthanide-doped permalloy thin films. *PHYSICAL REVIEW LETTERS*, 102(11):117201, March 2009.
- [24] J.-Y. Bigot, M. Vomir, and E. Beaurepaire. Coherent ultrafast magnetism induced by femtosecond laser pulses. *NATURE PHYSICS*, 5(7):515, July 2009.
- [25] A.K. Zvezdin and V.A. Kotov. *Modern Magnetooptics and Magneto-optical Materials*. Institute of Physics Publishing, Bristol, 1997.
- [26] G. Schütz, W. Wagner, W. Wilhelm, P. Kienle, R. Zeller, R. Frahm, and G. Materlik. Absorption of circularly polarized x-rays in iron. *PHYSICAL REVIEW LETTERS*, 58(7):737, February 1987.
- [27] G. van der Laan, B. T. Thole, G. A. Sawatzky, J. B. Goedkoop, J. C. Fuggle, J.-M. Esteve, R. Karnatak, J. P. Remeika, and H. A. Dabkowska. Experimental proof of magnetic x-ray dichroism. *PHYSICAL REVIEW B*, 34(9):6529, November 1986.
- [28] C. Kao, J. B. Hastings, E. D. Johnson, D. P. Siddons, G. C. Smith, and G. A. Prinz. Magnetic-resonance exchange scattering at the iron L2 and L3 edges. *PHYSICAL REVIEW LETTERS*, 65(3):373, July 1990.
- [29] H.-Ch. Mertins, D. Abramsohn, A. Gaupp, F. Schäfers, W. Gudat, O. Zaharko, H. Grimmer, and P. M. Oppeneer. Resonant magnetic reflection coefficients at the Fe 2p edge obtained with linearly and circularly polarized soft x-rays. *PHYSICAL REVIEW B*, 66(18):184404, November 2002.
- [30] F. Nolting, A. Scholl, J. Stöhr, J. W. Seo, J. Fompeyrine, H. Siegwart, J.-P. Locquet, S. Anders, J. Lüning, E. E. Fullerton, M. F. Toney, M. R. Scheinfein, and H. A. Padmore. Direct observation of the alignment of ferromagnetic spins by antiferromagnetic spins. *NATURE*, 405(6788):767, June 2000.
- [31] C. Stamm, T. Kachel, N. Pontius, R. Mitzner, T. Quast, K. Holldack, S. Khan, C. Lupulescu, E. F. Aziz, M. Wietstruk, H. A. Dürr, and W. Eberhardt. Femtosecond modification of electron localization and transfer of angular momentum in nickel. *NATURE MATERIALS*, 6(10):740, October 2007.

- [32] C. Gutt, L.-M. Stadler, S. Streit-Nierobisch, A. P. Mancuso, A. Schropp, B. Pfau, C. M. Gunther, R. Konnecke, J. Gulden, B. Reime, J. Feldhaus, E. Weckert, I. A. Vartanyants, O. Hellwig, F. Staier, R. Barth, M. Grunze, A. Rosenhahn, D. Stickler, H. Stillrich, R. Fromter, H. P. Oepen, M. Martins, T. Nisius, T. Wilhelm, B. Faatz, N. Guerassimova, K. Honkavaara, V. Kocharyan, R. Treusch, E. Saldin, S. Schreiber, E. A. Schneidmiller, M. V. Yurkov, S. Eisebitt, and G. Grübel. Resonant magnetic scattering with soft x-ray pulses from a free-electron laser operating at 1.59 nm. *PHYSICAL REVIEW B*, 79(21):212406, June 2009.
- [33] F. U. Hillebrecht, T. Kinoshita, D. Spanke, J. Dresselhaus, Ch. Roth, H. B. Rose, and E. Kisker. New magnetic linear dichroism in total photoelectron yield for magnetic domain imaging. *PHYSICAL REVIEW LETTERS*, 75(11):2224, September 1995.
- [34] M. Pretorius, J. Friedrich, A. Ranck, M. Schroeder, J. Voss, V. Wedemeier, D. Spanke, D. Knabben, I. Rozhko, H. Ohldag, F. U. Hillebrecht, and E. Kisker. Transverse magneto-optical Kerr effect of Fe at the Fe 3p threshold. *PHYSICAL REVIEW B*, 55(21):14133, June 1997.
- [35] M. Sacchi, G. Panaccione, J. Vogel, A. Mirone, and G. Laan. Magnetic dichroism in reflectivity and photoemission using linearly polarized light: 3p core level of Ni(110). *PHYSICAL REVIEW B*, 58(7):3750, August 1998.
- [36] M. Hecker, P.M. Oppeneer, S. Valencia, H.-C. Mertins, and C.M. Schneider. Soft x-ray magnetic reflection spectroscopy at the 3p absorption edges of thin Fe films. *JOURNAL OF ELECTRON SPECTROSCOPY AND RELATED PHENOMENA*, 144:881, 2005.
- [37] S. Valencia, A. Gaupp, W. Gudat, H.-Ch Mertins, P. M. Oppeneer, D. Abramsohn, and C. M. Schneider. Faraday rotation spectra at shallow core levels: 3p edges of Fe, Co and Ni. *NEW JOURNAL OF PHYSICS*, 8(10):254, 2006.
- [38] H. C. Kapteyn, M. M. Murnane, and I. P. Christov. Extreme nonlinear optics: Coherent x-rays from lasers. *PHYSICS TODAY*, 58(3):39, March 2005.
- [39] X Zhou, R. Lock, N. Wagner, W. Li, H. C. Kapteyn, and M. M. Murnane. Elliptically polarized high-order harmonic emission from molecules in linearly polarized laser fields. *PHYSICAL REVIEW LETTERS*, 102(7):073902, February 2009.
- [40] T. Popmintchev, M. Chen, A. Bahabad, M. Gerrity, P. Sidorenko, O. Cohen, I. P. Christov, M. M. Murnane, and H. C. Kapteyn. Phase matching of high harmonic

- generation in the soft and hard x-ray regions of the spectrum. *PROCEEDINGS OF THE NATIONAL ACADEMY OF SCIENCE*, 106(26):10516, June 2009.
- [41] C. La-O-Vorakiat, M. Siemens, M. M. Murnane, H. C. Kapteyn, S. Mathias, M. Aeschlimann, P. Grychtol, R. Adam, C. M. Schneider, J. M. Shaw, H. Nembach, and T. J. Silva. Ultrafast demagnetization dynamics at the m edges of magnetic elements observed using a tabletop high-harmonic soft x-ray source. *PHYSICAL REVIEW LETTERS*, 103(25):257402, December 2009.
 - [42] R. L. Sandberg, D. A. Raymondson, C. La-O-Vorakiat, A. Paul, K. S. Raines, J. Miao, M. M. Murnane, H. C. Kapteyn, and W. F. Schlotter. Tabletop soft-x-ray fourier transform holography with 50 nm resolution. *OPTICS LETTERS*, 34(11):1618, June 2009.
 - [43] W. Voigt. *Magneto- und Elektrooptik*. Teubner, Leipzig, 1908.
 - [44] P.M. Oppeneer. *Magneto-Optical Kerr Spectra*, volume 13 of *Handbook of Magnetic Materials*. Elsevier Amsterdam, 2001.
 - [45] Marco Pretorius. *Magnetooptische Effekte mit linear polarisierter Synchrotronstrahlung im Bereich der 3p-Absorptionskanten der 3d-Übergangsmetalle Fe, Co und Ni*. PhD thesis, Universität Hamburg, 1999.
 - [46] M. A. Schröder. *Magnetooptische Kerr-Effekte im VUV an Eisen und Eisensystemen*. PhD thesis, Universität Hamburg, 2000.
 - [47] J. D. Jackson. *Classical Electrodynamics*. J. Wiley, New York, 3rd edition, 1981.
 - [48] E. Hecht and A. Zajac. *Optics*. Addison Wesley Publishing Company, 3rd edition, 1997.
 - [49] M. Born and E. Wolf. *Principles of Optics: Electromagnetic Theory of Propagation, Interference and Diffraction of Light*. Cambridge University Press, 6 edition, 1997.
 - [50] Z. J. Yang and M. R. Scheinfein. Combined three-axis surface magneto-optical Kerr effects in the study of surface and ultrathin-film magnetism. *JOURNAL OF APPLIED PHYSICS*, 74(11):6810, December 1993.
 - [51] A. Hubert and R. Schäfer. *Magnetic Domains: The Analysis of Magnetic Microstructures*. Springer, Berlin, 1997.
 - [52] P. Yeh. Optics of anisotropic layered media: A new 4x4 matrix algebra. *SURFACE SCIENCE*, 96(1-3):41, June 1980.

- [53] J. Zak, E. R. Moog, C. Liu, and S. D. Bader. Magneto-optics of multilayers with arbitrary magnetization directions. *PHYSICAL REVIEW B*, 43(8):6423, March 1991.
- [54] S. Valencia, A. Gaupp, W. Gudat, Ll. Abad, Ll. Balcells, and B. Martinez. X-ray magnetic circular dichroism in reflection geometry: A tool for investigating surface magnetism in thin films. *JOURNAL OF APPLIED PHYSICS*, 104(2):023903, July 2008.
- [55] L. Nénot and P. Croce. Caractérisation des surfaces par réflexion rasante de rayons x. application a l'étude du polissage de quelques verres silicates. *REVUE DE PHYSIQUE APPLIQUÉE (PARIS)*, 15:761, March 1980.
- [56] K. Stoev and K. Sakurai. Recent theoretical models in grazing incidence x-ray reflectometry. *THE RIGAKU JOURNAL*, 14(2):22, 1997.
- [57] D. E. Savage, J. Kleiner, N. Schimke, Y.-H. Phang, T. Jankowski, J. Jacobs, R. Kariotis, and M. G. Lagally. Determination of roughness correlations in multilayer films for x-ray mirrors. *JOURNAL OF APPLIED PHYSICS*, 69(3):1411, February 1991.
- [58] P. Bruno, Y. Suzuki, and C. Chappert. Magneto-optical kerr effect in a paramagnetic overlayer on a ferromagnetic substrate: A spin-polarized quantum size effect. *PHYSICAL REVIEW B*, 53(14):9214, April 1996.
- [59] P. M. Oppeneer. Magneto-optical spectroscopy in the valence-band energy regime: relationship to the magnetocrystalline anisotropy. *JOURNAL OF MAGNETISM AND MAGNETIC MATERIALS*, 188(3):275, October 1998.
- [60] J. Kunescaron and P. M. Oppeneer. Exact many-body sum rule for the magneto-optical spectrum of solids. *PHYSICAL REVIEW B*, 61(23):15774, June 2000.
- [61] J. P. Hannon, G. T. Trammell, M. Blume, and Doon Gibbs. X-ray resonance exchange scattering. *PHYSICAL REVIEW LETTERS*, 61(10):1245, September 1988.
- [62] J. Stöhr and H. C. Siegmann. *Magnetism: From fundamentals to nanoscale dynamics*. Springer Berlin, 2006.
- [63] H. Ebert, L. Baumgarten, C. M. Schneider, and J. Kirschner. Polarization dependence of the 2p-core-level photoemission spectra of Fe. *PHYSICAL REVIEW B*, 44(9):4406, 1991.
- [64] F. Meier and B.P. Zakharchenya. *Optical Orientation*, volume 8 of *Modern Problems in Condensed Matter Sciences*. North-Holland, Amsterdam, 1984.

-
- [65] D.-H. Kim, P. Fischer, W. Chao, E. Anderson, M.-Y. Im, S.-C. Shin, and S.-B. Choe. Magnetic soft x-ray microscopy at 15 nm resolution probing nanoscale local magnetic hysteresis (invited). *JOURNAL OF APPLIED PHYSICS*, 99(8):08H303, April 2006.
- [66] T. Miyahara, S.-Y. Park, T. Hanyu, T. Hatano, S. Moto, and Y. Kagoshima. Comparison between 3p and 2p magnetic circular dichroism in transition metals and alloys: Is the sum rule applicable to itinerant magnetic systems? *REVIEW OF SCIENTIFIC INSTRUMENTS*, 66(2):1558, February 1995.
- [67] K. Starke, F. Heigl, A. Vollmer, M. Weiss, G. Reichardt, and G. Kaindl. X-ray magneto-optics in lanthanides. *PHYSICAL REVIEW LETTERS*, 86(15):3415, April 2001.
- [68] J. E. Prieto, F. Heigl, O. Krupin, G. Kaindl, and K. Starke. Magneto-optics of Gd and Tb in the soft x-ray resonance regions. *PHYSICAL REVIEW B*, 68(13):134453, Oct 2003.
- [69] H.-Ch. Mertins, F. Schäfers, X. Le Cann, A. Gaupp, and W. Gudat. Faraday rotation at the 2p edges of Fe, Co, and Ni. *PHYSICAL REVIEW B*, 61(2):R874, January 2000.
- [70] S. Valencia, A. Kleibert, A. Gaupp, J. Ruzs, D. Legut, J. Bansmann, W. Gudat, and P. M. Oppeneer. Quadratic x-ray magneto-optical effect upon reflection in a near-normal-incidence configuration at the M edges of 3d-transition metals. *PHYSICAL REVIEW LETTERS*, 104(18):187401, May 2010.
- [71] B.L. Henke, E.M. Gullikson, and J.C. Davis. X-ray interactions: photoabsorption, scattering, transmission, and reflection at $E=50\text{--}30000\text{ eV}$, $Z=1\text{--}92$. *ATOMIC DATA AND NUCLEAR DATA TABLES*, 54(2):181, July 1993. released by the Center of X-ray Optics.
- [72] H. Kiessig. Interferenz von Röntgenstrahlen an dünnen Schichten. *ANNALEN DER PHYSIK*, 402(7):769, 1931.
- [73] D. T. Attwood. *Soft X-Rays and Extreme Ultraviolet Radiation: Principles and Applications*. Cambridge University Press, 1999.
- [74] P. Jaeglé. *Coherent Sources of XUV Radiation: Soft X-Ray Lasers and High-Order Harmonic Generation*, volume 106 of *Springer Series in Optical Sciences*. Springer, 2005.
- [75] T. Pfeifer, C. Spielmann, and G. Gerber. Femtosecond x-ray science. *REPORTS ON PROGRESS IN PHYSICS*, 69(2):443, January 2006.

- [76] S. Cramm. *Probing the nanoworld: Microscopies, Scattering and Spectroscopies of the Solid State*, chapter Synchrotron radiation sources and beamlines: Overview, page B2. 38th IFF Spring School. Forschungszentrum Jülich, 2007.
- [77] <http://www-xfel.spring8.or.jp/cband/e/undulator.htm>.
- [78] C. Rulliere, editor. *Femtosecond Laser Pulses: Principles and Experiments*. Springer, 2nd edition, October 2004.
- [79] M. Buchmeier, R. Schreiber, D. E. Bürgler, and C. M. Schneider. Thickness dependence of linear and quadratic magneto-optical Kerr effects in ultrathin Fe(001) films. *PHYSICAL REVIEW B*, 79(6):064402, February 2009.
- [80] R. Adam, Y. Khivintsev, R. Hertel, C. M. Schneider, A. Hutchison, R. Camley, and Z. Celinski. Dynamic properties of arrays of ferromagnetic rectangular bars. *JOURNAL OF APPLIED PHYSICS*, 101(9):09F516, May 2007.
- [81] Jeffrey L. Krause, Kenneth J. Schafer, and Kenneth C. Kulander. High-order harmonic generation from atoms and ions in the high intensity regime. *PHYSICAL REVIEW LETTERS*, 68(24):3535, June 1992.
- [82] P. B. Corkum. Plasma perspective on strong field multiphoton ionization. *PHYSICAL REVIEW LETTERS*, 71(13):1994, September 1993.
- [83] C. Winterfeldt. *Generation and Control of High-Harmonic Radiation*. PhD thesis, Julius-Maximilians-Universität Würzburg, 1996.
- [84] L. V. Keldysh. Ionization in the field of a strong electromagnetic wave. *JETP*, 20:1307, 1965.
- [85] A. Rundquist, C. G. Durfee, Z. Chang, C. Herne, S. Backus, M. M. Murnane, and H. C. Kapteyn. Phase-matched generation of coherent soft x-rays. *SCIENCE*, 280(5368):1412, May 1998.
- [86] I. P. Christov, Margaret M. Murnane, and Henry C. Kapteyn. High-harmonic generation of attosecond pulses in the "single-cycle" regime. *PHYSICAL REVIEW LETTERS*, 78(7):1251, February 1997.
- [87] A. Paul. *Coherent EUV Light from High-Order Harmonic Generation: Enhancement and Applications to Lensless Diffractive Imaging*. PhD thesis, University of Colorado, 2007.
- [88] F. Schäfer. *Modern Developments in X-Ray and Neutron Optics*, volume 137 of *Springer Series in Optical Sciences*. Springer, April 2008.

-
- [89] O. Zaharko, P. M. Oppeneer, H. Grimmer, M. Horisberger, H.-Ch. Mertins, D. Abramssohn, F. Schfers, A. Bill, and H.-B. Braun. Exchange coupling in Fe/NiO/Co film studied by soft x-ray resonant magnetic reflectivity. *PHYSICAL REVIEW B*, 66(13):134406, October 2002.
- [90] R. R. Gareev, D. E. Bürgler, M. Buchmeier, D. Olligs, R. Schreiber, and P. Grünberg. Metallic-type oscillatory interlayer exchange coupling across an epitaxial FeSi spacer. *PHYSICAL REVIEW LETTERS*, 87(15):157202, September 2001.
- [91] D. E. Bürgler, C. M. Schmidt, J. A. Wolf, T. M. Schaub, and H. J. Güntherodt. Ag films on Fe/GaAs(001): from clean surfaces to atomic Ga structures. *SURFACE SCIENCE*, 366(2):295, October 1996.
- [92] D. E. Bürgler, P. Grünberg, S. O. Demokritov, and M. T. Johnson. *Interlayer exchange coupling in layered magnetic structures*, volume 13 of *Handbook of Magnetic Materials*. Elsevier Amsterdam, 2001.
- [93] D. E. Bürgler and P. Grünberg. *Magnetoelectronics: Magnetism and Magneto-transport in Layered Structures*. Nanoelectronics and Information Technology. Wiley-Vch, 2005.
- [94] M. Buchmeier, B. K. Kuanr, R. R. Gareev, D. E. Bürgler, and P. Grünberg. Spin waves in magnetic double layers with strong antiferromagnetic interlayer exchange coupling: Theory and experiment. *PHYSICAL REVIEW B*, 67(18):184404, May 2003.
- [95] N. Kreines, D. Kholin, S. Demokritov, and M. Rikart. Noncollinear interlayer exchange in fe/cr/fe magnetic structures with different interface roughnesses. *JETP LETTERS*, 78(10):627, November 2003.
- [96] C.M. Schneider, A. Kaiser, C. Wiemann, C. Tieg, and S. Cramm. Photoemission microscopy study of picosecond magnetodynamics in spin-valve-type thin film elements. *JOURNAL OF ELECTRON SPECTROSCOPY AND RELATED PHENOMENA*, 181:159, 2010.
- [97] A. V. Kimel, A. Kirilyuk, P. A. Usachev, R. V. Pisarev, A. M. Balbashov, and Th. Rasing. Ultrafast non-thermal control of magnetization by instantaneous photomagnetic pulses. *NATURE*, 435(7042):655, June 2005.
- [98] C. D. Stanciu, F. Hansteen, A. V. Kimel, A. Kirilyuk, A. Tsukamoto, A. Itoh, and Th. Rasing. All-optical magnetic recording with circularly polarized light. *PHYSICAL REVIEW LETTERS*, 99(4):047601, July 2007.

- [99] R. N. Simons. *Coplanar Waveguide Circuits, Components, and Systems*. John Wiley & Sons Inc., 2001.
- [100] T. Damm. *Sputterepitaxie von Eisenfilmen und Eisen/Silizium/Eisen - Dreilagenschichtsystemen auf GaAs(001) und MgO(001)*. PhD thesis, Universität zu Köln, January 2004.
- [101] T. Damm, M. Buchmeier, A. Schindler, D. E. Bürgler, P. Grünberg, and C. M. Schneider. Magnetic properties of Fe films and Fe/Si/Fe trilayers grown on GaAs(001) and MgO(001) by ion-beam sputter epitaxy. *JOURNAL OF APPLIED PHYSICS*, 99(9):093905, May 2006.
- [102] <http://bama.ua.edu/~tmewes/Java/CPW/CPWCalculator.shtml>.
- [103] T. Pfeifer, H.-M. Heiliger, T. Löffler, C. Ohlhoff, C. Meyer, G. Lupke, H.G. Roskos, and H. Kurz. Optoelectronic on-chip characterization of ultrafast electric devices: Measurement techniques and applications. *IEEE JOURNAL OF SELECTED TOPICS IN QUANTUM ELECTRONICS*, 2(3):586, 1996.
- [104] T. Fliessbach. *Elektrodynamik: Lehrbuch zur Theoretischen Physik*, volume 2. Spektrum Akademischer Verlag, 5 edition, July 2008.
- [105] L. Rabiner, R. Schafer, and C. Rader. The chirp z-transform algorithm. *IEEE TRANSACTIONS ON AUDIO AND ELECTROACOUSTICS*, 17(2):86, 1969.
- [106] C. Kittel. On the theory of ferromagnetic resonance absorption. *PHYSICAL REVIEW*, 73(2):155, January 1948.
- [107] B. Kuanr, R. E. Camley, and Z. Celinski. Narrowing of the frequency-linewidth in structured magnetic strips: Experiment and theory. *APPLIED PHYSICS LETTERS*, 87(1):012502, July 2005.
- [108] M. Buess, T. Haug, M. R. Scheinfein, and C. H. Back. Micromagnetic dissipation, dispersion, and mode conversion in thin permalloy platelets. *PHYSICAL REVIEW LETTERS*, 94(12):127205, April 2005.
- [109] L. Pan and D. B. Bogy. Data storage: Heat-assisted magnetic recording. *NATURE PHOTONICS*, 3(4):189, April 2009.
- [110] K. Vahaplar, A. M. Kalashnikova, A. V. Kimel, D. Hinzke, U. Nowak, R. Chantrell, A. Tsukamoto, A. Itoh, A. Kirilyuk, and Th. Rasing. Ultrafast path for optical magnetization reversal via a strongly nonequilibrium state. *PHYSICAL REVIEW LETTERS*, 103(11):117201, September 2009.

- [111] B. Koopmans, J. J. M. Ruigrok, F. Dalla Longa, and W. J. M. de Jonge. Unifying ultrafast magnetization dynamics. *PHYSICAL REVIEW LETTERS*, 95(26):267207, December 2005.
- [112] G. P. Zhang, W. Hübner, Georgios Lefkidis, Yihua Bai, and Thomas F. George. Paradigm of the time-resolved magneto-optical Kerr effect for femtosecond magnetism. *NATURE PHYSICS*, 5(7):499, July 2009.
- [113] G. Lefkidis, G. P. Zhang, and W. Hübner. Angular momentum conservation for coherently manipulated spin polarization in photoexcited NiO: An ab initio calculation. *PHYSICAL REVIEW LETTERS*, 103(21):217401, November 2009.
- [114] M. Krauss, T. Roth, S. Alebrand, D. Steil, M. Cinchetti, M. Aeschlimann, and H. C. Schneider. Ultrafast demagnetization of ferromagnetic transition metals: The role of the coulomb interaction. *PHYSICAL REVIEW B*, 80(18):180407, November 2009.
- [115] G. Malinowski, F. Dalla Longa, J. H. H. Rietjens, P. V. Paluskar, R. Huijink, H. J. M. Swagten, and B. Koopmans. Control of speed and efficiency of ultrafast demagnetization by direct transfer of spin angular momentum. *NATURE PHYSICS*, 4(11):855, November 2008.
- [116] M. Battiato, K. Carva, and P. M. Oppeneer. Superdiffusive spin transport as a mechanism of ultrafast demagnetization. *PHYSICAL REVIEW LETTERS*, 105(2):027203, July 2010.
- [117] I. Neudecker, G. Woltersdorf, B. Heinrich, T. Okuno, G. Gubbiotti, and C.H. Back. Comparison of frequency, field, and time domain ferromagnetic resonance methods. *JOURNAL OF MAGNETISM AND MAGNETIC MATERIALS*, 307(1):148, December 2006.
- [118] S. S. Kalarickal, P. Krivosik, M. Wu, E. Patton, M. L. Schneider, P. Kabos, T. J. Silva, and J. P. Nibarger. Ferromagnetic resonance linewidth in metallic thin films: Comparison of measurement methods. *JOURNAL OF APPLIED PHYSICS*, 99(9):093909, May 2006.
- [119] T. D. Rossing. Resonance linewidth and anisotropy variation in thin films. *JOURNAL OF APPLIED PHYSICS*, 34(4):995, April 1963.
- [120] J. M. Shaw, T. J. Silva, M. L. Schneider, and R. D. McMichael. Spin dynamics and mode structure in nanomagnet arrays: Effects of size and thickness on linewidth and damping. *PHYSICAL REVIEW B*, 79(18):184404, May 2009.

- [121] E. A. Gibson. *Quasi-Phase Matching of Soft X-ray Light from High-Order Harmonic Generation using Waveguide Structures*. PhD thesis, University of Colorado, 2004.
- [122] L. Guidoni, E. Beaurepaire, and J. Bigot. Magneto-optics in the ultrafast regime: Thermalization of spin populations in ferromagnetic films. *PHYSICAL REVIEW LETTERS*, 89(1):017401, June 2002.
- [123] H. Ibach and H. Lüth. *Solid-State Physics. An Introduction to Principles of Materials Science*. Springer, Berlin, 3 edition, July 2003.
- [124] D. M. C. Nicholson, W. H. Butler, W. A. Shelton, Yang Wang, X.-G. Zhang, G. M. Stocks, and J. M. MacLaren. Magnetic structure and electronic transport in permalloy. *JOURNAL OF APPLIED PHYSICS*, 81(8):4023, April 1997.
- [125] M. Eisenbach, G. M. Stocks, and D. M. Nicholson. Noncollinear magnetism in permalloy. *JOURNAL OF APPLIED PHYSICS*, 101(9):09G503, May 2007.
- [126] A. P. Malozemoff, A. R. Williams, and V. L. Moruzzi. "Band-gap theory" of strong ferromagnetism: Application to concentrated crystalline and amorphous Fe- and Co-metalloid alloys. *PHYSICAL REVIEW B*, 29(4):1620, February 1984.
- [127] H.-S. Rhie, H. A. Dürr, and W. Eberhardt. Femtosecond electron and spin dynamics in Ni/W(110) films. *PHYSICAL REVIEW LETTERS*, 90(24):247201, June 2003.
- [128] R. Huber, F. Tauser, A. Brodschelm, M. Bichler, G. Abstreiter, and A. Leitenstorfer. How many-particle interactions develop after ultrafast excitation of an electron-hole plasma. *NATURE*, 414(6861):286, November 2001.
- [129] M. Brooks. Thomas-fermi screening of exchange interactions. *JOURNAL OF PHYSICS: CONDENSED MATTER*, 13(22):L469, 2001.
- [130] K. El Sayed, S. Schuster, H. Haug, F. Herzel, and K. Henneberger. Subpicosecond plasmon response: Buildup of screening. *PHYSICAL REVIEW B*, 49(11):7337, March 1994.
- [131] A. Vaterlaus, T. Beutler, and F. Meier. Spin-lattice relaxation time of ferromagnetic gadolinium determined with time-resolved spin-polarized photoemission. *PHYSICAL REVIEW LETTERS*, 67(23):3314, December 1991.
- [132] T. Popmintchev, M.-C. Chen, P. Arpin, M. M. Murnane, and H. C. Kapteyn. The attosecond nonlinear optics of bright coherent x-ray generation. *NATURE PHOTONICS*, 4(12):822, December 2010.

Publications

2011 **Manuscript in preparation,**

"Breakdown of exchange coupling in ultrafast demagnetization of Cu-doped permalloy", S. Mathias, C. La-O-Vorakiat, P. Grychtol, R. Adam, J. Shaw, H. Nembach, M. Siemens, M. Aeschlimann, T. Silva, C. M. Schneider, H. Kapteyn and M. Murnane

2011 **Journal of Electron Spectroscopy and Related Phenomena**, **184**, 287

"Layer-selective studies of an anti-ferromagnetically coupled multilayer by resonant magnetic reflectivity in the extreme ultraviolet range", P. Grychtol, R. Adam, A. M. Kaiser, S. Cramm, D. E. Bürgler and C. M. Schneider

2011 **Journal of Electron Spectroscopy and Related Phenomena**, **184**, 291

"Time-resolved measurements of $Ni_{80}Fe_{20}/MgO/Co$ trilayers in the extreme ultraviolet range", R. Adam, P. Grychtol, S. Cramm and C. M. Schneider

2010 **Physical Review B**, **82**, 054433

"Resonant magnetic reflectivity in the extreme ultraviolet spectral range: Interlayer-coupled $Co/Si/Ni/Fe$ multilayer system", P. Grychtol, R. Adam, S. Valencia, S. Cramm, D. E. Bürgler and C. M. Schneider

2009 **Physical Review Letters**, **103**, 257402

"Ultrafast demagnetization dynamics at the M edges of magnetic elements observed using a tabletop high-harmonic soft x-ray source", C. La-O-Vorakiat, M. Siemens, M. Murnane, H. Kapteyn, S. Mathias, M. Aeschlimann, P. Grychtol, R. Adam, C. M. Schneider, J. Shaw, H. Nembach and T. Silva

2009 **Applied Physics Letters**, **95**, 051901

"Anomalies in the thermomechanical behavior of $Ba_{0.5}Sr_{0.5}Co_{0.8}Fe_{0.2}O_{3-\delta}$ ceramic oxygen conductive membranes at intermediate temperatures", B. X. Huang, J. Malzbender, R. W. Steinbrech, P. Grychtol, C. M. Schneider and L. Singheiser

2007 **Optics Express**, **15**, 10832-10841

"Simultaneous dual-band ultra-high resolution optical coherence tomography",
F. Spöler, S. Kray, P. Grychtol, B. Hermes, J. Bornemann, M. Först and H.
Kurz

Conference Contributions

2011 **DPG spring meeting, Dresden, Germany**

"Ultrafast element-specific decoupling of magnetization dynamics in permalloy", **talk**

2010 **International Symposium on Metallic Multilayers, Berkeley, USA**

"Ultrafast and element-selective demagnetization dynamics probed at the M absorption edges employing a table-top soft x-ray source", **invited talk**

2010 **Ultrafast VUV and X-ray Science Satellite Meeting, Stanford, USA**

"Coupled magnetic multilayer systems studied by resonant reflectivity in the XUV range", **poster**

2010 **International Conference on Vacuum Ultraviolet and X-ray Physics, Vancouver, Canada**

"Coupled magnetic multilayer systems studied by resonant reflectivity in the XUV range", **poster**

2010 **DPG spring meeting, Regensburg, Germany**

"Ultrafast and element-selective demagnetization dynamics probed at the M absorption edges employing a tabletop high-harmonic soft x-ray source", **talk**

2009 **International Colloquium on Magnetic Films and Surfaces, Berlin**

"Quasi-Static and time-resolved T-MOKE measurements of NiFe/MgO/Co layer stacks in the extreme UV range", **poster**

2008 **BESSY user meeting, Berlin**

"Time-resolved magneto-optical measurements of magnetization dynamics in magnetic films and multilayers", **poster**

2008 **DPG spring meeting, Berlin**

"MOKE and BLS measurements of interlayer exchange coupling on epitaxial Fe/Cr/Fe wedge systems", **talk**

Curriculum Vitae

Personal Details

name	Patrik Dominik Grychtol
birth date	11.05.1979
birth place	Kattowitz, Poland
nationality	German

History

10/2007–04/2011	Peter Grünberg Institut, Research Center Jülich Ph.D. thesis
01/2007–09/2007	Traveling Southeast Asia
04/2005–12/2006	Institute of Semiconductor Electronics, RWTH Aachen Diploma thesis: <i>Contrast enhancement in optical coherence tomography</i>
11/2004–03/2005	Traveling Australia and New Zealand
10/2003–10/2004	School of Geoscience, University of Sydney, Australia Postgraduate studies of Environmental Science
10/2002–09/2003	1st Institute of Physics, RWTH Aachen Postgraduate studies of Solid State Physics
04/2002–09/2002	5th Student Parabolic Flight Campaign, ESA, France Participation and technical development of flight experiment: <i>Growth of plasma crystals in zero gravity</i>

- 10/1999–03/2002 **1 st Institute of Physics, RWTH Aachen**
Undergraduate and postgraduate studies of Physics
- 06/1999–09/1999 **Bayer AG, Leverkusen**
Internship in various pharmaceutical departments
- 06/1998–04/1999 **Military service, Lebach**
3./ Fallschirmjägerbataillon 261
- 09/1989–05/1998 **Lise-Meitner-Schule, Leverkusen**
High school diploma

Awards

- 06/2010–09/2010 **JILA, University of Colorado at Boulder, USA**
Research fellowship granted by the German Academic Exchange Service (Deutscher Akademischer Austausch Dienst – DAAD)

References

Prof. Claus M. Schneider 1 st Ph.D. advisor

Contact: Forschungszentrum Jülich
Peter Grünberg Institut
Leo-Brandt-Strasse
D–52425 Jülich, Germany
c.m.schneider@fz-juelich.de +49-2461-61-4428

Prof. Martin Aeschlimann 2 nd Ph.D. advisor

Contact: Technische Universität Kaiserslautern
Fachbereich Physik
Erwin Schrödinger Strasse 46
D–67663 Kaiserslautern, Germany
ma@physik.uni-kl.de +49-631-205-2322

Prof. Margaret Murnane Cooperation partner

Contact: JILA and Departments of Physics and ECE
University of Colorado at Boulder
Boulder, CO 80309-0440, USA
murnane@jila.colorado.edu +1-303-210-0396

May 28, 2011

1. **Soft Matter**
From Synthetic to Biological Materials
Lecture manuscripts of the 39th IFF Spring School March 3 – 14, 2008
Jülich, Germany
edited by J.K.G. Dhont, G. Gompper, G. Nägele, D. Richter, R.G. Winkler (2008),
c. 1000 pages
ISBN: 978-3-89336-517-3
2. **Structural analysis of diblock copolymer nanotemplates using grazing incidence scattering**
by D. Korolkov (2008), III, 167 pages
ISBN: 978-3-89336-522-7
3. **Thermal Nonequilibrium**
Thermal forces in fluid mixtures
Lecture Notes of the 8th International Meeting on Thermodiffusion,
9 – 13 June 2008, Bonn, Germany
edited by S. Wiegand, W. Köhler (2008), 300 pages
ISBN: 978-3-89336-523-4
4. **Synthesis of CMR manganites and ordering phenomena in complex transition metal oxides**
by H. Li (2008), IV, 176 pages
ISBN: 978-3-89336-527-2
5. **Neutron Scattering**
Lectures of the JCMS Laboratory Course held at the Forschungszentrum Jülich
and the research reactor FRM II of TU Munich
edited by R. Zorn, Th. Brückel, D. Richter (2008), ca. 500 pages
ISBN: 978-3-89336-532-6
6. **Ultrafast Magnetization Dynamics**
by S. Woodford (2008), 130 pages
ISBN: 978-3-89336-536-4
7. **Role of Surface Roughness in Tribology: from Atomic to Macroscopic Scale**
by C. Yang (2008), VII, 166 pages
ISBN: 978-3-89336-537-1
8. **Strahl- und Spindynamik von Hadronenstrahlen in Mittelenergie-Ringbeschleunigern**
von A. Lehrach (2008), II, 171 Seiten
ISBN: 978-3-89336-548-7
9. **Phase Behaviour of Proteins and Colloid-Polymer Mixtures**
by C. Gögelein (2008), II, 147 pages
ISBN: 978-3-89336-555-5

10. **Spintronics – From GMR to Quantum Information**
Lecture Notes of the 40th IFF Spring School March 9 – 20, 2009
Jülich, Germany
edited by St. Blügel, D. Bürgler, M. Morgenstern, C. M. Schneider,
R. Waser (2009), c. 1000 pages
ISBN: 978-3-89336-559-3
11. **ANKE / PAX Workshop on SPIN Physics**
JINR, Dubna, Russia / June 22. – 26, 2009
Org. Committee: A. Kacharava, V. Komarov, A. Kulikov, P. Lenisa, R. Rathmann,
H. Ströher (2009), CD-ROM
ISBN: 978-3-89336-586-9
12. **Entwicklung einer Nanotechnologie-Plattform für die Herstellung
Crossbar-basierter Speicherarchitekturen**
von M. Meier (2009), 135 Seiten
ISBN: 978-3-89336-598-2
13. **Electronic Oxides –
Correlation Phenomena, Exotic Phases and Novel Functionalities**
Lecture Notes of the 41st IFF Spring School March 8 – 19, 2010
Jülich, Germany
edited by St. Blügel, T. Brückel, R. Waser, C.M. Schneider (2010), ca. 1000
pages
ISBN: 978-3-89336-609-5
14. **4th Georgian-German School and Workshop in Basic Science**
Tbilisi, Georgia / May 3 – 7, 2010
Org. Committee: E. Abrosimova, R. Botchorishvili, A. Kacharava, M. Nioradze,
A. Prangishvili, H. Ströher (2010); CD-ROM
ISBN: 978-3-89336-629-3
15. **Neutron Scattering**
Lectures of the JCNS Laboratory Course held at Forschungszentrum Jülich and
the research reactor FRM II of TU Munich
edited by Th. Brückel, G. Heger, D. Richter, G. Roth and R. Zorn (2010),
ca 350 pages
ISBN: 978-3-89336-635-4
16. **Ab initio investigations of magnetic properties of ultrathin transition-metal
films on 4d substrates**
by A. Al-Zubi (2010), II, 143 pages
ISBN: 978-3-89336-641-5
17. **Investigation of a metal-organic interface realization and understanding of
a molecular switch**
by O. Neucheva (2010), 134 pages
ISBN: 978-3-89336-650-7

18. **Reine Spinströme in lateralen Spinventilen, *in situ* Erzeugung und Nachweis**
von J. Mennig (2010), V, 95 Seiten
ISBN: 978-3-89336-684-2

19. **Nanoimprint Lithographie als Methode zur chemischen Oberflächenstrukturierung für Anwendungen in der Bioelektronik**
von S. Gilles (2010), II, 169 Seiten
ISBN: 978-3-89336-686-6

20. **Macromolecular Systems in Soft- and Living-Matter**
Lecture Notes of the 42nd IFF Spring School 2011 February 14 – 25, 2011
Jülich, Germany
edited by Jan K.G. Dhont, Gerhard Gompper, Peter R.Lang, Dieter Richter,
Marisol Ripoll, Dieter Willbold, Reiner Zorn (2011), ca. 1000 pages
ISBN: 978-3-89336-688-0

21. **The spin structure of magnetic nanoparticles and in magnetic nanostructures**
by S. Disch (2011), V, 342 pages
ISBN: 978-3-89336-704-7

22. **Element-selective and time-resolved magnetic investigations in the extreme ultraviolet range**
by P. Grychtol (2011), xii, 144 pages
ISBN: 978-3-89336-706-1

